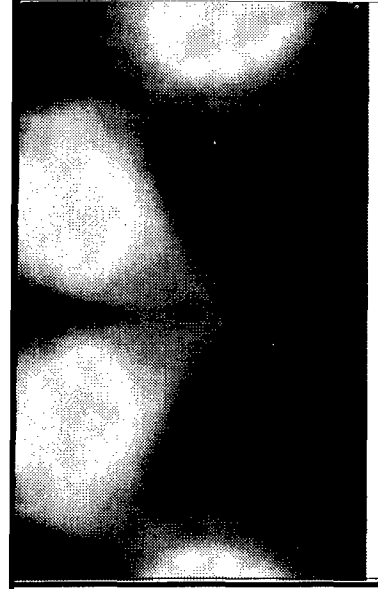

Armed Forces
Radiobiology Research Institute

AFRRI Reports

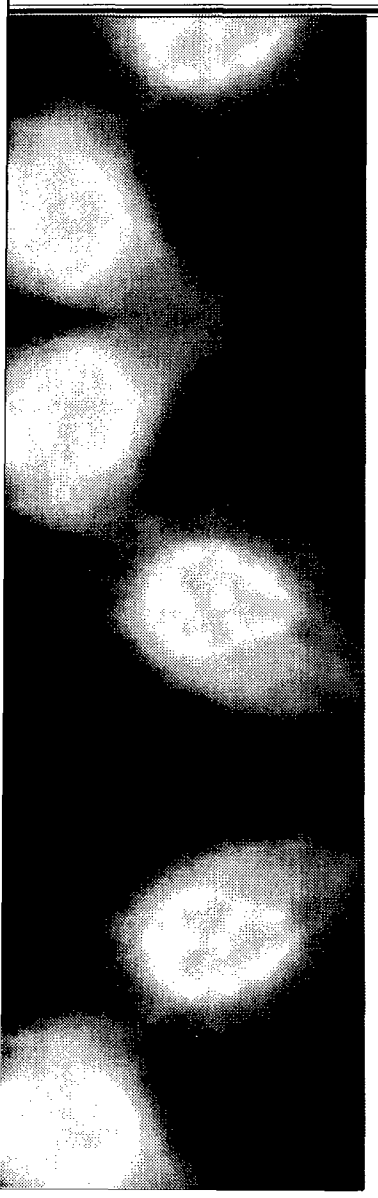

Third - Fourth Quarters
1997

Armed Forces
Radiobiology Research Institute
8901 Wisconsin Avenue
Bethesda, MD 20889-5603
www.afrri.usuhs.mil

AFRRI Reports

Third - Fourth Quarters
1997

CONTENTS

IN VITRO TOXICOLOGY
Volume 10, Number 2, 1997
Mary Ann Liebert, Inc.

Could Nitrosyl Chloride Be Produced by Human Skin Keratinocytes and Sulfur Mustard? A Magnetic Resonance Study

CARMEN M. ARROYO, ALASDAIR J. CARMICHAEL,[1] and CLARENCE A. BROOMFIELD

ABSTRACT

It is known that alkylating processes occur after exposure to sulfur mustard (HD). Although direct alkylation of DNA and RNA has been widely described, we hypothesize additional alkylation events of potential importance in skin injury. We have determined by immunocytochemistry levels of interleukin-1 β (IL-1β) in cultures of normal human epidermal keratinocytes (NHEK) after exposure to HD. The expression of IL-1β in NHEK was found to be related to cell culture donor age. In neonatal NHEK exposed to HD (2 mM), IL-1β expression is decreased. Conversely, in adult breast NHEK exposed to HD (2 mM), IL-1β response is increased. Electron paramagnetic resonance (EPR) spectroscopy was used to show the formation of an EPR detectable, g = 2.04, feature characteristic of iron-nitrosyl complex formation, and the generation of this induced complex by NHEK exposed to HD (1 mM for 18 hours) was blocked by N^w-Nitro-L-arginine (L-NOARG), a competitive inhibitor of nitric oxide synthase (NOS). Nitric oxide ($^{\bullet}NO$) has been implicated as the effector molecule that mediates IL-1β (Corbett et al., 1993). Our results show the release of nitric oxide during cytokine expression, IL-1β, when keratinocytes are exposed to HD. The combination of the nitric oxide with the chloride (Cl^-) released from sulfur mustard ($[ClCH_2CH_2]_2S$) on cyclization to the sulfonium ion may lead to the formation of nitrosyl chloride (NOCl), a known potent alkylating agent. If NOCl is formed as a result of HD exposure, then it may play a role in the skin injury.

INTRODUCTION

The experiments described in this work deal with the effects of sulfur mustard (HD) on normal human epidermal keratinocytes (NHEK). Keratinocytes are the cells found in the outer layer of the skin and are the primary targets of mustard exposure.

Analysis of normal human epidermis using specific enzyme-linked immunosorbent assays (ELISA) and bioassays for the cytokine interleukin (IL-1) have led to the conclusion that the average adult harbors 20 to 60 μg (0.6 to 1.9 nmol) of IL-1 in his or her epidermis (Kupper et al., 1989). Taking the epidermis as a three-dimensional space with a thickness of 0.1 mm and an area of 1.5 m^2, the concentration of IL-1 in this space is 4 to 12 nmol/L. This concen-

U.S. Army Medical Research Institute of Chemical Defense, Aberdeen Proving Ground, Maryland, and [1]Applied Cellular Radiobiology Department, Armed Forces Radiobiology Research Institute, Bethesda, Maryland.

tration exceeds the concentration of IL-1 required to activate certain cells by three orders of magnitude (<10 pmol). Keratinocytes can express higher numbers of IL-1 receptors than can any other cell type studied (Kupper et al., 1989; Blanton et al., 1989). A variety of stimuli can enhance IL-1 receptor expression *in vitro*. These include phorbol esters, calcium, and UV-radiation (Dinarello, 1991). Most keratinocyte interleukin (*in vivo* and *in vitro*) is cell associated; relatively little is released from the cell. In this report, we have determined by immunocytochemistry levels of interleukin-1β (IL-1β) in cultured NHEK after exposure to HD. HD is a known DNA alkylating agent causing mutations that lead to cell injury or death. However, the exact mechanism of alkylation remains unclear. What is known is that the action of alkylating agents, such as HD, proceeds through a mechanism that involves as a first step, formation of a cyclic aklylating agent (sulfonium ion) and the release of chloride (equation 1):

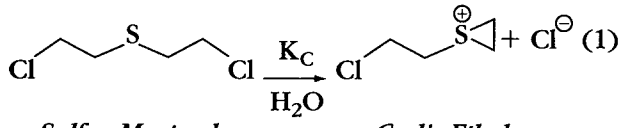

Sulfur Mustard *Cyclic Ethylene Sulfonium Ion*

The hydrolysis of HD in an aqueous media at 37°C is rapid, with $t_{1/2}\sim$ 2 minutes (Lawley, 1976; Lieske et al., 1992).

Furthermore, HD may affect or alter various cell pathways prior to reaching the DNA located in the nucleus. Therefore, the action of alkylation agents on target organ cells may proceed via three principal mechanisms: 1) the physical interaction of the alkylating agent with cellular receptors; 2) the chemical reaction of the alkylating agent with these receptors; or 3) either type of metabolite-receptor interaction following metabolism of the alkylating agent within the target organ or elsewhere.

In addition, electron paramagnetic resonance (EPR) and enzyme-linked immunosorbent assay (ELISA) results (Figure 1 and Figure 2) show the generation of nitric oxide ($^{\bullet}$NO), therefore, suggesting that nitric oxide synthase (NOS) plays a role during IL-1 expression when keratinocytes are exposed to HD. Inducible nitric oxide synthase (iNOS) has been associated with inflammatory and autoimmune tissue injury (Kolb et al., 1992). Their findings show the presence of iNOS in human skin that can be localized to keratinocytes in the epidermal layer. This article shows the possible involvement of active nitrogen species in the pathways of cell injury/repair after exposure to HDs. Active nitrogen species are those derived from nitric oxide generated in cells. The possible involvement of the known alkylating agent nitrosyl chloride (NOCl) is discussed. The thermodynamic considerations and possible *in vivo* production of NOCl by macrophages and neutrophils have been reported (Koppenol, 1994).

MATERIALS AND METHODS

NHEK (adult and neonatal, Clonetics, San Diego, CA) were cultured to confluency and harvested for experiments. The culture medium used was keratinocyte basal medium, modified Molecular Cellular Developmental Biology 153 (MCDB 153), which was supplemented with bovine pituitary extract (7.5 mg/mL); human recombinant epidermal growth factor (0.1 μg/mL); hydrocortisone (0.5 mg/mL); bovine insulin (5 mg/mL); gentamicin sulfate (50 mg/mL); and amphotericin-B (50 μg/mL). The medium was changed after 2 days of culture. At days 3 and 6, the cells were harvested. After harvesting, the NHEK were resuspended in phosphate medium ($5 \times 10^6 - 5 \times 10^7$ cells/0.5 mL). IL-1β and EPR were measured after exposure of the suspension 1–2 mM HD, 0.1 mM N^w-nitro-L-arginine (L-NOARD); $C_6H_{13}N_5O_4$, Sigma Chemical Co., St. Louis, MO), or a combination of these agents. IL-1β expression was measured after 3-hour exposure and heme-NO EPR was measured after 18-hour exposure. The IL-1β expression was measured using two commercially available kits for the ELISA technique (Quantikine™ and Predicta®). These kits are specific for IL-1β and show no cross reactivity with other cytokines (eg, IL-1α, etc.) as stated in the Quantikine™ and Predicta® brochures for IL-1β.

The Quantikine™ human IL-1β Immunoassay (Catalog Number DLB50, R&D Systems, Inc., Minneapolis, MN) was used for the quantitative determination of human IL-1β concentration in the cell cultures. This assay uses the quantita-

tive "sandwich" enzyme immunoassay technique. A monoclonal antibody specific for IL-1β is coated onto the microtiter plate provided in the kit. Standards and homogenous cell suspensions (100 μL) were pipetted into the wells, and IL-1β was added to the wells to sandwich the IL-1β immobilized during the first incubation. After a wash to remove any unbound antibody-enzyme reagent, a substrate solution was added to the wells and color developed in proportion to the amount of IL-1β bound in the initial step. The color development was stopped and the intensity of the color was measured. By comparing the optical density of the samples to the standard curve, the concentration of the IL-1β in the unknown samples was then determined. Representative data are shown in Figure 2.

The Predicta® Interleukin-1β Kit (Genzyme Diagnostics, Cambridge, MA) contained a 96-well microtiter plate with immobilized mouse monoclonal antibody to IL-1β. Aliquots (100 μL) of sample (homogenous cell suspension) or standard were added to each test well and incubated, allowing any IL-1β present to bind to antibodies on the microtiter plate. The wells were washed and a rabbit polyclonal antibody to IL-1β was added. This antibody was found to the captured IL-1. After a subsequent incubation, the wells were washed and a peroxidase-labeled goat anti-rabbit IgG reagent was added. This reagent attached to the polyclonal antibody in the immune complex on the plate. After a third wash, a substrate (peroxide) and chromagen (tetramethylbenzidine) were added to the wells, producing a blue color in the presence of the peroxidase enzyme. The color reaction was stopped by the addition of sulfuric

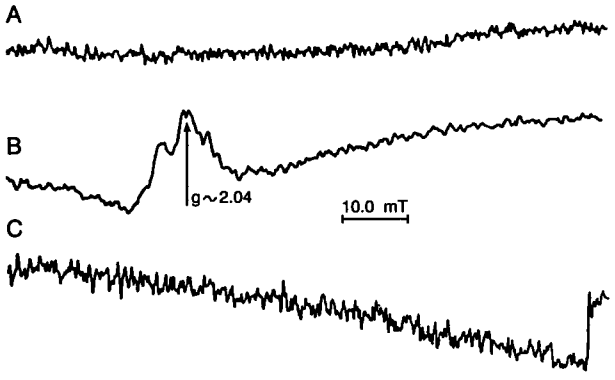

FIG. 1. Low temperature (liquid nitrogen, 77°K) EPR spectra recorded from NHEK suspensions (3.8 × 10^6 cells/mL). A: Control, nonexposed adult NHEK. B: Adult NHEK exposed to 1 mM HD collected 18 hours post-HD exposure. C: Sample treated with N^w-Nitro-L-arginine (L-NOARG) to final concentration of 100 μM. EPR conditions were magnetic field, 334.5 mT; modulation frequency, 100 kHz; microwave frequency, 9.475 GHz; microwave power, 10 mW; receiver gain, 5 × 10^5; modulation amplitude, 0.5 mT and scan rate 0.62 mT/s.

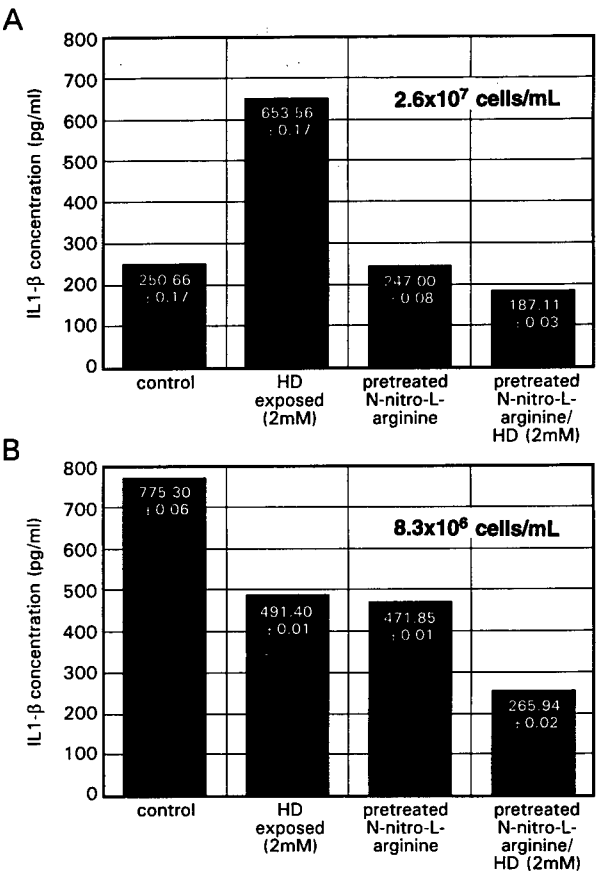

FIG. 2. IL-1β activation of adult and neonatal NHEK exposed to 1–2 mM HD. The IL-1β levels in cell suspensions ($5 \times 10^6 - 5 \times 10^7$ cells/mL) were measured using IL-1β Predicta® Human Cytokine and Quantikine™ ELISA kits. (A) 100-μL aliquots of adult NHEK (2.6×10^7 cells/mL) as a function of IL-1β (pg/mL) produced in HD-exposed and nonexposed controls. (B) 100-μL aliquots of neonatal NHEK (8.3×10^6 cells/mL) as function of IL-1β (pg/mL) produced in HD-exposed and nonexposed controls. The effect of N^w-nitro-L-arginine (L-NOARG) alone and the combined effects of HD and L-NOARG on IL-1β expression by NHEK are also included in panel A and panel B.

acid, which changes the blue to yellow. The intensity of the yellow color was directly proportional to the amount of IL-1β present in the sample or standard. The absorbance of each well was read at 450 nm and a standard curve was constructed to quantitate IL-1β concentrations in the cell samples. Results of several representative experiments are shown in Figure 2.

EPR spectroscopy experiments were performed using cell suspensions containing at least 5×10^6 keratinocyte cells/mL suspended in 1 mL of complete MCDB 153 media. The cells were incubated at 37°C for an additional 18 hours in the presence or absence of 1 mM HD or 50 to 100 μM of L-NOARG at which time the cells were isolated and frozen at −70°C. EPR spectroscopy was performed at 77°K on the cell suspensions using a Varian E-109 spectrometer equipped with a X-band (9 GHz) microwave bridge. The instrumental parameters at which the EPR spectra were recorded are given in Figure 1.

The NHEK cells (HD-treated and untreated) were centrifuged, and the supernates were separated and stored at −70°C for the NO_2^- measurements while the pellets were resuspended in saline buffer for other experiments. Cell suspensions were centrifuged at 1500 rpm for 10 minutes on a Beckman TJ-6 centrifuge. Two methods were used to determine the concentration of nitrite (NO_2^-) as a decomposition product of $^\bullet$NO generated in NHEK suspensions in the presence and absence (controls) of HD. The first method made use of a Sievers 270 B $^\bullet$NO Chemiluminescence Analyzer. This method applies to either $^\bullet$NO or NO_2^- and is based on the hypothesis that in biological systems $^\bullet$NO decomposes into NO_2^-. The NO_2^- formed in the sample is reconverted into $^\bullet$NO in a reaction chamber containing deaerated glacial acetic acid and potassium iodide. The regenerated $^\bullet$NO is carried over by an inert gas (argon or helium) into another reaction chamber containing ozone. The reaction between ozone and $^\bullet$NO luminesces, and the luminescence proportional to the concentration of $^\bullet$NO/NO_2^- present in the sample is measured. The concentration of NO_2^- in the sample solutions is determined from a calibration curve relating NO_2^- concentration to chemiluminescence. The calibration curve was constructed by running a series of standard nitrite ($NaNO_2$, Sigma Chemical Co., St. Louis, MO; cat. no. S2252) solutions on the Sievers 270 B and relating their concentration to chemiluminescence. Alternatively, cells were removed from dry ice and allowed to thaw at 25°C. Stock solution identified as *A* (1% sulfanilamide (Sigma Chemical Co, cat. no. S9251) was dissolved in 50% phosphoric acid (w/v). Solution *A* was kept cold and wrapped in aluminum foil. Solution identified as solution *B* (0.1%N-(1-naphthyl)ethylenediamine (Sigma Chemical Co; cat. no. N9125)) was dissolved in distilled water (w/v), kept cold and wrapped in aluminum foil. Sodium nitrite standard was dissolved in distilled water and kept cold. Equal amounts of standard (200 μL) or sample containing solution *A* were mixed together for 1 to 10 minutes. An equal amount of solution *B* (200 μL) was added. The mixture turned from pink to purple. The microwell plate was then read in a microplate reader set at 540 nm or 550 nm. Control and standard curves were compared. In either type of analysis all samples showed a weak response. In addition, there was no significant difference between the controls (0.47 pmol/μL) and the HD-exposed (0.50 pmol/μL) samples.

RESULTS

Adult NHEK exposed to HD and incubated for 18 hours at 37°C induced the formation of EPR-detectable signals (Fig. 1). The EPR spectra in Figure 1 were obtained by freezing the samples to 77°K in liquid nitrogen after the incubation at 37°C for 18 hours. Figure 1A is the control and represents the EPR spectrum obtained when adult NHEK were incubated in the absence of HD and then frozen. However, adult NHEK exposed to HD and incubated generate the EPR spectrum shown in Figure 1B. This EPR spectrum has an approximate g-value of g = 2.04, which is similar to the g-values of known reported iron-nitrosyl complexes suggesting the formation of nitric oxide ($^\bullet$NO) (Corbett et al., 1991). The observed EPR spectrum may originate directly from the formation of $^\bullet$NO or one of the reactive nitrogen byproducts (NO_x) generated in the biological decomposition of $^\bullet$NO. Because this spectrum suggests that adult NHEK

generate •NO during HD exposure, the cells were incubated with HD in the presence of the specific NOS inhibitor L-NOARG (Fukuto and Chaudhuri, 1995) in order to confirm the production of •NO. The result from this experiment is shown in Figure 1C. The result indicates that the EPR spectrum shown in Figure 1B is not generated when the cells are incubated with HD in the presence of L-NOARG. This strongly suggests that •NO is produced when adult NHEK are exposed to HD. Neonatal NHEK incubated in the presence and absence of HD do not generate the EPR spectrum shown in Figure 1B. It is possible that if •NO is produced by neonatal NHEK either in the unexpected controls or in the HD-exposed cells, this •NO may originate from another source and have a different function, thus rendering it unavailable to interact with iron to form an iron-nitrosyl type complex as seen in Figure 1B. It is also conceivable that low concentrations of •NO are always present in neonatal NHEK. This concentration may be too low to detect by EPR but high enough to cause other types of biological effects (eg, cytokine expression).

It is of importance to establish what role the production of •NO plays during exposure of NHEK to HD. Previous reports have shown that •NO is involved in immune/cytokine regulation (Nathan and Xie, 1994). Furthermore, exposure to HD causes blister formation as an immune response to the action of HD. Therefore, to establish the role of •NO plays during HD exposure, the effect that HD exposure has on cytokine regulation must be determined.

Initially the effect of HD on the production of IL-1β was chosen because human skin keratinocytes express significant numbers of IL-1 receptors determined by the ELISA technique. For this reason, the ELISA technique was performed on adult NHEK and neonatal NHEK ($5 \times 10^6 - 5 \times 10^7$ cells) exposed to HD (2 mM) and incubated for 180 minutes at 37°C. This exposure time is sufficient to allow expression of a significant quantity of IL-1β. However, it is not long enough to allow the cells (adult and neonatal) to go through a complete cycle and divide, thus eliminating possible errors due to differences in cell turnover time (~21 hours for neonatal NHEK and ~24 hours for adult NHEK). The HD concentration range was chosen because it is generally observed that exposure to approximately 1 mM HD causes formation of microblisters while full blister formation occurs after exposure to approximately 2 mM HD. The results are shown in Figure 2. Adult NHEK exposed to HD (2 mM) show a significant increase in the production of IL-1β (Fig. 2A). When these cell suspensions are incubated with the specific NOS inhibitor L-NOARG prior to the HD exposure, the production of IL-1β is decreased to the level obtained for the cells (controls) not exposed to HD. In addition, the combined effects of incubation with L-NOARG followed by exposure to HD slightly lowers the production of IL-1β when compared to the cell suspensions incubated with L-NOARG alone or to controls. For neonatal NHEK exposed to HD (2 mM) the production of IL-1β is decreased when compared with the cells (controls) not exposed to HD (Fig. 2B). Furthermore, incubation of the cell suspensions with L-NOARG alone also decreases the production of IL-1β. In this case the level of IL-1β produced is the same as the level for HD exposed cells (Fig. 2B). The combined effects of incubation with L-NOARG followed by HD exposure are also shown in Fig. 2B. These show a further decrease in the production of IL-1β when compared with the controls and with the cells exposed to HD alone or cells incubated with L-NOARG alone. The concentration of IL-1β per cell before and after exposure to HD or treatment with L-NOARG is given in Table 1. The data shows that the neonatal NHEK contain a significantly larger amount of IL-1β per cell when compared with the adult NHEK.

The approximately tenfold difference in IL-1β concentration per cell in the untreated control adult and neonatal NHEK can be attributed to two reasons: 1) a continual higher level of IL-1β in neonatal NHEK is required for the induction of growth factors for proliferation and other structural proteins required for the normal keratinocyte development; and 2) the fully developed •NO-related immune pathways in adult NHEK differs from the developing •NO-related immune pathways in the neonatal NHEK. For instance, the data (Fig. 2) show that the production of IL-1β is directly linked to the production of •NO. Therefore, it is possible that the adult NHEK contain a low concentration of the constitutive form of NOS (cNOS), but have the

TABLE 1. CONCENTRATION OF INTERLEUKIN-1β PER CELL

Cell type	*n*[a]	*Control (pg/cell) × 10⁶*	*HD (pg/cell) × 10⁶*	*L-NOARG (pg/cell) × 10⁶*	*L-NOARG + HD (pg/cell) × 10⁶*
Adult	3	9.64	25.14	9.50	7.20
Neonatal	3	93.41	59.20	56.85	32.04

[a]n = number of experiments. All columns are the average over number of experiments.

capability of rapidly producing iNOS, which is activated immediately on the presence of a foreign toxic substance. Alternatively, the neonatal NHEK contain mainly the cNOS and thus require only small concentrations of iNOS. This would mean that adult NHEK produce iNOS on demand in the presence of a foreign toxic substance (HD in this case) generating the •NO that triggers the observed increase in IL-1β production. However, neonatal NHEK contain a steady concentration of cNOS that is continuously producing low levels •NO that in turn triggers the observed higher level production of IL-1β. Although the adult and neonatal NHEK appear to contain different forms of NOS enzyme, both types of cells are affected in the same manner by the specific NOS inhibitor L-NOARG even though both types of cells (adult and neonatal) react in an opposite manner when exposed to HD.

The lower yield of IL-1β (Fig. 2B) when neonatal NHEK are exposed to HD as compared with unexposed controls is possibly due to the interaction of HD with the cell surface. It is possible that activation of cNOS and iNOS originates from different receptors on the cell surface. Therefore, because neonatal NHEK appear to contain only cNOS, it is likely that the interaction of HD with the cell surface would interfere with the continuous production of •NO and IL-1β (Fig. 2B). This is consistent with the fact that no EPR signal is observed for HD-exposed neonatal NHEK when suspensions of these cells were run in the same manner as the adult NHEK (Fig. 1). However, the reason for not observing an EPR signal in the unexposed controls remains unclear at this time. These observations are consistent with previous studies (Hunyadi et al., 1992), which suggest that the surface characteristics of NHEK are continuously changing. These modulations reflect the stage of differentiation and activation of the NHEK. Thus, the NHEK in various stages of differentiation have distinct sets of surface moieties that are expressed in different manners (Fig. 2).

There is one thing that is clear from the results in Figure 2 and that is the dependence of the production of IL-1β in adult and neonatal NHEK on the generation of •NO. This establishes •NO as an effector molecule in cytokine regulation especially in the case of IL-1β. This fact is supported by the observation that when the production of •NO is blocked by the specific NOS inhibitor (L-NOARG) the production of IL-1β is also terminated. The results suggest that the production of •NO by the NHEK serves as a direct IL-1 converting enzyme activator or that •NO formed triggers a signal at the cell membrane that activates the IL-1 converting enzyme.

The fate of the •NO generated by the NHEK after activating the IL-1β system remains to be addressed. The •NO generated by cells usually decomposes into NO_2^-. However, there was no difference in the concentration of NO_2^- measured in the controls (0.47 pmol/μL) and HD-exposed (0.50 pmol/μL) NHEK. These results suggest that 1) NO_2^- is not formed during cell exposure to HD, and 2) the •NO generated forms another reactive nitrogen species. Because chloride (Cl^-) is released on dissolution of HD in aqueous environments, it is possible that the reactive nitrogen species formed is NOCl. NOCl is a DNA alkylating agent that is consistent with the known biological action of HD. Alternatively, although NO_2^- or nitrous acid (HNO_2) is known to cause transitional mutations on DNA, there are no available reports that NO_2^-/HNO_2 act on DNA as alkylating agents.

In addition, NOCl and •NO react with he-

moglobin yielding the EPR spectra shown in Figure 3. Figure 3A represents the reaction of NOCl with hemoglobin and Figure 3B represents the reaction of a solution of dissolved •NO with hemoglobin (1×10^{-4} M). Both these EPR spectra have similar g-values to the one observed in Figure 1B. However, in Figure 3A the NOCl was generated chemically in a reaction vessel and then carried over with an inert gas (nitrogen) and bubbled through hemoglobin (1×10^{-4} M) solution. The hemoglobin solution containing the NOCl was rapidly frozen at 77°K in liquid nitrogen prior to obtained its EPR spectrum. Therefore, it is possible that EPR spectrum in Figure 1B does not originate from the direct interaction of •NO with some type of porphyrin-containing molecule, but via the interaction with NOCL with the porphyrin-containing molecule. This being the case, the EPR spectrum (Fig. 1C) would not be observed in the presence of the NOS inhibitor L-NOARG because •NO is required to react with the Cl^- originating from the HD.

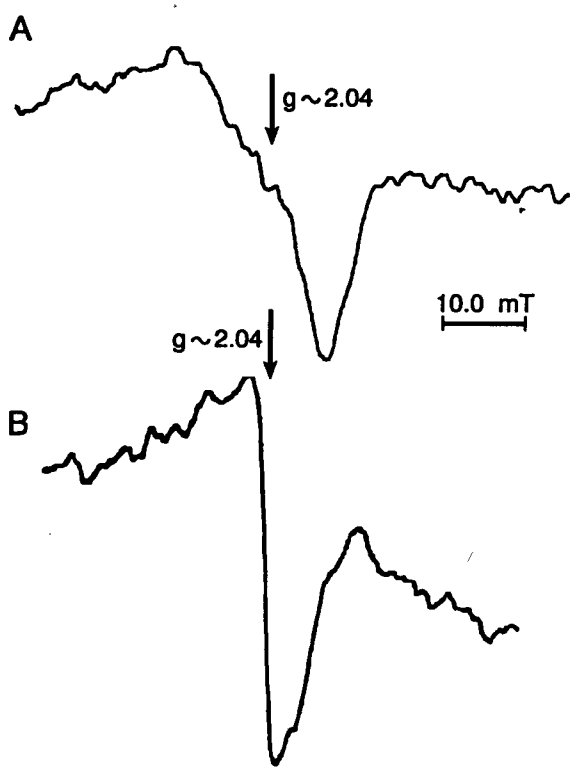

FIG. 3. Low temperature (77°K) EPR spectrum of hemoglobin after reaction with (A) chemically generated NOCl, and (B) dissolved •NO. EPR conditions were magnetic field, 334.5 mT; modulation frequency, 100 kHz; microwave frequency, 9.475 GHz; microwave power, 10 mW; receiver gain, 1.25×10^4; modulation amplitude, 1.0 mT and scan rate 0.833 mT/s.

DISCUSSION

The presence of Cl^- from the dissociation of HD and •NO production or one of its active nitrogen byproducts (NO_x) during the expression of IL-1β may feasibly generate the highly reactive alkylating agent NOCl:

$$Cl^- + NO_x \rightarrow NOCl \quad (2)$$

Nitrosyl Chloride

The Gibbs energy of formation of NOCl is energetically feasible (Williams, 1988). Nitrosyl chloride can nitrosylate organic compounds directly, and therefore its presence poses two dangers: 1) it is a strong oxidant, and 2) nitrosylation leads to compounds that are often mutagenic or promutagenic (alkylation of DNA). If the substrate concentration is sufficient to ensure that its rate of reaction is much greater than the hydrolysis of NOCl then NOCl formation is rate-limiting. In quantitative terms, this occurs when $K_2[RNH_2] > > K_1[H_2O]$ (reactions 3–5).

$$HNO_2 + H_3O^+ \rightleftharpoons H_2NO_2^+ + H_2O \quad (3)$$

$$H_2NO_2^+ + Cl^- \underset{K_{-1}}{\overset{K_1}{\rightleftharpoons}} NOCl + H_2O \quad (4)$$

$$NOCl + RNH_2 \xrightarrow{K_2} RN_2^+ \rightarrow RCl \quad (5)$$

A hypothetical model consistent with the results is shown in Figure 4. Both adult and neonatal NHEK conform to this scheme under normal circumstances. However, because of the suggested difference in the NOS-type (inducible or constitutive) in these cells, their reaction to HD exposure is quite different. In terms of IL-1β production, "resting" keratinocytes in normal skin do not express significant numbers of IL-1 receptors. The resting keratinocyte can be in an "activated" or "refractory" state. The IL-1β receptor expression is associated with the active state of the keratinocyte and requires an outside

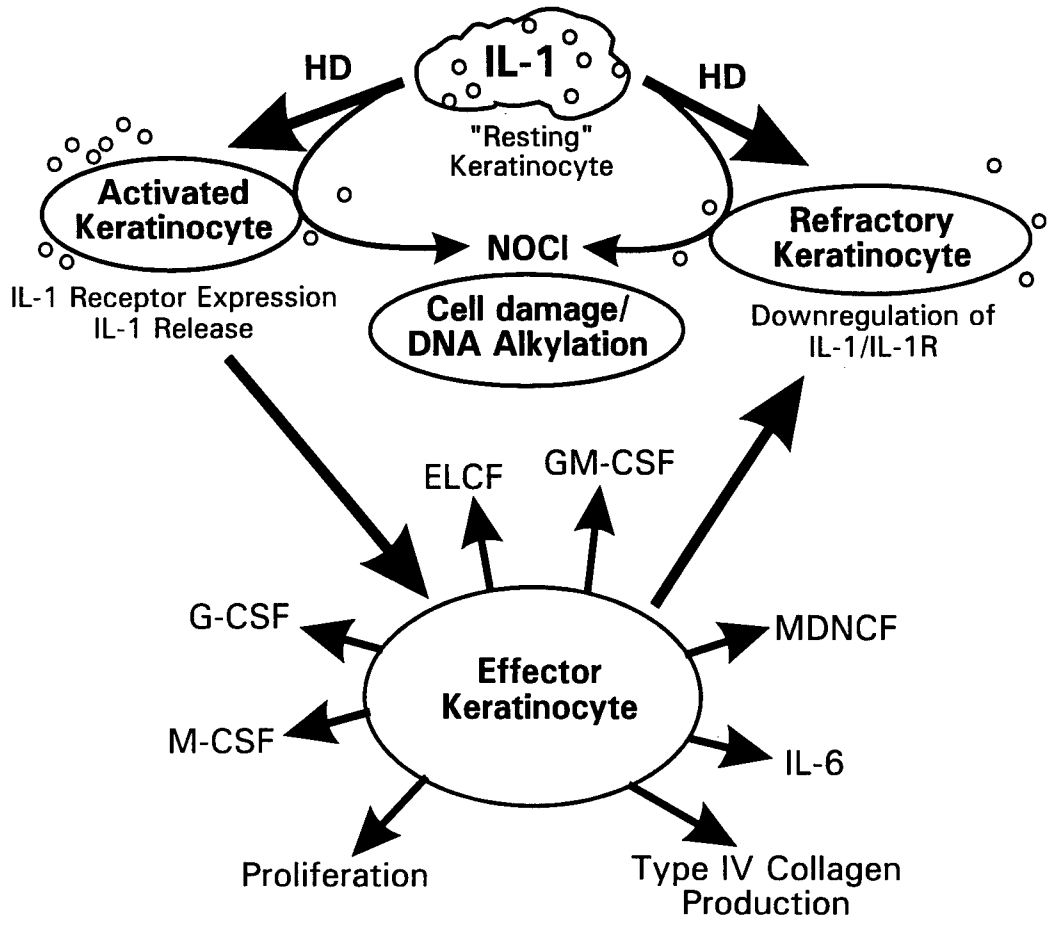

FIG. 4. Hypothetical model of keratinocyte activation. The cellular activation of keratinocytes that follows the binding of IL-1 to its cell-surface causes gene expression of various products including interleukin-6 (IL-6), granulocyte (G), macrophage (M) and GM colony-stimulating factors (CSFs), epidermal-derived lymphocyte chemotactic factor (ELCF) and mononuclear cell-derived neutrophil chemotactic factor (MDNCF). Other consequences of IL-1 binding to its receptor include proliferation, chemotaxis, and type IV collagen production. Adapted from Kupper (1990).

stimulus to express the receptor and generate IL-1β. Exposure to HD causes adult NHEK to go into the activated state generating $^{\bullet}$NO, which in turn activates the IL-1β receptors causing the production of IL-1β. The production of IL-1β triggers a series of other events in the keratinocyte (effector state). These observations are consistent with the results shown in Fig. 2A. The neonatal NHEK are continuously producing higher levels of $^{\bullet}$NO and IL-1β. Therefore, these cells are always in a resting, activated, or effector state. However, when neonatal NHEK are exposed to HD the cells go directly into the refractory state either from the resting state or the effector state. In the refractory state the IL-1 receptors are downregulated consistent with the results in Figure 2B. In both cases NOCl could be produced leading to cell damage and DNA alkylation.

REFERENCES

BLANTON, B., KUPPER, T.S., McDOUGALL, J., and DOWER, S. (1989). Regulation of interleukin-1 and its receptor in human keratinocytes. Proc. Natl. Acad. Sci. USA **86,** 1273–1277.

CORBETT, J.A., LANCASTER, J.R., SWEETLAND, M.A., and McDANIEL, M.L. (1993). A 1-hour pulse with IL-1β induces formation of nitric oxide and inhibits insulin secretion by rat islets of Langerhans: Evidence for a tyrosine kinase signaling mechanism. FASEB J. **7,** 369–374.

CORBETT, J.A., LANCASTER, JR., J.R., SWEETLAND, M.A., and McDANIEL, M.L. (1991). Interleukin 1β-induced formation of EPR-detectable iron-nitrosyl complexes in islets of Langerhans. Role of nitric oxide in interleukin-1β-induced inhibition of insulin secretion. J. Biol. Chem. **266,** 21351–21354.

DINARELLO, C.A. (1991). Interleukin-1 and interleukin-1 antagonism. Blood **77,** 1627–1652.

FUKUTO, J.M. and CHAUDHURI, G. (1995). Inhibition of constitutive and inducible nitric oxide synthase: potential selective inhibition. Annu. Rev. Pharmacol. Toxicol. **35,** 165–194.

HUGHES, J.H., COLCA, J.R., EASOM, R.A., TURK, J., and McDANIEL, M.L. (1990). Interleukin-1 inhibits insulin secretion from isolated rat pancreatic islets by a process that requires gene transcription and mRNA translation. J. Clin. Invest. **86,** 856–863.

HUNYADI, J., SIMON JR., M., and DOBOZY, A. (1992). Immune-associated surface markers of human keratinocytes (minireview). Immunol. Lett. **31,** 209–216.

KOLB, H. and KOLB-BACHOFEN, V. (1992). Nitric oxide: A pathogenic factor in autoimmunity. Immunol. Today **13,** 157–160.

KOPPENOL, W.H. (1994). Thermodynamic concentrations on the formation of reactive species from hypochlorite, superoxide and nitrogen monoxide. Could nitrosyl chloride be produced by neutrophils and macrophages? FEBS Lett. **347,** 5–8.

KUPPER, T.S. (1989). Mechanisms of cutaneous inflammation. Arch Dermatol. **125,** 1406–1411.

KUPPER, T.S. (1990). Role of epidermal cytokines, in: *Immunophysiology. The Role of Cells and Cytokines in Immunity and Inflammation.* J.J. Oppenheim and E.M. Shevach (eds.) Oxford University Press: NY, pp. 285–305.

KUPPER, T.S., LEE, F., BICHALL, N., CLARK, S., and DOWER, S.K. (1989). Interleukin-1 binds to specific receptors on human keratinocytes and induces granulocyte macrophage colony-stimulating factor mRNA and protein. J. Clin. Invest. **82,** 1787–1792.

LAWLEY, P.D. (1976). Carcinogenesis by alkylating agents. ACS Monograph **173,** (American Chemical Society, Washington, D.C.) 83–244.

LIESKE, C.N., KLOPCIC, R.S., GROSS, C.L., CLARK, J.H., DOLZINE, T.W., LOGAN, T.P., and MEYER, H.G. (1992). Development of an antibody that binds sulfur mustard. Immunol. Lett. **31,** 117–122.

NATHAN, C. and XIE, Q. (1994). Regulation of biosynthesis of nitric oxide. J. Biol. Chem. **269,** 13725–13728.

WILLIAMS, D.L.H. (1988). *Nitrosation.* Cambridge University Press: New York, pp. 1–36.

Address reprint requests to:
Commander, US Army Medical Research Institute of Chemical Defense
ATTN: MCMR-UV-DA/Dr. Arroyo
Aberdeen Proving Ground, MD 21010-5425.

Human & Experimental Toxicology (1997) 16, 334-342

Trichloroethylene radicals generated by ionizing radiation. An EPR/spin trapping study

Alasdair J Carmichael[1] and Linda Steel-Goodwin[2,3]

[1]*Applied Cellular Radiobiology Department, Armed Forces Radiobiology Research Institute, Bethesda, Maryland 20889-5603;* [2]*Biological Effects Group, Environmental and Occupational Toxicology Division, Armstrong Laboratory, Dayton, Ohio, USA*

Trichloroethylene (TCE) was exposed in the presence of the spin trap N-*tert*-butyl-α-phenyl nitrone (PBN, 0.1 M) to ionizing radiation from two different sources in an attempt to determine the origin of the spin-trapped radicals generating the EPR spectra in precision cut liver slices. TCE samples were irradiated with 18 MeV electrons to a total dose of 1000 Gy in a linear accelerator (LINAC) or exposed to ^{60}Co γ-rays to total doses of 100 Gy and 1000 Gy. The results show that three PBN adducts were generated during the LINAC radiations. Two of these spin adducts correspond to the addition of carbon-centered radicals to PBN, and the third adduct is consistent with a decomposition product of PBN. The predominant carbon-entered radical yields a PBN adduct that is more stable, persists for over 24 h and has identical hyperfine coupling constants (a_N=1.61 mT, a_H^β=0.325 mT) to the PBN adduct obtained when precision-cut liver slices were exposed to TCE. Gamma radiation (100 Gy) of TCE yields PBN adducts with lower primary nitrogen hyperfine coupling constants (a_N=1.45 mT and a_N=1.54 mT). The results (γ-radiation) suggest that the carbon-centered radical is formed on a single TCE carbon that is different than the predominant radical formed during LINAC radiations. This difference is confirmed by experiments using ^{13}C-TCE. The results further suggest that, during γ-radiation of TCE, the radicals are formed by dechlorination at the TCE carbon containing two chlorine atoms. The results obtained during LINAC radiations suggest that the predominant radical is formed by dechlorination at the TCE carbon containing a single chlorine and a single proton. In addition, it is possible that this radical is the initial TCE radical formed during exposure of liver slices to TCE.

Keywords: free radicals; trichloroethylene; EPR; spin trapping; ionizing radiation

Introduction

Trichloroethylene (TCE) is a degreasing agent and an environmental contaminant. The management of solid waste containing 0.5 mg/L TCE (CAS No. 79-01-6) is controlled through the Resource Conservation and Recovery Act (RCRA) 1976. RCRA involves very specific rules for the generation, transportation, treatment, storage, or disposal of TCE waste. These rules are required for TCE because *in vivo* experiments have determined that TCE has a characteristic toxicity in rodents, and the data have been used by regulatory agencies to assess human and environmental risks.[1,2]

The experimental information on the extent to which TCE-induced adverse effects in rodents is due to the parent TCE compound, TCE metabolites, interaction of TCE with biological membranes, or a combination of these effects remains a major challenge in toxicological studies.[3-12]

Recent *in vitro* liver slice studies suggested that metabolism of TCE involves free radical pathways.[13] Free radicals are compounds containing an unpaired electron and their reactions occur naturally in biological systems.[14-19] In the normally functioning cell free radical levels are balanced, however, when this balance is altered a chain of events can occur that lead to deleterious effects.[16] Based on studies with chloral hydrate, the ultimate deleterious effects of TCE-induced free radicals are assumed to be lipid peroxidation.[20] Lipid peroxidation can be estimated by measuring conjugated dienes or malondialdehyde.[15,21,22] A recent report indicated that the formation of conjugated dienes in liver slices exposed to various concentrations of TCE was directly related to the formation of free radicals.[13] However, in this report only the formation of free radicals was shown, but their origin was not elucidated due to the large number of possibilities that exists when attempting to determine free radicals generated in the liver. The objective of this study was to better understand the process leading to the generation of free radicals detected in the liver. For this reason the focus of the present study

Correspondence: AJ Carmichael, PhD
[3]Current address: Air Force Office of Scientific Research, Academic and International Affairs, 110 Duncan Avenue, Suite B115, Bolling Air Force Base, DC 20332-8080
Received November 1996; revised March 1997; accepted April 1997

is to generate TCE radicals under controlled conditions using ionizing radiation and compare them to those observed in tissue experiments. The aim is to determine the initial TCE radicals formed. To accomplish this, the techniques of electron paramagnetic resonance (EPR) spectroscopy/spin trapping were used.[23,24] Spin traps are usually nitroso or nitrone compounds that give stable nitroxide radicals as adducts.[14,15] Stable nitroxide formation allows spin traps to be used as probes of radical reactions as well as detection by EPR spectroscopy.

Free radicals can be generated by hydrolysis, heat, radiation, ultrasound, and enzyme catalysis.[15,25,26] In this study, ionizing radiation was used to induce free radicals of the parent TCE compound, and the radicals detected were compared to the radicals detected in the bathing solution of liver slices incubated *in vitro* in the presence of TCE.

Materials and methods

TCE and N-*tert*-butyl-α-phenyl nitrone (PBN) were purchased from Aldrich Chemical Co., Inc. Milwaukee, WI. Randomly labeled ^{13}C-TCE (~50% ^{13}C label at each TCE carbon) was obtained from CDN Isotopes, Quebec, Canada.

PBN was dissolved at a concentration of 0.1 M in TCE (>99%) and irradiated in a linear accelerator (LINAC) with 18 MeV electrons to a total dose of 1000 Gy. PBN solutions in TCE (>99%) were also irradiated in a ^{60}Co gamma source to total doses of 100 and 1000 Gy.

Energy deposition into the sample from the ionizing radiation causes bond cleavage. This creates TCE radicals that subsequently yield spin adducts following their reaction with PBN. The TCE samples were exposed to pulsed 18 MeV electrons generated in the LINAC (1000 Gy total dose) and to γ-rays generated in a ^{60}Co source (1000 Gy total dose). Although the total radiation dose (1000 Gy) delivered to the sample is the same from the LINAC and the ^{60}Co source, it must be noted that LINAC radiation is pulsed electrons, and the total dose is the average dose over all pulses delivered to the sample. At any given pulse a much great instantaneous dose may be delivered to the sample. This greater instantaneous dose may cause different effects than those caused by ^{60}Co γ-radiation. In this case, the radiation field was homogeneous and continuous in delivering the total dose at a specific dose rate.

The irradiated samples were evaporated to dryness under a stream of nitrogen and then dissolved in Waymouth's MB 752/1 medium (Gibco Lab. Grand Island, NY) to mimic the environment of the spin adducts generated in the presence of liver slices described elsewhere.[13] Preparation of the liver slices and the Waymouth's medium is also described in a previous report.[13] Spin adduct EPR spectra were obtained immediately after dissolution into the Waymouth's medium.

^{13}C-labeled TCE solutions (>99% TCE; 99.3 atom % ^{13}C) containing PBN (0.1 M) were irradiated with ^{60}Co γ-rays to a total dose of 100 Gy, and their EPR spectra were obtained directly from the irradiated solutions.

EPR is a magnetic resonance technique which gives information on the molecular environment surrounding an unpaired electron (e.g. free radicals, transition metals) by measuring the effect of a magnetic field on the unpaired electron. Since the electron and nuclei act as small magnets, the interaction of external magnetic field with the unpaired electron is affected by the neighboring nuclei. Therefore, each species being measured yields a different EPR spectrum. In general free radicals are highly reactive and short lived and cannot be measured directly in solution by EPR. However, in this case the technique of spin trapping is used. Spin trapping consists of reacting a short lived free radical with a spin trap, usually a nitrone or nitroso compound, to yield a longer lived nitroxide radical (spin adduct) which can be measured and identified by EPR.

All EPR spectra were recorded on a Bruker ESP300E spectrometer or a Varian E-109 X-band spectrometer at a 100 kHz magnetic field modulation. Unless otherwise stated, the magnetic field was set at 335.0 mT, microwave frequency 9.51 GHz, microwave power 20 mW, modulation amplitude 0.1 mT, time constant 0.5 s, scan time 4 min and scan range 10.0 mT. Spectral parameters were obtained by computer simulation generating theorectical EPR spectra that matched the experimental spectra.

Results

TCE was exposed in the presence of PBN (0.1 M) to ionizing radiation from two different sources in an attempt to determine the origin of the spin-trapped radicals generating the EPR spectra in precision cut liver slices. Exposure of precision-cut liver slices to TCE in the presence of the spin trap PBN generated an EPR spectrum consisting of two superimposed spin adduct EPR spectra which have been described elsewhere.[13] In that report, the more intense spin adduct EPR spectrum was computer simulated using the hyperfine coupling constants a_N=1.61 mT and a_H^β=0.325 mT. For the less intense spin adduct EPR spectrum a small primary nitrogen hyperfine coupling was observed, however, no computer simulation was possible for that spectrum due to the weak nature of the EPR signals.

The EPR spectrum obtained after LINAC radiation (1000 Gy) of the TCE samples is shown in Figure 1a. The irradiated samples were evaporated to dryness under a stream of nitrogen and the residual powder containing the PBN adducts was dissolved in Waymouth's medium used in the experiments with the liver slices.[13] The EPR spectrum (Figure 1a) consists of three superimposed spin adduct EPR spectra. Figure 1b shows the computer-generated EPR spectrum that matches the experimental EPR spectrum in Figure 1a. This spectrum was obtained by addition of the computer-generated EPR spectra used to stimulate each of the PBN spin adducts formed.

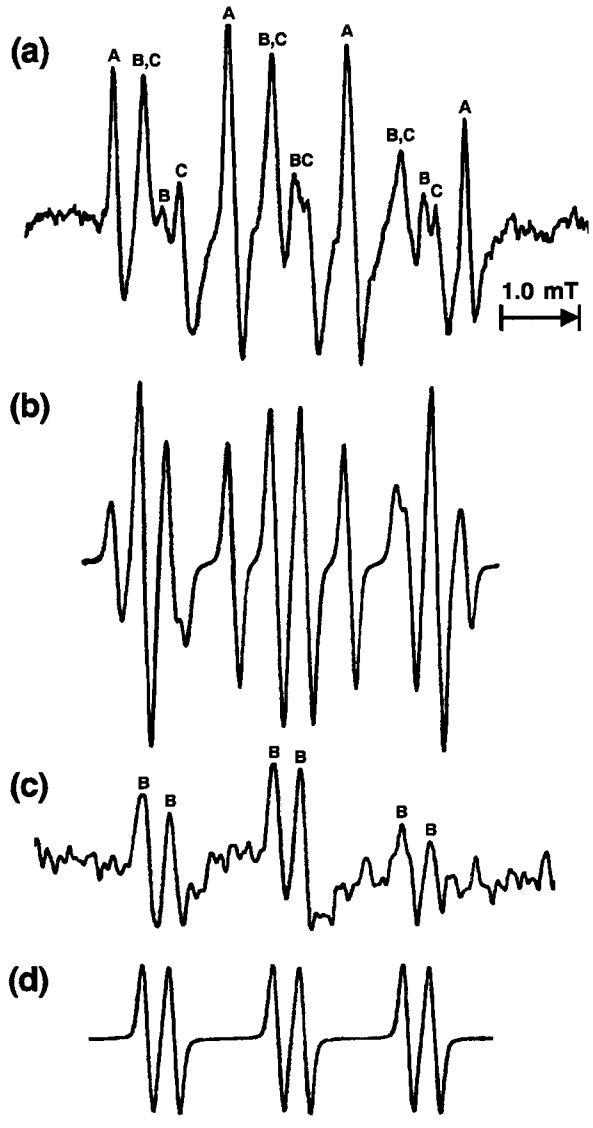

Figure 1 (**a**) EPR spectrum of PBN spin adducts obtained after irradiation of TCE with 18 MeV electrons in the LINAC. Sample was irradiated and immediately dried under a stream of nitrogen and then redissolved in Waymouth's medium; (**A**), (**B**) and (**C**) show three different spin adducts identified. (**b**) Computer-simulation that best matches the experimental spectrum in (**a**). This theorectical spectrum was obtained by the addition of three theorectical spectra that best match the EPR of the individual adducts. (**c**) EPR spectrum obtained after the sample in (**a**) was left at room temperature for 24 h. (**d**) Computer simulation of spectrum in (**c**) See Table 1 for spin adducts labeled **a**, **b** and **c**.

The first spin adduct identified consists of a 1:2:2:1 quartet labeled A in Figure 1a. The 1:2:2:1 quartet indicates that the unpaired electron interacts equally or similarly with the nuclei of primary nitrogen and secondary hydrogen; it is computer simulated using hyperfine coupling constants $a_N=a_H^{\beta}=1.41$ mT. These values are consistent with the reported values for the reduction product of the nitroso spin trap 2-methyl-2-nitrosopropane (MNP).[14,27] This spin adduct originates from the decomposition of PBN or by a rearrangement of a PBN spin adduct producing a *tert*-butyl amynoxyl group. Addition of a proton to the aminoxyl nitrogen yielded the reduction product of the nitroso spin trap MNP. Decomposition of PBN yielding the *tert*-butyl aminoxyl group has been observed previously by Arroyo *et al.*, in the reaction of PBN with phosgene.[27]

The second spin adduct identified yields the EPR spectrum labeled B in Figure 1a. This EPR spectrum consists of a triplet of doublets indicating that the unpaired nitroxide electron is interacting with the nuclei of a primary nitrogen and a β-hydrogen. It is computer simulated using hyperfine coupling constants, $a_N=1.61$ mT and $a_H^{\beta}=0.325$ mT. These values are identical to the values obtained for the predominant spin adduct generated when liver slices are exposed to TCE. This strongly suggests that the spin adducts generating the EPR spectrum labeled B in Figure 1a and in the liver slices originated from the same TCE radical.[13]

The third spin adduct identified is labeled C in Figure 1a also consists of a triplet of doublets. It is weak in nature and was computer simulated using hyperfine coupling constants $a_N=1.54$ mT and $a_H^{\beta}=0.43$ mT. It is possible that this TCE adduct corresponds to the low intensity adduct observed in the precision-cut liver slices exposed to TCE.[13]

The triplet of doublets with labeled B in Figure 1a is persistent and decays slightly over a period of 24 h. Figure 1c shows the remaining EPR spectrum obtained after the sample used in Figure 1a was left at room temperature for 24 h. The computer simulation for this stable spin adduct was obtained using hyperfine coupling constants $a_N=1.61$ mT and $a_H^{\beta}=0.325$ mT (Figure 1d). These values were identified to those used to simulate the EPR spectra in Figure 1a and to those from the EPR spectra generated by liver slices exposed to TCE.[13] Because the hyperfine coupling constants for the EPR spectra in Figures 1a and c are equal suggests that no rearrangement occurs over time to form other possible spin adducts.

TCE exposed in the presence of PBN to γ-irradiation (1000 Gy) generated the spin adduct EPR spectrum in Figure 2a. Similar to the weak EPR spectrum in Figure 1, this EPR spectrum

consists of a triplet of doublets and is computer simulated using hyperfine coupling constants a_N=1.54 mT and a_H^β=0.43 mT (Figure 2b). Since only the spin adduct with hyperfine coupling constants a_N=1.54 mT and a_H^β=0.43 mT was observed in both the LINAC (Figure 1) and gamma (Figure 2) radiation experiments, it was assumed that these spin adducts have the same origin and were formed on the same TCE carbon atom. However, since the prominent triplet of doublets (a_N=1.61 mT and a_H^β=0.325 mT) in Figure 1 was only formed in the LINAC radiation and not during the γ-radiation of TCE (Figure 2), the results suggested that the triplet of doublets observed in Figure 2a and the triplet of doublets observed in Figure 1a and c originated from radicals formed on different TCE carbons. Because of the nature of the TCE molecule, it is conceivable that various TCE radicals could be formed during exposure of this molecule to ionizing radiation. However, no transformation is observed over time in the EPR spectra consisting of triplet of doublets in Figures 1a and 2a, suggesting therefore that the spin adducts observed are chemically the most stable forms originating from any of the possible progenitor

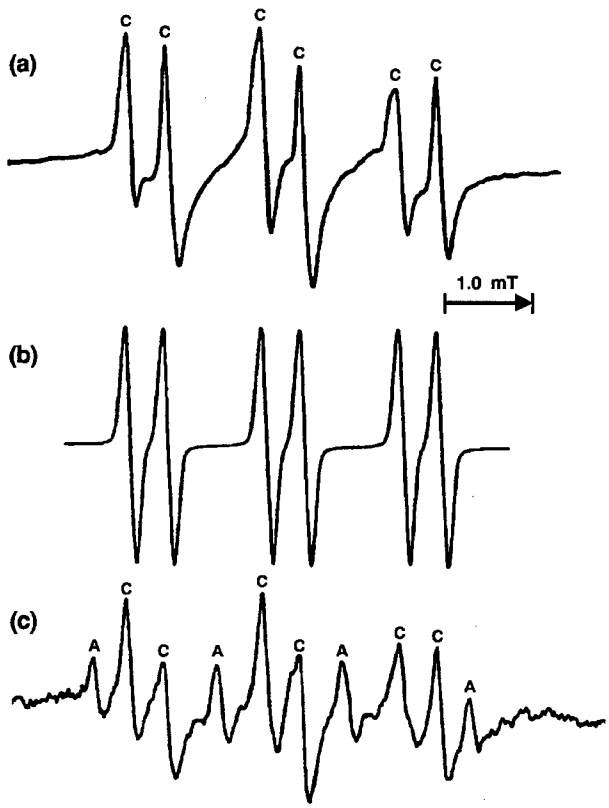

Figure 2 (**a**) EPR spectrum obtained after γ-radiation (1000 Gy) of TCE in the presence of PBN (0.1 M). Sample was irradiated and immediately dried under a stream of nitrogen then dissolved in Waymouth's medium. (**b**) Computer simulation that best matches the spectrum in (**a**). (**c**) EPR spectrum after the sample in (**a**) was left at room temperature for 24 h. See Table 1 for spin adducts labeled **A** and **C**.

TCE radicals. Figure 2c shows the EPR spectrum recorded 24 h after measurement of the sample which yielded the EPR spectrum in Figure 2a. This EPR spectrum (Figure 2c) consists of two superimposed spin adduct EPR spectra. One formed a triplet of doublets which was computer-simulated using the same hyperfine coupling constants (a_N=1.54 mT, a_H^β=0.43 mT) as those used to simulate the EPR spectrum in Figure 2a. The second spin adduct consisted of a 1:2:2:1 quartet and is simulated using hyperfine coupling constants a_N=a_H^β=1.41 mT. Similar to the case observed in Figure 1a, this 1:2:2:1 quartet originated from the decomposition of PBN or a PBN adduct yielding the *tert*-butyl aminoxyl-type radical corresponding to the reduction product of 2-methyl-2-nitrosopropane. The 1:2:2:1 quartet in Figure 2c is not formed immediately during the radiation of the TCE samples as occurred in the experiments described in Figure 1. The immediate observation of the 1:2:2:1 quartet (Figure 1a) after LINAC radiation and its appearance over time after γ-irradiation (Figure 2c) make it unlikely that this quartet originated solely from the decomposition of PBN. For this reason, the results suggested that the 1:2:2:1 quartet may be formed as a by-product of PBN adduct decomposition, during PBN adduct rearrangement, or both. This was supported by the observed decay of the triplet of doublets in Figure 2a and the simultaneous appearance of the 1:2:2:1 quartet (Figure 2c), suggesting that the 1:2:2:1 quartet is formed during decomposition of the spin adduct generating the triplet of doublets in Figures 2a and c. In addition, it must be noted that the samples were irradiated to an equal total dose in the LINAC and in the ^{60}Co source (1000 Gy) but generated different final spin adducts that do not interconvert over time from one to the other. This strongly supported the notion that the initial TCE radicals generated in both types of radiation experiments are different. Since TCE contains only two carbon atoms, a simple explanation for the above observations is that the initial radicals are formed predominantly on different TCE carbon atoms.

Additional information regarding the nature of the initial TCE radicals formed is obtained when this chemical was exposed to a lower dose of γ-radiation. Figure 3a shows the EPR spectrum obtained when TCE containing PBN (0.1 M) was exposed to γ-radiation at a total dose of 100 Gy. The computer simulation of the experimental spectrum (Figure 3a) is shown in Figure 3b and was obtained using hyperfine coupling constants a_N=1.45 mT and a_H^β=0.32 mT. These parameters are different from the hyperfine coupling constants (a_N=1.54 mT and a_H^β=0.43 mT) used to simulate the triplet of doublets (Figure 2a) obtained after γ-radiation

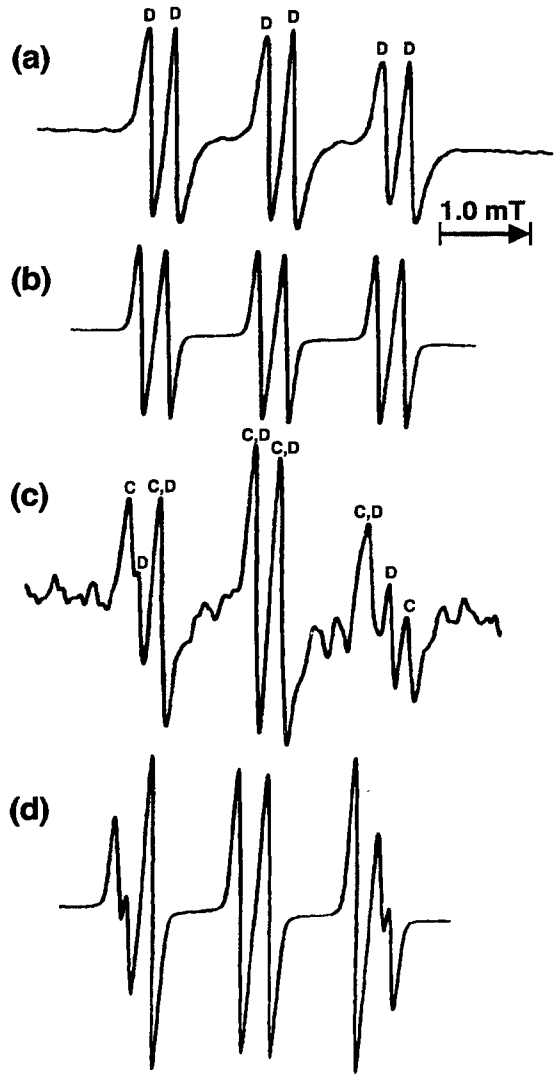

Figure 3 EPR spectra obtained after γ-radiation (100 Gy) of TCE in the presence of PBN. (**a**) EPR spectrum recorded following radiation, drying sample with a stream of nitrogen and dissolving in Waymouth's medium. (**b**) Computer simulation that best matches the experimental spectrum in (**a**). (**c**) Spectrum recorded 24 h after radiation. (**d**) Computer simulation that best matches the experimental spectrum in (**c**). See Table 1 for spin adducts labeled **C** and **D**.

(1000 Gy) of TCE. Figure 3c shows the EPR spectrum obtained for the sample 24 h after recording the spectrum in Figure 3a. The EPR spectrum in Figure 3c consists of two superimposed spin adduct EPR spectra. One of the spin adducts was simulated using hyperfine coupling constants a_N=1.45 mT and a_H^β=0.32 mT (Figure 3d), corresponding to the spin adduct described in Figure 3a. The second spin adduct was computer-simulated using hyperfine coupling constants a_n=1.54 mT and a_H^β=0.43 mT (Figure 3d). Figure 3d consists of the EPR spectrum obtained after adding the computer-simulated EPR spectra that best match the experimental EPR spectrum in Figure 3c. The hyperfine coupling constants a_N=1.54 mT and a_H^β=0.43 mT (Figure 3d) are identical to those used to simulate EPR spectrum in Figure 2a, suggesting that these adducts are the same. Therefore, the observed loss in intensity in the EPR spectrum in Figures 3a and c (a_N=1.45 mT and a_H^β=0.32 mT) and the increase in intensity of the additional spin adduct EPR spectrum (a_N=1.54 mT and a_H^β=0.43 mT) (Figure 3c), strongly suggested that over time the spin adduct generating the EPR spectrum in Figure 3a is rearranged to the spin adduct observed in Figure 2a. The results in Figure 2 do not show any further rearrangement of the spin adduct (a_N=1.54 mT and a_H^β=0.43 mT) and suggested that this was chemically the more stable adduct. It is possible that the higher deposition of energy into the TCE from γ-radiation (1000 Gy) was sufficient for this adduct to be formed directly or possibly making the initial TCE adduct (Figure 3a) observed at 100 Gy more unstable and prone to decomposition.

The data suggests that the single spin adduct obtained during γ-radiation of TCE (Figure 2a) corresponds to the spin adduct obtained during LINAC radiation (Figure 1), which yielded the weaker triplet of doublets EPR spectrum. It is also

Table 1 EPR parameters of PBN-TCE spin adducts

Treatment	*Time (h)*	*a_N (mT)*	*a_H^β (mT)*	*Radical*	*Figure*	*Eqn*[a]
Liver Slice[b]	–	<1.61	–	C?	1	2.4
Liver Slice[b]	–	1.61	0.325	B	1	3
LINAC	0	1.41	1.41	A	1a	–
LINAC	0	1.61	0.325	B	1a	3
LINAC	0	1.54	0.43	C	1a	4
LINAC	24	1.61	0.325	B	1c	3
^{60}Co-γ[c]	0	1.54	0.43	C	2a	4
^{60}Co-γ[c]	24	1.41	1.41	C	2c	–
^{60}Co-γ[c]	24	1.54	0.43	C	2c	4
^{60}Co-γ[d]	0	1.45	0.32	D	3a	2.4
^{60}Co-γ[d]	24	1.45	0.32	D	3c	2.4
^{60}Co-γ[d]	24	1.54	0.43	C	3c	4

[a]Proposed structures based on EPR data and nature of the TCE molecule. [b]Liver slices exposed to TCE (taken from Reference 13). [c]1000 Gy total dose of ^{60}Co-γ-radiation. [d]100 Gy total dose of ^{60}Co-γ-radiation

possible that this spin adduct corresponds to the spin adduct generating the weak EPR signal appearing as shoulders in the EPR spectra obtained from the exposure of liver slices to TCE.[13] In this case it was not possible to simulate the weak EPR signals formed during exposure of liver slices to TCE. However, the spectra were similar in having a lower primary nitrogen hyperfine coupling constant (a_N=1.54 mT for γ-radiation) when compared to the prominent triplet of doublets observed during liver slice exposure to TCE (a_N=1.61 mT). The EPR parameters for the various TCE radicals observed are summarized in Table 1.

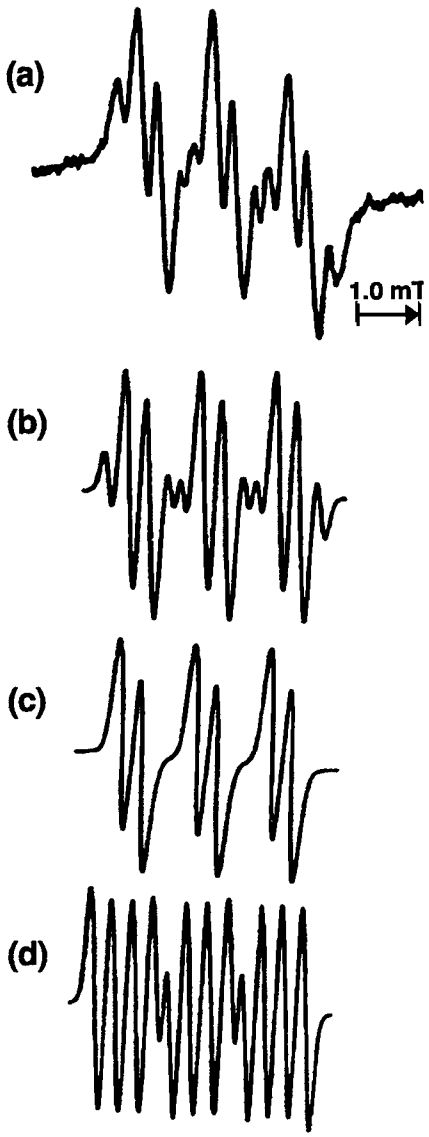

Figure 4 (**a**) EPR spectrum obtained after γ-radiation (100 Gy) of ^{13}C-labeled TCE in the presence of PBN. This spectrum was recorded in TCE immediately following irradiation. (**b**) Computer simulation that best matches the experimental EPR spectrum in (**a**). This spectrum was obtained by addition of the spectra in (**c**) and (**d**), which illustrate the computer simulations that best match the EPR of the individual spin adducts identified in (**a**).

Further information to verify TCE radical formation at a single carbon when exposed to γ-radiation can be obtained using ^{13}C-labeled TCE. Since the purpose of these experiments was to support the notion that γ-radiation generated a radical only on one of the TCE carbons, it was not necessary to evaporate the samples to dryness and dissolve them in the Waymouth's medium. The results in Figure 4 were obtained following γ-radiation of randomly labeled ^{13}C-TCE in the presence of PBN. Figure 4a consists of two superimposed PBN spin adduct EPR spectra. One is a triplet of doublets which originated from an adduct formed by the addition of a nonlabeled TCE carbon atom to PBN. This EPR spectrum was simulated using hyperfine coupling constants a_N=1.42 mT and a_H^{β}=0.39 mT. The second spin adduct consisted of a triplet of quartets due to the interaction of the unpaired nitroxide electron with the nucleus of a β-hydrogen and the nucleus of a β-^{13}C atom (I_{13_C}=1/2). This spin adduct EPR spectrum was simulated using hyperfine coupling constants a_N=1.42 mT, a_H^{β}=0.39 mT, and $a_{13_C}^{\beta}$=0.78 mT. Because the TCE was randomly labeled (approximately 50% label at each TCE carbon), a single triplet of quartets is consistent with the trapping of a radical formed on a single TCE carbon during γ-radiation. Since both TCE

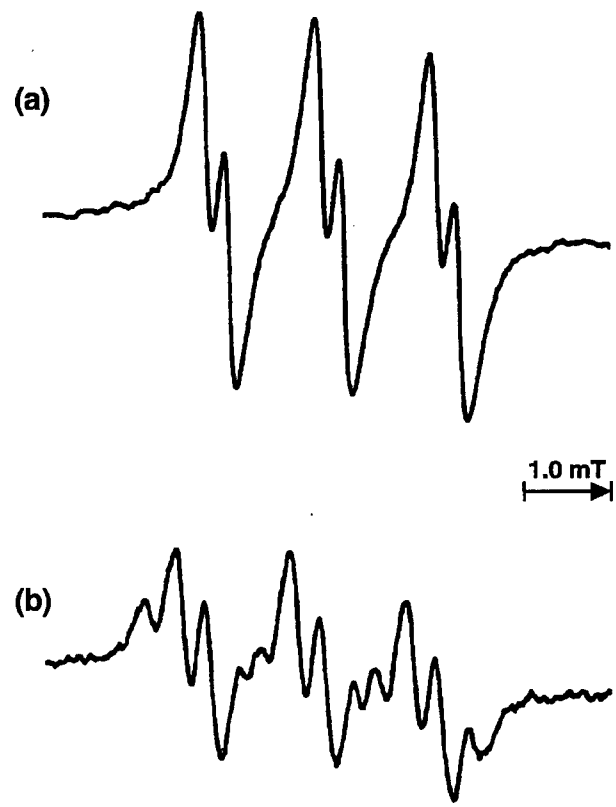

Figure 5 EPR spectra of TCE (**a**) and ^{13}C-labeled TCE (**b**) recorded with identical instrumental parameters immediately following γ-radiation (100 Gy) in the presence of PBN. Both spectra were recorded in TCE.

carbons contain different substituents and therefore are chemically different, if radical formation occurred on either TCE carbon during γ-radiation it would be expected that dechlorination and radical formation would yield an EPR spectrum containing two distinct triplets of quartets (different ^{13}C hyperfine interactions). The first triplet of quartets would correspond to one TCE carbon while the second triplet of quartets would correspond to the other TCE carbon. However, since this is not the case and only a single triplet of quartets was observed, the result in Figure 4a strongly suggests that dechlorination and radical formation occurs at a single carbon during γ-radiation. It is also important to note that each component in Figure 4a has approximately equal intensity and that the combined intensity of both spin adduct EPR spectra (Figure 4a) was approximately equal to the intensity of the EPR spectrum obtained under the same conditions during γ-radiolysis of the unlabeled TCE (Figure 5). The results in Figures 4 and 5 strongly support TCE radical formation on a single carbon during exposure to γ-radiation. Furthermore, the results from the γ-radiation experiments (Figures 3–5) showed that the TCE radical was not formed on the same carbon atom as the radical generating the predominant spin adduct in the media bathing the liver slices and during the LINAC radiation (Figure 1).

Discussion

It is conceivable that the LINAC radiation of TCE generates a single primary TCE radical that may rearrange through its own instability by a reaction with some other component in the solution (e.g., oxygen). If this were the case, secondary radical products would be generated allowing PBN to compete for the progenitor radical and the radical product. This would yield two different spin adduct EPR spectra, although both spin adducts may have originated from radical formation on a single TCE carbon. However, these possibilities are unlikely due to the formation of a single spin adduct observed when TCE is exposed to γ-radiation (Figure 2), in addition to this spin adduct corresponding to one of the spin adducts obtained in LINAC radiation. Therefore, the results suggest that radicals are formed independently on both TCE carbons by dechlorination and depend on the type of radiation to which the TCE solutions are exposed.

Initial dechlorination induced by ionizing radiation can generate two different TCE radicals (Equations 1 and 2, See below).

The formation of two different PBN-TCE spin adducts (Figure 1) during the LINAC radiation is consistent with initial dechlorination occurring at both the TCE carbon atoms. It should be expected that the reaction of PBN with the radical formed in *equation 1* would generate a spin adduct with no chlorine (only a double bond) in the proximity of the nitroxide group. The absence of a chlorine (with electron withdrawing properties) in the immediate vicinity of the nitroxide would allow a greater interaction between the unpaired nitroxide electron and the nitrogen nucleus. A larger interaction of the unpaired nitroxide electron with the nitrogen nucleus translates into a larger primary nitrogen hyperfine coupling constant. On the other hand, the reaction of PBN with the radical formed in *equation 2* would yield a spin adduct in which the unpaired nitroxide electron is shifted away from the nitrogen due to the electron withdrawing properties of the neighboring chlorine and the double bond. This being the case, the interaction of the unpaired nitroxide electron

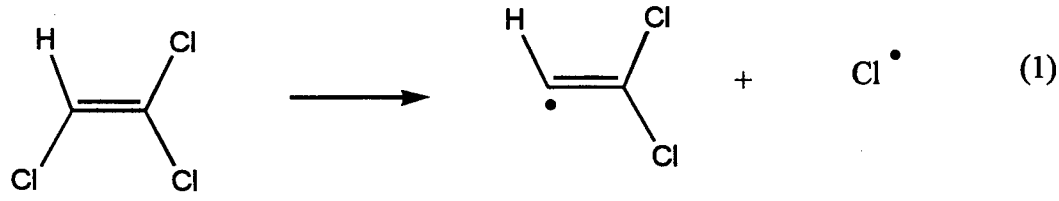

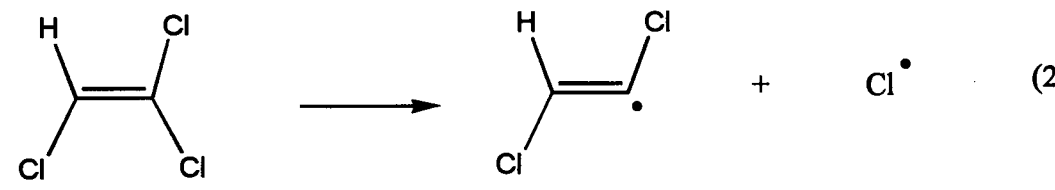

with the nitrogen nucleus would be decreased, therefore generating a spin adduct EPR spectrum with smaller primary nitrogen hyperfine coupling constants. Therefore, it is concluded that the PBN adduct trapped and simulated with the larger nitrogen coupling, a_N=1.61 mT, originates from the reaction of $H^{\bullet}C{=}CCl_2$ with PBN (Equation 1) and is the predominant radical observed when exposing liver slices to TCE. It is concluded for the reasons given above that the spin adduct EPR spectra simulated using a nitrogen coupling, a_N=1.45 mT, correspond to the single PBN adduct formed during γ-radiolysis (100 Gy) of TCE (Figure 3a). This adduct originates from the reaction of the $ClHC{=}C^{\bullet}Cl$ radical with PBN (Equation 2). The above adducts may be stable in an aprotic environment; however, both adducts formed in the reaction of PBN and the radical products in *equations 1 and 2* appear to be unstable in an aqueous environment and possibly rearrange as seen in Figure 3c and d. This rearrangement which is formally a reduction yields the final products observed in Figures 1–3 and in *equations 3 and 4*. Based on the EPR data and the nature of the TCE molecule the proposed structures for the PBN adducts (labeled B, C, D, in Table 1) are given in *equations 3 and 4* (see below).

The slight increase in the primary nitrogen hyperfine from a_N=1.45 mT to a_N=1.54 mT as observed in *equation 4*, is consistent with the breaking of the C=C double bond, leaving only the chlorine to pull the unpaired electron away from the nitroixde nitrogen.

Assignment of the $H^{\bullet}C{=}CCl_2$ radical (Equation 1) as the initial and predominant radical generated during exposure of the liver slices to TCE appears reasonable for various reasons. This vinyl-type radical should be sufficiently reactive to abstract a hydrogen atom from a polyunsaturated fatty acid to initiate the previously observed conjugated diene formation.[15] Conjugated diene formation is initiated by the interaction of a primary radical with a polyunsaturated fatty acid in the membrane.[15] The primary radical (e.g., hydroxyl, alkoxyl, peroxyl, alkyl) must be sufficiently reactive to abstract a hydrogen atom from the polyunsaturated fatty acid. In addition the vinyl-type radical (Equation 1) could rapidly react with oxygen forming a peroxyl-type radical that could also be responsible for initiating the reactions leading to the formation of the previously measured conjugated dienes.[15] It is also possible that such a TCE peroxyl-type intermediate may be the initial intermediate leading to the formation of various known TCE metabolites such as trichloroethanol and trichloroacetic acid.

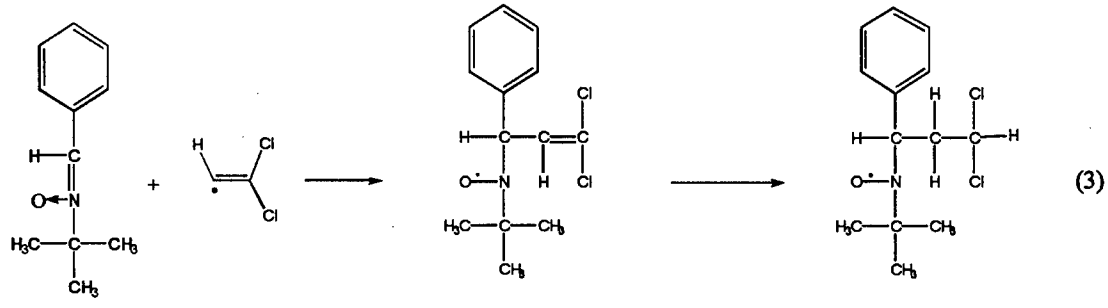

(a_N = ?)

(a_N = 1.61 mT)

B

(3)

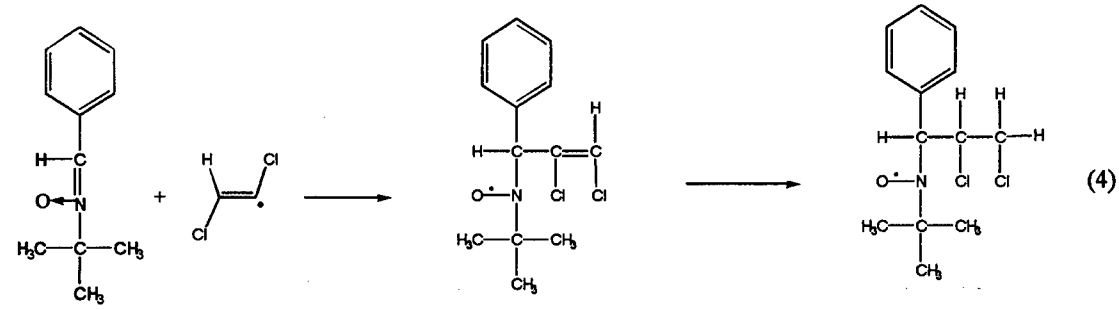

(a_N = 1.45 mT)

D

(a_N = 1.54 mT)

C

(4)

Acknowledgements

This work was supported in part by AFOSR work unit #2312A202 and AFRRI work unit #004630. The views expressed in this work are those of the authors and do not reflect those of any US Government Department.

References

1 National Cancer Institute. Carcinogenesis bioassay of trichloroethylene CAS No. 79-01-6. *DHEW Publication No* (NIH) 76-802, 1976.
2 National Toxicology Program. Carcinogenesis bioassay of trichloroethylene (CAS No. 79-01-6) in F3NN/N rats and B6C3F1 mice (gavage studies) 1982; *Technical Report No. 243*. Research Triangle Park, NC.
3 Costa AK, Katz ID, Ivanetich KM. Trichloroethylene: its interactions with hepatic microsomal cytochrome P-450 in vitro. *Biochemical Pharmacology* 1980; **29:** 433–439.
4 Berman K. Interactions of trichloroethylene with DNA in vitro and with RNA and DNA of various mouse tissues in vivo. *Archives of Toxicology* 1983; **54:** 181.
5 Elcombe CR. Species differences in carcinogenicity and peroxisome proliferation due to trichloroethylene: A biochemical human hazard assessment. Receptors & Other Targets for Toxic Substances. *Archives of Toxicology* 1985; **Suppl 8:** 6–17.
6 Dekant W, Schultz A, Metzler M, Henschler D. Absorption, elimination and metabolism of trichloroethylene: a quantitative comparison between rats and mice. *Xenobiotic* 1986; **16:** 143–152.
7 Gonthier BP, Barret LG. In vitro spin trapping of free radicals produced during trichloroethylene and diethyl ether metabolism. *Toxicology Letters* 1989; **47:** 225–234.
8 Fisher JW, Allen BC. Evaluating the risk of liver cancer in humans exposed to trichloroethylene using physiological models. *Risk Analysis* 1993; **13:** 87–95.
9 Fisher JW, Gargas ML, Allen BC, Anderson ME. Physiologically based pharmacokinetic modeling with trichloroethylene and its metabolite, trichloroacetic acid in the rat and mouse. *Toxicology and Applied Pharmacology* 1991; **109:** 183–195.
10 Larson JL, Bull RJ. Species differences in the metabolism of trichloroethylene to the carcinogenic metabolites trichloroacetate and dichloroacetate. *Toxicology and Applied Pharmacology* 1992; **115:** 278–285.
11 Bull RJ, Templin M, Larson JL, Stevens DK. The role of dichloroacetate in the hepatocarcinogenicity of trichloroethylene. *Toxicology Letters* 1993; **68:** 203–211.
12 Daniel FB *et al.* Hepatocarcinogenicity of chloral hydrate, 2-chloroacetaldehyde and dichloroacetic acid in the male B6C3F1 mouse. *Fundamental and Applied Toxicology* 1992; **19:** 159–168.
13 Steel-Goodwin L, Pravacek TL, Carmichael AJ. Trichloroethylene metabolism in vitro: an EPR/spin trapping study. *Human and Experimental Toxicology* 1996; **15:** 878–884.
14 Beuttner GR. Spin trapping: ESR parameters of spin traps. *Free Radical Biology and Medicine* 1987; **3:** 259–303.
15 Rice-Evans CA, Diplock AT, Symons MRC. Techniques in free radical research. In: Laboratory Techniques in Biochemistry and Molecular Biology (RH Burdon, PH van Knippenberg, (Eds.) Elsevier, NY, 1991.
16 Carmichael AJ, Steel-Goodwin L, Gray B, Arroyo CM. Reactions of active oxygen and nitrogen species studied by EPR and spin trapping. *Free Radical Research Communications* 1993; **19:** S1–S16.
17 Halliwell B. How to characterize a biological antioxidant. *Free Radical Research Communications* 1990; **9:** 1–2.
18 Reilly PM, Schiller HJ, Bulkley GB. Pharmacological approach to tissue injury mediated by free radicals and other reactive oxygen metabolites. *American Journal of Surgery* 1991; **161:** 488–503.
19 Gutteridge JMC. Free radicals in disease processes. A compilation of cause and consequence. *Free Radical Research Communications* 1993; **9:** 1–22.
20 Ni Y-C, Wong TY, Kadlubar FF, Fu PP. Hepatic metabolism of chloral hydrate to free radical(s) and induction of lipid peroxidation. *Biochemical and Biophysical Research Communications* 1994; **204:** 937–943.
21 Gardner HW. Effects of lipid hydroperoxides on food components. In: Xenobiotics in Foods and Feeds JW Finley, DE Schwass (Ed.) ACS Symposium Series 234, American Chemical Society, Washington DC, 1983.
22 Fraga CG, Leibovitz BE, Tappel AL. Lipid peroxidation measured as thiobarbituric acid reactive substances in tissue slices: characterization and comparison with homogenates and microscomes. *Free Radical Biology and Medicine* 1988; **4:** 155–161.
23 Mason RP. Spin trapping free radical metabolites of toxic chemicals. In: Spin Labeling in Pharmacology; Chapter 2 pp 87–129. 1984.
24 Knecht KT, Mason RP. Inhibition of radical adduct reduction and reoxidant of the corresponding hydroxylamines in in vivo spin trapping and carbon tetrachloride-derived radicals. *Free Radical Biology and Medicine* 1992; **13:** 151–160.
25 Carmichael AJ, Mossoba MM, Riesz P, Christman L. Free radical production in aqueous solutions exposed to simulated ultrasonic diagnostic conditions. *IEEE Transactions in Ultrasonics, Ferroelectrics, and Frequency Control* 1986; **Vol USSC-33,** 148–155.
26 von Sonntag C, Schuchmann H-P. The elucidation of peroxyl radical reactions in aqueous solution with the help of radiation-chemical methods. *Angewandte Chemie International Edition* 1991; **30:** 1229–1283.
27 Arroyo CM *et al.* Autoionization reactions of phosgene ($OCCl_2$) studied by electron paramagnetic resonance/spin trapping techniques. *Journal of Biochemical Toxicology* 1993; **8:** 107–110.

JOURNAL OF INTERFERON AND CYTOKINE RESEARCH 17:567–572 (1997)
Mary Ann Liebert, Inc.

Sublethal Gamma Irradiation Increases IL-1α, IL-6, and TNF-α mRNA Levels in Murine Hematopoietic Tissues

CHENG-MIN CHANG,[1] ALEX LIMANNI,[1,3] WILLIAM H. BAKER,[1,4] MICHAEL E. DOBSON,[1] JOHN F. KALINICH,[2] and MYRA L. PATCHEN[1,5]

ABSTRACT

The effects of sublethal (7.75 Gy) ^{60}Co gamma radiation exposure on endogenous bone marrow and splenic interleukin-1α (IL-1α), IL-6, and tumor necrosis factor-α (TNF-α) mRNA and protein levels were assayed in $B_6D_2F_1$ female mice. Bone marrow and spleen were harvested from normal and irradiated mice on days 2, 4, 7, 10, and 14 postexposure, and cytokine mRNA levels were determined by reverse transcription polymerase chain reaction (RT-PCR) and Southern blot analysis. IL-1α mRNA levels were significantly increased in bone marrow at days 2 and 4 postirradiation and at day 7 in spleen compared with controls. Postirradiation IL-6 mRNA levels showed a significant increase at day 2 in bone marrow and at days 7 and 10 in spleen. TNF-α mRNA levels exhibited a significant increase at day 2 postirradiation in bone marrow, but in spleen no difference between control and irradiated samples was observed on any day postirradiation. Interestingly, there were no significant differences in the cytokine protein levels in postirradiation bone marrow, spleen, or serum when compared with normal controls.

INTRODUCTION

Interleukin-1 (IL-1), IL-6, and tumor necrosis factor (TNF) are multifunctional cytokines involved in the regulation of hematopoiesis as well as immune and inflammatory responses. Hematopoiesis is a complex developmental process that is intricately regulated by the interaction of a variety of positive and negative growth factors. Although IL-1 and IL-6 alone do not stimulate the *in vitro* proliferation of hematopoietic cells, they can synergize with other colony-stimulating factors to induce proliferation of hematopoietic progenitor cells.[1,2] TNF-α, alone or in combination with interferon, has been shown to inhibit *in vitro* hematopoiesis.[3] A number of cell types, including macrophages/monocytes, T cells, B cells, keratinocytes, and endothelial cells, are able to synthesize and release these cytokines.[4,5] These cytokines can be stimulated *in vitro* by a variety of stimuli, including lipopolysaccharide (LPS) and radiation.[6–11] Molecular biology techniques can now evaluate the effects of radiation on *in vivo* cytokine expression. Following *in vivo* radiation exposure, the repopulation of murine bone marrow and spleen showed increased levels of c-kit ligand mRNA for several days postexposure.[12] Radiation exposure also increases GM-CSF mRNA levels in both murine bone marrow and spleen but does not affect bone marrow and splenic transforming growth factor (TGF)-β mRNA levels.[13]

IL-1, IL-6, and TNF do play a role in protecting animals from the detrimental effects of radiation.[14–16] In addition, IL-6 is also an important mediator of both IL-1-induced and TNF-induced hematopoietic recovery[17] and an important effector in accelerating multilineage recovery following radiation-induced hematopoietic aplasia mediated by granulocyte colony-stimulating factor (G-CSF).[15] To examine whether these cytokines act endogenously in recovery, we performed a series of experiments where both mRNA and protein levels in IL-1α, IL-6, and TNF-α were measured *in vivo* in a murine model in which a high sublethal radiation exposure was used to induce severe hematopoietic hypoplasia.

MATERIALS AND METHODS

Animals and irradiation conditions

All animal experiments were approved by the Institute Animal Care and Use Committee. $B_6D_2F_1$ female mice (~20 g)

Departments of [1]Radiation Medicine and [2]Applied Cellular Radiobiology, Armed Forces Radiobiology Research Institute, Bethesda, MD.
[3]Present address: Arthritis Centers of Texas, Dallas, TX.
[4]Present address: Walter Reed Army Institute of Research, Washington, DC.
[5]Present address: Alpha-beta Technology, Worcester, MA.

were purchased from Jackson Laboratories (Bar Harbor, ME) and irradiated in the Armed Forces Radiobiology Research Institute's ^{60}Co gamma radiation source. Irradiations were performed bilaterally to a total absorbed dose of 7.75 Gy at a dose rate of 0.4 Gy/min. Dosimetry was performed as described.[18]

Cells and tissues

After killing by cervical dislocation, femurs and spleens were harvested from normal and irradiated mice on days 2, 4, 7, 10, and 14 postirradiation. Tissues from 3 to 7 mice were pooled to obtain sufficient cells for each specific assay. Bone marrow cells were flushed from femurs with 3 ml of McCoy's 5A medium (Flow Labs, McLean, VA) containing 10% heat-inactivated fetal bovine serum (FBS) (HyClone Labs, Logan, UT). The number of nucleated cells in the bone marrow suspensions was determined by a Coulter Counter (Coulter, Hialeah, FL). Spleens were homogenized with a polytron homogenizer. To obtain serum from normal and irradiated mice on days 2, 4, 8, 10, 14, and 17 postexposure, animals were halothane-anesthetized, and blood was drawn by cardiac puncture using a syringe attached to a 20-gauge needle.

RT-PCR

Total RNA was extracted from bone marrow suspensions and homogenized spleens using the RNAzol method (Tel-Test Inc., Friendswood, TX) as modified by Chomczynski and Sacchi.[19] RNA concentrations were determined spectrophotometrically from absorbance at 260 nm. Total RNA of each sample was characterized by ethidium bromide-staining of agarose gels to ensure the use of only intact RNA. Intact total RNA was reverse transcribed into first strand complementary deoxyribonucleic acid (cDNA), which was then amplified by using polymerase chain reaction (PCR). The final volume of 5 μl reverse transcription (RT) reaction mixture contained 0.1 μg bone marrow total RNA or 0.5 μg splenic total RNA, 50 mM Tris-HCl (pH 8.3), 3 mM $MgCl_2$, 75 mM KCl, 2.5 μg/ml oligo$(dT)_{12-18}$, 1 mM each dATP, dGTP, dTTP, and dCTP, and 10 U Moloney murine leukemia virus reverse transcriptase. The reaction mixture for RT was incubated at 37°C for 1 h and 90°C for 10 min and chilled on ice for 10 min. The PCR primers of IL-1α, IL-6, and TNF-α were purchased from Clontech Laboratories, Inc. (Palo Alto, CA) and of GAPDH from Synthetic Genetics (San Diego, CA). The sequence of primers and expected product sizes are as follows:

IL-1α (625 bp)	5′-primer	5′-ATGGCCAAAGTTCCTGACTTGTTT-3′
	3′-primer	5′-CCTTCAGCAACACGGGCTGGTC-3′
IL-6 (638 bp)	5′-primer	5′-ATGAAGTTCCTCTCTGCAAGAGACT-3′
	3′-primer	5′-CACTAGGTTTGCCGAGTAGATCTC-3′
TNF-α (692 bp)	5′-primer	5′-ATGAGCACAGAAAGCATGATCCGC-3′
	3′-primer	5′-CCAAAGTAGACCTGCCCGGACTC-3′
GAPDH (195 bp)	5′-primer	5′-CCATGGAGAAGGCTGGGG-3′
	3′-primer	5′-CAAAGTTGTCATGGATGACC-3′

The reaction mixture for PCR contained 5 μl cDNA template from the RT reaction, 10 mM Tris-HCl (pH 8.3), 50 mM KCl, 1.5 mM $MgCl_2$, 0.8 mM each dATP, dGTP, dCPT, and dTTP, 1.0 μM 5′-primer, 1.0 μM 3′-primer, and 1.25 U *Taq* DNA polymerase. PCR was performed with a DNA Thermal Cycler (Perkin Elmer Cetus, Norwalk, CT). Denaturation was at 94°C for 1 min, annealing at 60°C for 2 min, and extension at 72°C for 3 min per cycle until the optimum number of cycles was reached. Reactions conditions were optimized individually for each cytokine. Southern transferase were performed as described.[13] The amplified products were electrophoresed in a 1% agarose gel in the presence of 1 μg/ml ethidium bromide, transferred onto Nytran membrane (Schleicher and Schuell, Keene, NH), and hybridized with the respective [^{32}P]-labeled murine IL-1α, IL-6, or TNF-α cDNA probe. The GAPDH mRNA levels were also determined to be used as a control for an equal amount of RNA loading. The probe for IL-1α was prepared as previously described.[20] The IL-6 probe consisted of a 0.65 kb insert cloned into the XhoI site of PXM (Genetics Institute, Cambridge, MA). The TNF-α probe contained a 1.38 kb insert cloned into the BamHI/PstI site of pGEM-3Z (Promega, Madison, WI), and the GAPDH probe was prepared as previously described.[12] Probes were labeled using a commercial nick-translation kit (Bethesda Research Laboratories, Gaithersburg, MD). Prehybridization was done in a solution containing 50% formamide solution, 6× SSC, 5× Denhardts, 50 mM Tris, 100 μg/ml salmon sperm DNA, and 1% SDS at 42°C. Overnight hybridization was done in the same solution after addition of the appropriate [^{32}P]-labeled cDNA probe. Subsequently, blots were washed three times at 42°C in a solution containing 2× SSC and 0.5% SDS (15 min each) and finally at 62°C in a solution containing 0.1× SSC and 0.1% SDS for 1 h. Autoradiographs were done at −70°C using Kodak XAR film. Both positive and negative control reactions showed the appropriate response.

Determination of protein levels

Bone marrow and splenic IL-α, IL-6, and TNF-α proteins were detected by the Western dot blot technique. Bone marrow single cell suspensions and splenic homogenate were placed on ice and disrupted by a 5 sec sonication (Heat Systems Cell Disrupter with Microtip, Farmingdale, NY). The method of Bradford[21] was used to determine protein concentrations. A modification of the method of Hawkes et al.[22] was used to determine the relative amounts of IL-1α, IL-6, and TNF-α in the cell homogenate. Briefly, 10 μg of total cellular protein was blotted onto a 0.45 μm nitrocellulose membrane (Schleicher and Schuell) for 1 h using a dot blotting apparatus (Bethesda Research Laboratories). After blocking the nitrocellulose by incubation for 60 min at ambient temperature with PBS containing 5% nonfat dried milk, the blot was incubated overnight at 4°C with a goat polyclonal antibody against respective recombinant murine IL-1α, IL-6, or TNF-α at 10 μg/ml in PBS/5% BSA containing 0.1% thimerosal. The blot was washed three times (10 min each) in PBS/0.1% Tween-20 before incubating for 60 min at ambient temperature with a 1000× dilution of rabbit antigoat IgG horseradish peroxidase conjugate (Sigma, St. Louis, MO) in 1% gelatin. The blot was then washed six times (5 min each) in PBS/0.1% Tween-20 before detection of

the peroxidase activity using the substrate 4-chloro-1-naphthol (Sigma) in the presence of hydrogen peroxide. After completion of the color reaction, the blots were washed with distilled water and dried. Commercial ELISA kits were used to measure the serum concentration of IL-6, IL-1α (Genzyme, Cambridge, MA), and TNF-α (Endogen, Cambridge, MA). Sera obtained from 10 normal or irradiated mice were pooled for use in this assay. Assays were performed according to the manufacturer's instructions after twofold dilution of the sera using the standard diluent supplied with the kit.

Quantitation

The densitometric volume of each sample was measured using a scanning laser densitometer (model 300B, Molecular Dynamics, Sunnyvale, CA), measuring the gray density of the entire PCR product band in each lane or color intensity of the dot blot in each well. The images were analyzed using ImageQuant software version 3.2 (Molecular Dynamics) supplied with the densitometer. PCR product and protein comparisons were then based on relative expression differences between irradiated and control samples.

Statistics

Data are expressed as a percentage of the unirradiated control for each experiment. Data were analyzed for statistical significance by means of the Student's t test. A p value of <0.100 was considered to be statistically significant.

RESULTS

Effects of radiation on IL-1α, IL-6, TNF-α, and GAPDH mRNA levels

A representative autoradiograph of bone marrow and spleen RT-PCR-amplified IL-1α, IL-6, TNF-α, and GAPDH mRNA transcripts from control and irradiated (7.75 Gy) mice is shown in Figure 1. The density of the autoradiographic bands was determined by laser densitometry, and the values were normalized to the control for each group. The average relative IL-1α, IL-6, and TNF-α mRNA levels of bone marrow and spleen are shown in Figures 2 and 3, respectively. Bone marrow IL-1α mRNA levels increased approximately 9-fold and 18-fold over controls by days 2 and 4 postirradiation, respectively. It showed a gradual decrease thereafter. Splenic IL-1α mRNA levels also increased after radiation exposure, but not to the extent seen in bone marrow. A 5-fold increased over control was observed on day 7 postirradiation, after which levels returned to normal. Bone marrow IL-6 mRNA levels were approximately 6-fold greater than controls on day 2 postirradiation but decreased in the following days. On the other hand, splenic IL-6 mRNA levels were near control levels until days 7 and 10 postirradiation, when they increased to about 5-fold and 6-fold over controls before returning to normal on day 14.

Bone marrow TNF-α mRNA levels were significantly increased, compared with controls, at day 2 but returned to normal levels by day 14. Splenic TNF-α mRNA levels were not significantly different from normal levels at any recovery day postirradiation. Parallel amplifications of GAPDH mRNA were also done during these studies. Bone marrow GAPDH mRNA levels were significantly increased on days 4 and 7 postirradiation. However, no significant differences between control and irradiated splenic GAPDH mRNA levels were detected at any day postirradiation (data not shown).

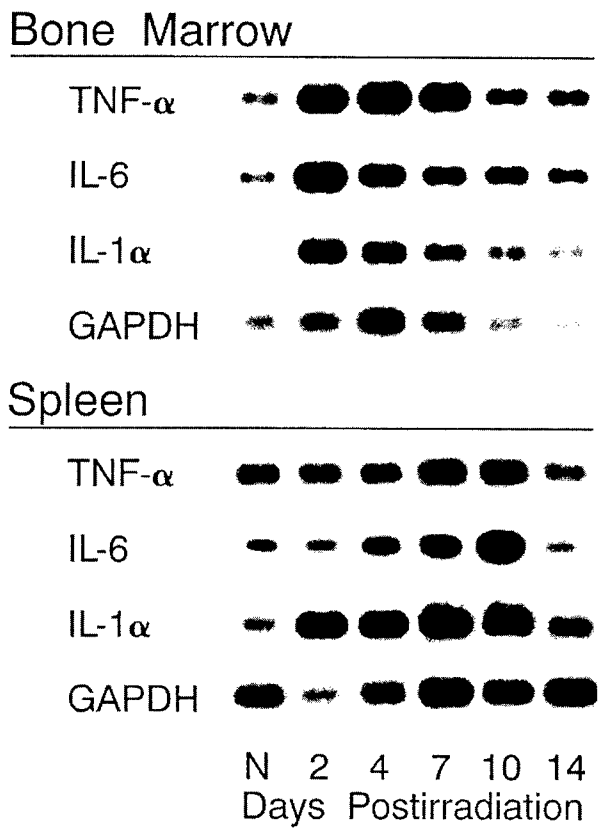

FIG. 1. Representative autoradiographs of RT-PCR-amplified mRNA transcripts of IL-1α, IL-6, TNF-α, and GAPDH in bone marrow and spleen of normal (N) and irradiated mice on days 2, 4, 7, 10, and 14 following a 7.75 Gy ^{60}Co gamma radiation exposure.

Effects of radiation on IL-α, IL-6, and TNF-α protein

Using the Western dot blot technique, IL-1α, IL-6, and TNF-α protein levels in bone marrow and spleen from normal and irradiated mice were determined on days 2, 4, 7, 10, and 14 postexposure. The results are shown in Table 1. IL-1α, IL-6, and TNF-α protein levels in both bone marrow and spleen were not significantly different from controls on any day after irradiation. Serum IL-1α, IL-6, and TNF-α protein levels were also evaluated in normal and irradiated mice on days 2, 4, 8, 10, 14, and 17 postexposure using an ELISA assay. In this assay, IL-1α, IL-6, and TNF-α protein were not detected in the serum (data not shown). The assays had sensitivities of 3.9, 3.9, and 35 pg/ml, respectively.

DISCUSSION

In this study, we investigated the effects of radiation on IL-1α, IL-6, and TNF-α mRNA levels in bone marrow and spleen

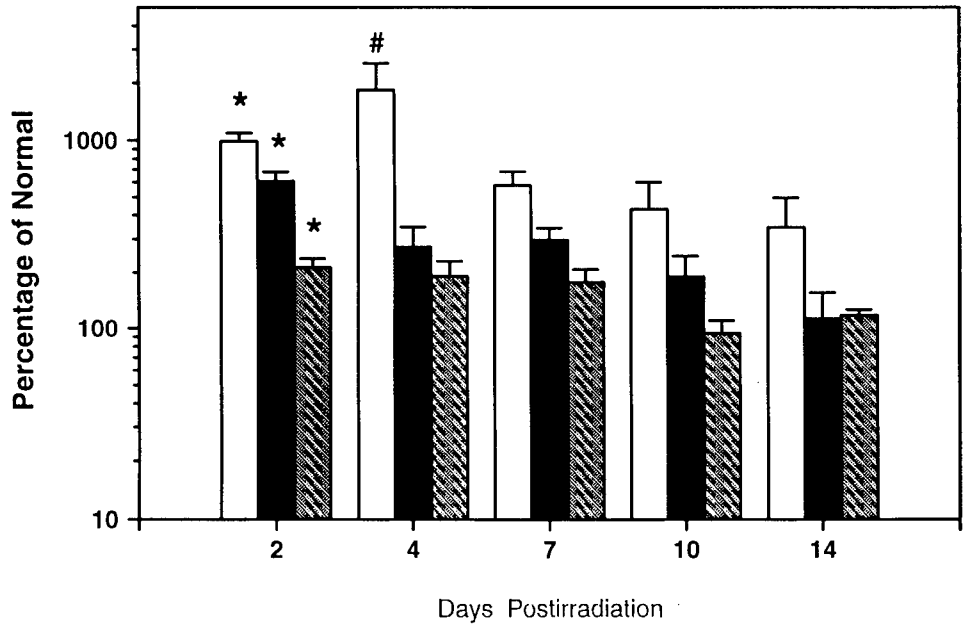

FIG. 2. Relative bone marrow IL-1α (open box), IL-6 (dark box), and TNF-α (striped box) mRNA levels from irradiated mice on days 2, 4, 7, 10, and 14 following a 7.75 Gy ^{60}Co gamma radiation exposure. Data are presented as a percentage of normal control levels and represent the mean ± SEM of values obtained from three experiments. $^{*}p < 0.05$ and $^{\#}p < 0.100$ with respect to normal control values.

by using RT-PCR and Southern blot assays. The traditional techniques for evaluation of gene expression, such as Northern blot and RNase protection assays, could not be used because the total RNA concentrations of the samples were extremely low. In addition, we also measured the protein levels of these cytokines in bone marrow and spleen by Western dot blot analysis and in serum by ELISA assay. Although previous *in vitro* studies have demonstrated that gene expression of some cytokines increases in response to radiation, few studies have been documented *in vivo*.

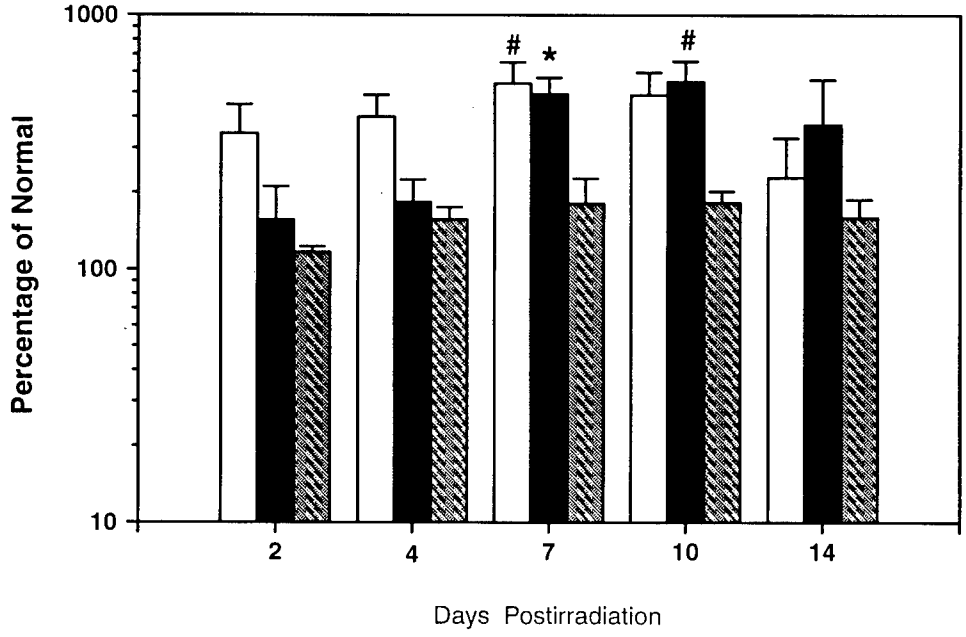

FIG. 3. Relative splenic IL-1α (open box), IL-6 (dark box), and TNF-α (striped box) mRNA levels from irradiated mice on days 2, 4, 7, 10, and 14 following a 7.75 Gy ^{60}Co gamma radiation exposure. Data are presented as a percentage of normal control levels and represent the mean ± SEM of values obtained from three experiments. $^{*}p < 0.05$ and $^{\#}p < 0.100$ with respect to normal control values.

TABLE 1. EFFECTS OF RADIATION EXPOSURE ON MURINE BONE MARROW AND SPLENIC IL-1α, IL-6, AND TNF-α PROTEIN LEVELS[a]

Day post-irradiation	IL-1		IL-6		TNF-α	
	Bone marrow	Spleen	Bone marrow	Spleen	Bone marrow	Spleen
2	99.0 ± 0.4[b]	100.0 ± 0.4	97.6 ± 0.6	101.5 ± 0.6	99.7 ± 0.9	99.4 ± 0.6
4	99.0 ± 0.6	98.7 ± 0.5	98.5 ± 1.3	100.0 ± 1.8	100.4 ± 1.2	100.0 ± 0.8
7	98.6 ± 0.9	98.6 ± 0.6	100.3 ± 2.1	99.3 ± 1.3	102.0 ± 1.1	101.2 ± 0.4
10	98.9 ± 1.3	98.6 ± 0.6	100.5 ± 1.8	98.6 ± 2.5	102.0 ± 0.6	100.7 ± 0.4
14	97.1 ± 1.0	98.9 ± 0.8	99.3 ± 2.8	97.9 ± 3.9	99.6 ± 0.6	101.5 ± 1.0

[a]Results are from densitometric analysis of Western dot blots and are expressed as percentage of control values.
[b]Mean ± SEM of values obtained from three experiments.

When compared with controls, significant increases were observed in the mRNA levels of IL-1α at days 2 and 4, of IL-6 at day 2, and of TNF-α at day 2 in bone marrow and in the mRNA of IL-1α at day 7 and IL-6 at days 7 and 10 in spleen. Similar radiation studies with mouse spleen in our laboratory[20] have shown that splenic IL-1α mRNA levels were increased at 8 h after radiation exposure with 7.75 or 9.75 Gy ^{60}Co gamma radiation. The present study with mouse spleen provided evidence that there was a bimodal expression in IL-1α mRNA levels.

Initially, we had planned to normalize our data to GAPDH mRNA levels. However, we found that GAPDH mRNA levels in the bone marrow were significantly increased at days 4 and 7 postirradiation. On the other hand, splenic GAPDH mRNA levels were not significantly incrased at any day following irradiation. Therefore, to compare mRNA levels at different times postirradiation, we normalized the densitometric scanning data of irradiated mice to the unirradiated controls in each group. In addition, recent work by Weill et al.[23] has shown that peripheral blood lymphocytes as well as an enriched T cell population, irradiated *in vitro* with 4 Gy of ionizing radiation, exhibit an 8-fold increase in GAPDH mRNA 3 h postirradiation. However, this increase was not seen after a 10 Gy exposure. This indicates that the radiation-induced increase in GAPDH mRNA levels can occur both *in vitro* and *in vivo*.

The cytokine protein levels evaluated by Western dot blot or ELISA do not correspond with increased relative mRNA levels detected by RT-PCR and Southern blot assays. The increases in these cytokine mRNA levels are not necessarily reflected by subsequent changes in cytokine protein levels, and the lack of increased IL-1α, IL-6, and TNF-α protein levels may reflect multiple mechanisms of posttranscriptional and posttranslational processes after radiation. Baker et al.[20] have demonstrated that translation of the induced cytokine mRNA occurs at an early recovery stage and that the increases in the levels of splenic IL-1α protein do not reflect the magnitude of the accumulation of mRNA levels. Using human peripheral blood mononuclear cells stimulated with recombinant C5a (rC5a), Schindler et al.[24] have shown that rC5a provides primarily a transcriptional but not a translational signal for IL-1β and TNF. The half-life of the untranslated mRNA is the same as that of the translated message. The mechanisms of posttranscriptional and posttranslational processes remain unclear.

This does not rule out the possibility of a radioprotective effect of these cytokines. Exogenous administration of IL-1, IL-6, and TNF to mice before irradiation has been reported to have a radioprotective function or to further accelerate hematopoietic regeneration following irradiation.[17,25,26] Exogenous administration of cytokines may have indirect effects involving the stimulation of other endogenous cytokines. Studies on cytokine expression following exogenous cytokine therapies will assist in further understanding cytokine mechanisms.

In conclusion, by using RT-PCR and Southern blot assays, we have demonstrated that (1) semiquantitation of mRNA levels of IL-1α, IL-6, and TNF-α in bone marrow and spleen can be accomplished, (2) the differences observed in the mRNA levels of IL-1α and IL-6 can vary in a tissue-specific and time-specific manner, and (3) protein levels of IL-1α, IL-6, and TNF-α in bone marrow, spleen, and serum do not appear to change in concert with mRNA levels.

ACKNOWLEDGMENTS

The authors are grateful to Roxanne Fischer and Ruth Seemann for their technical assistance. This work was supported by the Armed Forces Radiobiology Research Institute under research work unit 96-5. Research was conducted according to the principles enunciated in the *Guide for the Care and Use of Laboratory Animals* prepared by the Institute of Laboratory Animal Resources, National Research Council.

REFERENCES

1. MOCHIZUKI, D.Y., EISEMAN, J.R., CONBON, P.J., LARSEN, A.D., and TUSHINSKI, R.J. (1987). Interleukin 1 regulates hematopoietic activity, a role previously ascribed to hemopoietin 1. Proc. Natl. Acad. Sci. USA **84,** 5267–5271.
2. IKEBUCHI, K., WONG, G.G., CLARK, S.C., IHLE, J.N., HIRAI, Y., and OGAWA, M. (1987). Interleukin 6 enhancement of interleukin 3-dependent proliferation of multipotential hemopoietic progenitors. Proc. Natl. Acad. Sci. USA **84,** 9035–9039.
3. BROXMYER, H.E., WILLIAMS, D.E., LU, L., COOPER, S., ANDERSON, S.L., BEYER, G.S., HOFFMAN, R., and RUBIN, B.Y. (1986). The suppressive influence of human tumor necrosis factors on bone marrow hematopoietic progenitor cells from normal donors and patients with leukemia: synergism of tumor necrosis factor and interferon-gamma. J. Immunol. **136,** 4487–4495.

4. MIZEL, S.B. (1989). The interleukins. FASEB J. **3,** 2379–2388.
5. AKIRA, S., HIRANO, T., TAGA, T., and KISHMOTO, T. (1990). Biology of multifunctional cytokines: IL-6 and related molecules (IL-1 and TNF). FASEB J. **4,** 2860–2867.
6. WRIGHT, R.M., HOLLADAY, C.S., and SPANGELO, B.L. (1993). Lipopolysaccharide induces interleukin-6 release from rat peritoneal macrophages *in vitro:* evidence for a novel mechanism. Circ. Shock **41,** 131–137.
7. BEUTLER, B., KROCHIN, N., MILSARK, I.W., LUEDKE, C., and CERAMI, A. (1986). Control of cachectin (tumor necrosis factor) synthesis: mechanisms of endotoxin resistance. Science **232,** 977–980.
8. WOLOSCHAK, G.E., CHANG-LIU, C.M., JONES, P.S., and JONES, C.A. (1990). Modulation of gene expression in Syrian hamster embryo cells following ionizing radiation. Cancer Res. **50,** 339–344.
9. ANSEL, J.C., LUGER, T.A., LOWRY, D., PERRY, P., ROOP, D.R., and MOUNTZ, J.D. (1988). The expresison and modulation of IL-1 in murine keratinocytes. J. Immunol. **140,** 2274–2278.
10. SCHERMAN, M.L., DATTA, R., HALLAHAN, D.E., WEICHSLBAUM, R.R., and KUFE, D.W. (1991). Regulation of tumor necrosis factor gene expression by ionizing radiation in human myeloid leukemia cells and peripheral blood monocytes. J. Clin. Invest. **87,** 1794–1797.
11. HALLAHAN, D.E., SPRIGGS, D.R., BECKETT, M.A., KUFE, D.W., and WEICHSELBAUM, R.R. (1989). Increased tumor necrosis factor α mRNA after cellular exposure to ionizing radiation. Proc. Natl. Acad. Sci. USA **86,** 10104–10107.
12. LIMANNI, A., BAKER, W.H., CHANG, C.M., SEEMANN, R., WILLIAMS, D.E., and PATCHEN, M.L. (1995). c-kit ligand gene expression in normal and sublethally irradiated mice. Blood **85,** 2377–2384.
13. CHANG, C.M., LIMANNI, A., BAKER, W.H., DOBSON, M.E., KALINICH, J.F., JACKSON, W., and PATCHEN, M.L. (1995). Bone marrow and splenic granulocyte-macrophage colony-stimulating factor and transforming growth factor-β mRNA levels in irradiated mice. Blood **86,** 2130–2136.
14. GALLICCHIO, V.S. (1988). Accelerated recovery of hematopoiesis following sub-lethal whole body irradiation with recombinant murine interleukin-1 (IL-1). J. Leukocyte Biol. **43,** 211–215.
15. PATCHEN, M.L., FISCHER, R., and MACVITTIE, T. (1993). Effects of combined administration of interleukin-6 and granulocyte colony-stimulating factor on recovery from radiation-induced hemopoietic aplasia. Exp. Hematol. **21,** 338–344.
16. SLORDAL, L., MUENCH, M.O., WARREN, D.J., and MOOSE, M.A.S. (1989). Radioprotectin by murine and human tumor-necrosis fcator: dose-dependent effects on hematopoiesis in the mouse. Eur. J. Haematol. **43,** 428–434.
17. NETA, R., PERLSTEIN, R., VOGEL, S.N., LEDNEY, G.D., and ABRAM, J. (1992). Role of interleukin 6 (IL-6) in protection from lethal irradiation and in endocrine responses to IL-1 and tumor necrosis factor. J. Exp. Med. **175,** 689–694.
18. SCHULZ, J., ALMOND, P.R., CUNNINGHAM, J.R., HOLT, J.G., LOEVINGER, R., SUNTHARALINGAM, N., WRIGHT, K.A., NATH, R., and LEMPERT, D. (1983). A protocol for the determination of absorbed dose for high-energy photon and electron beams. Med. Physiol. **10,** 741–771.
19. CHOMCZYNSKI, P., and SACCHI, N. (1987). Single-step method of RNA isolation by acid guanidinium thiocyanate-phenol-chloroform extraction. Anal. Biochem. **162,** 156–159.
20. BAKER, W.H., LIMANNI, A., CHANG, C.M., JACKSON, W.E., and PATCHEN, M.L. (1995). Comparison of IL-1α gene expression and protein levels in the murine spleen following lethal and sublethal total-body irradiation. Radiat. Res. **143,** 320–326.
21. BRADFORD, M. (1976). A rapid and sensitive method for the quantitation of microgram quantities of protein utilizing the principle of protein-dye binding. Anal. Biochem. **42,** 248–254.
22. HAWKES, R., NIDAY, E., and GORDON, J. (1982). A dot-immunobinding assay for monoclonal and other antibodes. Anal. Biochem. **119,** 142–147.
23. WEILL, D., GAY, F., TOVEY, M.G., and CHOUAIB, S. (1996). induction of tumor necrosis factor α expression in human T lymphocytes following ionizing gamma radiation. J. Interferon Cytokine Res. **16,** 395–402.
24. SCHINDLER, R., GELFAND, J.A., and DINARELLO, C.A. (1990). Recombinant C5a stimulates transcription rather than translation of interleukin-1 (IL-1) and tumor necrosis factor: translational signal provided by lipopolysaccharide or IL-1 itself. Blood **76,** 1631–1638.
25. CONSTINE, L.S., HARWELL, S., KENG, P., LEE, F., RUBIN, P., and SIEMANN, D. (1991). Interleukin 1 alpha stimulated hemopoiesis but not tumor cell proliferation and protects mice from lethal total body irradiation. Int. J. Radiat. Oncol. Biol. Phys. **20,** 447–456.
26. KING, A.G., and BADGER, A.M. (1991). Administration of an immunomodulatory azaspirane, SK&F 105685 or human recombinant interleukin 1 stimulates myelopoiesis and enhances survival from lethal irradiation in C57B1/6 mice. Exp. Hematol. **19,** 624–628.

Address reprint requests to:
Dr. Cheng-min Chang
Radiation Medicine Department
Armed Forces Radiobiology Research Institute
8901 Wisconsin Avenue
Bethesda, MD 20889-5603

Received 27 January 1997/Accepted 28 May 1997

EXPERIMENTAL CELL RESEARCH 234, 249–258 (1997)
ARTICLE NO. EX973602

Characterization of Influenza Virus-Induced Death of J774.1 Macrophages

R. Joel Lowy[1] and Dimiter S. Dimitrov

Radiation Pathophysiology and Toxicology Department, Armed Forces Radiobiology Research Institute, Bethesda, Maryland 20889; and Section of Membrane Structure and Function, National Cancer Institute, National Institutes of Health, Bethesda, Maryland 20892

The mechanism and role of influenza virus (IV)-induced pathogenesis of macrophages during respiratory infection are ill defined. Reported here are findings on IV-induced cytopathic effects (CPEs) for an *in vitro* experimental system using the murine macrophage cell line J774.1. CPE was elicited by 0.2 or greater multiplicity of infection (m.o.i.). CPEs showed a lag of 6–8 h postinfection and occurred most rapidly between 6 and 12 h. J774.1 cells did not support productive IV replication, but immunofluorescence demonstrated that IV protein synthesis occurred. Light microscopy and DNA staining showed that after death cells had very condensed cytoplasm and nuclei. Cell remnants were surrounded by intact plasma membrane (PM) as demonstrated by exclusion of a membrane-impermeant dye. Time-lapse video microscopy recordings between 6 and 10 h postinfection showed sequential structural changes, including previously undescribed events. Notable changes were a rapid cytokinesis (zeiosis; "cell boiling"), followed by nuclear shrinkage, and an unusual transient blebbing of the PM. DNA fragmentation occurred after 12 h, producing a wide size range. UV-inactivated virus failed to induce CPEs, and CPE was blocked by amantadine. *N*-Acetylcysteine and pyrrolidine dithiocarbamate, but not other inhibitors of reactive oxygen intermediates, reduced or blocked the CPE. Most changes observed are those attributed to apoptotic processes rather than necrotic cell death. The kinetics and inhibitor effects suggest that IV infection and replication must be initiated to activate CPEs.

INTRODUCTION

Although influenza virus (IV) is one of the most extensively studied viruses and remains an important health problem, its pathogenesis at the cellular level is not completely understood. One important clinical aspect of IV infection is that it predisposes patients for subsequent upper respiratory bacterial infections, causing death in individuals whose immune systems are not robust [1–3]. The specific cellular and molecular mechanisms of this effect are still ill defined [2, 4], but previous work suggests that a contributing factor may be IV lesioning of macrophage function [4–8]. Consistent with this idea are observations in poultry showing that both lymphocytes and macrophages are destroyed during virulent influenza infections [9].

We report here initial findings on a convenient experimental system, using J774.1 cells, a well-characterized murine macrophage cell line, which allows study of cell biological, cell physiological, and immunological aspects of IV–macrophage pathobiology *in vitro*. Descriptions of IV-induced cell death have been reported for MDCK and HeLa cells [10], MDCK cells [11], an avian lymphocytic cell line [11], and human monocytes [12]. Based primarily on DNA fragmentation characteristics, as well as some cell structural and biochemical data, these authors concluded that cell death was occurring by apoptosis. The cell structural changes described here for the effect of IV on J774.1 cells were most similar to an apoptotic-like process and less consistent with necrosis [13, 14]. Time-lapse video microscopy demonstrated, for the first time, that the rapid extensive cytoplasmic fragmentation, the most dramatic and unique characteristic of apoptosis, is induced by IV in these macrophages. Previously undescribed changes for IV-induced pathogenesis include extensive vacuolization prior to this cytokinesis and the observation that the final nuclear and cytoplasmic condensation occurs later in the process. In contrast to previous reports of IV-induced cell death, DNA fragmentation occurs, but does not form "ladders" and is not an early marker of cell death. Also reported are results which show that J774.1 cell death does not occur with UV-inactivated virus or in the presence of the antiviral amantadine. Finally, thiol antioxidants, known to be effective blockers of cell death in other sytems, are shown to be effective against IV in these macrophages as well.

[1] To whom correspondence and reprint requests should be addressed at Radiation Pathophysiology and Toxicology Department, Armed Forces Radiobiology Research Institute, 8901 Wisconsin Avenue, Bethesda, MD 20889-5603. Fax: (301) 295-0313. E-mail: lowy@mx.afrri.usuhs.mil.

0014-4827/97

METHODS

Virus and cell culture. Concentrated stocks of IV strain X31 H3N2 were obtained as purified concentrates at 2 mg viral protein per milliliter (Specific Pathogen-Free Avian Supply, Preston, CT) and stored at −70°C. All plaque assays were performed using MDCK cells as described [15], but cultures were fixed with 4% formaline and stained with crystal violet. Virus titers are expressed as m.o.i. based on MDCK plaque-forming units per J774.1 cell, as J774.1 cells under these conditions did not support productive IV replication (see Results). The J774.1 macrophage cell line was maintained in spinner culture using RPMI 1640 medium supplemented with 10% heat-inactivated fetal bovine serum, 5000 U/ml each of penicillin and streptomycin, and 5 m*M* glutamine. MDCK cells were maintained in DMEM containing the same supplements. J774.1 cells were plated 24 h prior to use. Prior to exposure cells were transferred to a modified Hanks' basic saline glucose (HBSG) solution containing 10 m*M* Hepes and 4 m*M* bicarbonate at pH 7.3 and 5 m*M* glucose [16]. Concentrated virus was added to the cells, which were then incubated for 60 min at 37°C. Cells were then washed twice, returned to culture medium, and maintained for up to 48 h.

Microscopic morphological observation. Cells were plated either on 12-mm coverslips (Bellco Glass, Vineland, NJ) or in microculture chambers with a coverslip bottom (4 cm^2/chamber; No. 178565, Nunc, Napervile, IL) at 1×10^5 cells/cm^2 and exposed to virus. To examine the 24-h morphology cells were stained with 5–10 μg/ml Hoechst 33342 for 10 min and then examined by a digitally enhanced low-light-level fluorescence microscopy system using simultaneous differential interference contrast (DIC) optics and fluorescence [16]. To observe the effects of virus on live cells by DIC optics these same coverslip microculture chambers and exposure conditions were used. At 6 h postinfection cells were switched to HBSG, the HBSG was covered with mineral oil to reduce evaporation, and the chambers were mounted on a thermoelectrically heated custom stage which maintained the temperature at 37°C. DIC images of the same field of cells were recorded directly to video disc and video tape for later time-lapse analysis. Selected frames were photographed on 35-mm Panatonic-X film with a Polaroid freeze-frame system.

Immunofluorescence. Cells were fixed and stained as described by Martin and Helenius [17]. Briefly, cells were fixed in 4% fomaldehyde in neutral buffered PBS for 15 min at room temperature followed by 15 min in 50 m*M* NH_4Cl and permeabilized in 0.1% Triton X. The primary antibodies used for immunostaining were a clinical diagnostic monoclonal influenza A panel which included the H3N2 sera type (Bartel Diagnostic, Issaquah, WA), a commercially prepared polyclonal goat antibody to A/Texas/H3N2 (Virostat, Portland ME), and a X31 polyclonal rabbit antibody which has been previously described [18]. All secondary antibodies used were Fab fragments labeled with FITC and were, respectively, anti-mouse, donkey anti-goat, and donkey anti-rabbit. The secondary antibodies for use with the polyclonals were preabsorbed by the vendor to reduce most forms of cross species nonspecific staining ("min X ML"; Jackson Laboratories Immunological Laboratories, West Grove, PA). Preliminary experiments were performed with the polyclonal antibodies and the best staining levels with low background were obtained with the primary at 1:100 and the secondaries at 1:50. Preliminary experiments performed with noninfected or IV-infected cells stained with only the secondaries showed only nonspecific backgrounds equivalent to unstained cells. The best staining was obtained with the monoclonal and X31-specific polyclonal, which were nearly identical in their staining patterns. Cells were examined using a 100X 1.4 N.A. CF Fluor lens (Nikon, Melville, NY) and the fluorescent images were captured using a cooled camera system (Princeton Instruments, Trenton, NJ) and Metamorph image processing software (Universal Imaging Corp., West Chester, PA) and printed directly from digital image files using a dye-sublimation printer.

Cell viability. Cells were plated in 96-well plates at 1×10^5 cells per well. Twenty-four hours after infection cell survival was measured using a Cell Titer 96 AQueous kit (Promega, Madison, WI). This assay is a version of the commonly used MTT assay, but is based on the water-soluble MTS substrate. Preliminary experiments showed good sensitivity for cell numbers between 10^4 and 10^7 J774.1 cells. Experiments were also done using cells exposed to the vital dye nigrosin [19]. This dye is much easier to read than trypan blue and did not interfere with Hoechst fluorescence. Pharmacological treatments were added at the indicated concentrations to cells as a 2-h pretreatment, during the infection, and during the postinfection period. Due to interference between NAC and PDTC and the MTS reagent a MTT-based assay was used (Promega). Data are expressed as the percentage of unexposed controls without virus or pharmacological agents. Data for no virus but with drug exposure are also presented.

Quantitation of small nuclei formation. The observation that virus-exposed dying cells had much smaller nuclei was used to develop a semiautomatic method of quantification using fluorescence microscopy and image processing techniques (see Results). Cells were plated in 8-well microculture chambers (1 cm^2; No. 177402, Nunc) at 1×10^5 cell/cm^2 and infected at 4 m.o.i. Between 6 and 24 h the chambers were washed with HBS, fixed in 4% formaldehyde, and stained with Hoechst dye. For each treatment fluorescent images were recorded from a total of six regions, three from each of two replicated wells. Semiautomatic morphometric analysis of the nuclear sizes and numbers was performed using Image-1 software from Universal Imaging Corp. Preliminary experiments allowed size thresholds to be set such that nuclei were sorted into two size categories indicative of normal or small condensed nuclei. Preliminary experiments showed that thresholds could be set so that less than 10% of control cells were defined as condensed. For each treatment typically a total of between 100 and 400 nuclei were scored. The data are expressed as percentage small nuclei.

DNA fragmentation. J774.1 cells were plated in T-25 flasks at 2.50×10^6 cells. Exposures or sham infections were performed as described using 2 m.o.i. and harvested for DNA isolation between 0 and 48 h. CEM cells were incubated with an anti-Fas antibody (Q-Fas, UBI, Catalog No. 05-201) at 50 and 200 ng/ml for 24 h for use as a positive control. DNA was isolated using the Gentra Systems, Inc (Minneapolis, MN) kit. All cells were washed with PBS containing Ca^{2+} and Mg^{2+} and then lysed using 0.3 ml of the lysis buffer at room temperature. DNA is reported to be stable up to 1 year under these conditions. RNase A (2 μl, 1 mg/ml) was added and the mixture incubated for 1 h at 37°C. The protein precipitation solution (0.1 ml) was added, and the mixture was vortexed for 20 s and centrifuged for 3 min at 17,000g. The supernatant was poured into a clean 1.5-ml tube containing 0.3 ml 100% isopropanol and mixed. This was centrifuged for 1 min at 17,000g, the supernatant was removed, and the DNA pellet was washed with 70% ethanol. The DNA was hydrated in 0.1 ml TE. Electrophoresis was performed at 4°C with a 1% agarose gel that was stained with ethidium bromide. λ DNA–*Bst*E II digest was used as a marker of the fragment sizes. The samples were loaded on a 1.5% agarose gel and electrophoresed in 0.5% TBE buffer for 1 h at 5 V/cm. The DNA was stained with ethidium bromide and pictures were taken with a Polaroid camera.

RESULTS

Effect of virus titer on J774.1 survival. Figure 1 shows the effect of IV titer on J774.1 cell survival. Decreases in the number of cells occurred between 0.2 and 20 m.o.i. by 24 h. Virus stocks were UV exposed, a common method to inactive influenza, and its effects were confirmed by loss of plaque formation on MDCK

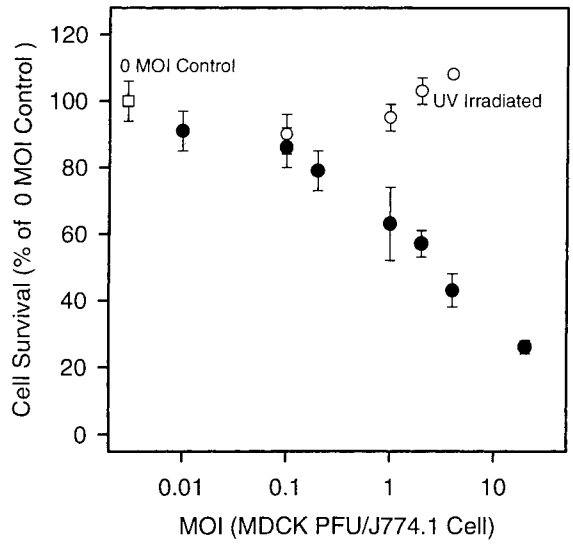

FIG. 1. Virus titer effect on cell number following IV exposure. Cells (1×10^5/well) in 96-well plates were exposed to varying titers of IV [note log scale and m.o.i. (multiplicity of infection) expressed as MDCK cell plaque-forming units per J774.1 cell. After 24 h cell survival was determined using the colorimetric MTS assay. Data are for cells exposed to live IV (solid circles), UV-inactivated IV (open circles) and mock exposed IV (open square). CPEs occur at titers above 0.2 m.o.i. for live IV. No CPE is observed for UV-treated IV. Data are expressed as means ± SEM for nine replicate cultures from three independent experiments. Data were calculated as percentage of paired mock-infected controls.

cells (data not shown). Inactivated virus failed to produce a CPE. This suggests that the macrophage response was not due to either a nonspecific effect, such as membrane damage by inactive virus particles, or cell signaling by influenza binding to macrophage surface receptors. Macrophages and monocytes have not been shown to support IV replication by most investigators, although production of low levels has been observed under some specialized culture conditions [4, 20, 21]. This was also true of the J774.1 cells. J774.1 cells in T-25 flasks were infected with 2 m.o.i. and showed the expected changes in morphology described below. Plaque assays conducted on MDCK cells using the medium from these J774.1 cells gave a PFU/ml of 2, approximately an 8 log reduction in titer from the viral stocks used to expose the J774.1 cells to virus. CPE assays were conducted at extended times up to 5 days postinfection (data not shown). At no m.o.i. was an increased CPE observed at later times. At intermediate m.o.i. after 48 h cell numbers began to return to initial levels due to replication of the surviving cells.

Immunofluorescence. Although permissive IV replication did not occur, the synthesis of IV proteins was supported by the J774.1 cells. Figure 2 shows light micrographs of J774.1 cells exposed to 4 m.o.i. and fixed at 6 h. This fixation time was chosen as being prior to loss of cells and cell structure during cell death, but at a time when influenza protein expression has been shown to reach a maximum in IV permissive cell lines. Cells exposed to virus show typical staining for IV, including both the nucleus and the cytoplasm (Figs. 2A and 2E). Only very low levels of combined autofluorescence and nonspecific immunostaining were observed for any of the 0 m.o.i. controls and are visible in part due to the sensitivity of the cooled CCD camera system (Figs. 2C and 2F). In two experiments a total of 200–400 cells were scored for each m.o.i. and the percentage

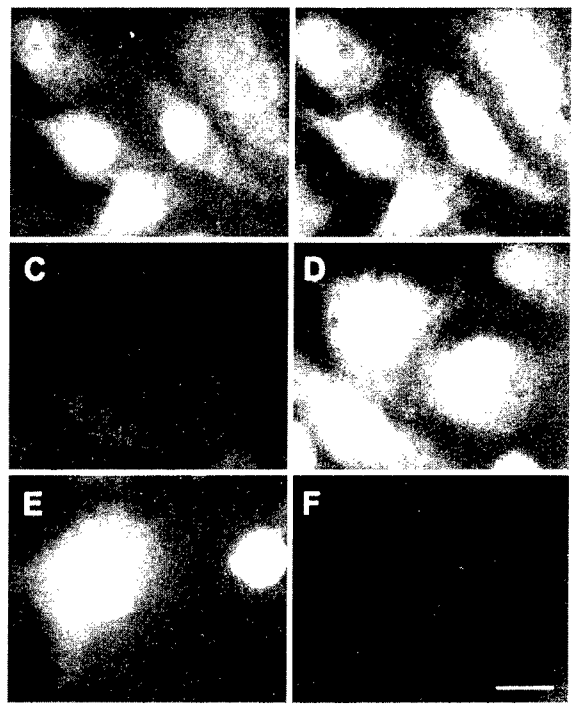

FIG. 2. Immunofluorescence staining of IV-exposed J774.1 cells. Cells were infected with 4 or 0 m.o.i., fixed, and stained as described at 6 h postinfection. The primary antibody was either a IV monoclonal panel of multiple sera types or a polyclonal to X31 followed by the appropriate FITC-labeled secondary antibody (see Methods). (A) 4 m.o.i. with monoclonal panel; (C) 0 m.o.i. with monoclonal panel. B and D are Evans blue counterstained red fluorescence to show cell locations for A and C, respectively. (E) 4 m.o.i. X31 polyclonal. (F) 0 m.o.i. X31 polyclonal. Cells infected with 4 m.o.i. show nuclear and cytoplasmic staining with the same pattern for both types of primary antibodies. Interestingly the cytoplasmic staining forms a fine net-like reticular structure in the J774.1 cells. Only low levels of autofluorescence/nonspecific staining occurred for the 0 m.o.i. controls, which is visible due to the high sensitivity of the low-light-level camera system. Fluorescent images in A, C, E, and F were acquired with FITC filters, and B and D were obtained with Texas red filters. No "cross-talk" between the filter sets was observed. All images were captured using a cooled CCD and image processing software (see Methods). Equivalent settings were used for the 4 and 0 m.o.i. treatments with each antibody so that intensities displayed are directly comparable. The polyclonal antibody resulted in slightly brighter staining, but all images were easily captured by the low-light-level camera system. Bar, 20 μm.

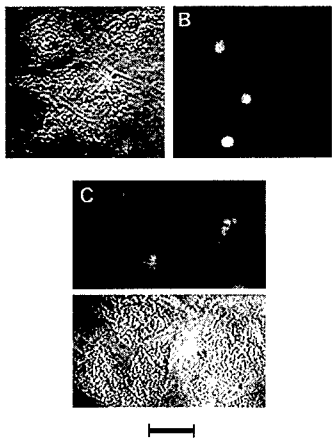

FIG. 3. Light microscopy appearance of IV-exposed and control cells. J774 cells were infected with 4 m.o.i. (A and B) or mock-infected (C and D) and fixed at 24 h. Cells were exposed to the membrane-impermeant dye nigrosin prior to fixation and to the DNA stain Hoechst 33323 afterward. Cells were examined by DIC (A and D) or fluorescence microscopy (B and C). IV-exposed cells have much smaller diameter nuclei which stain much more intensely and lose the heterogeneous staining pattern seen in the controls. The IV-exposed cells have distorted morphologies relative to those of controls and much more compact cytoplasm. In some cases the organelles are condensed to one side of the cell away from the plasma membrane. Despite these structural changes, IV-exposed cells, like control cells, do not have intense blue-black nuclear staining and therefore excluded the nigrosin dye. Bar, 5 μm.

of positive stained cells was determined. For input exposures of 0.1, 2, and 4 m.o.i. the respective percentages were 2, 56, and 88%. These data correlated well with the CPE values in Fig. 1.

Morphological changes. Morphological examination of cells postvirus exposure at 24 h (Figs. 3A and 3B) showed that the cells were very altered from the controls (Figs. 3C and 3D). They appeared smaller, but not detached or rounded, and had less cytoplasm. DIC microscopy showed the nuclei to be smaller and darker than normal. DNA staining with Hoechst dye (Figs. 3B and 3C) confirmed that the average nuclear size was reduced in diameter compared to the controls. DNA staining of normal J774.1 cells typically showed some chromatin structure (Fig. 3C) which is lost in virus-exposed cells. The staining intensity for these smaller nuclei was much greater than that of the controls by a factor of 200- to 300-fold. This difference is based on gain settings for the intensified camera system necessary to obtain images of a comparable gray-scale value which could be accurately recorded by the imaging system. Therefore despite being displayed at apparently similar intensities, the images were actually 2 logs different in intensity. It is unlikely that nuclear volume or thickness changes could readily account for this large change in DNA staining intensity; therefore an alteration in DNA condensation was the likely cause.

An important feature of differing forms of cell death is plasma membrane integrity. During necrosis there is cell swelling and rupture, leading to failure of the plasma membrane and extensive staining by dyes such as Trypan blue, nigrosin, and propidium iodide. In apoptotic processes these events do not occur or occur much later during a secondary phase of necrosis [14]. These differences in membrane permeablity have been used as the basis for flow cytometry assays of apoptotic cell death [22, 23]. The cells shown in Fig. 3 were exposed to nigrosin prior to fixation and Hoechst staining. Few floating cells were observed and care was taken to not lose cells from the substrate during dyeing, washing, and fixation. Although the nuclei appear darker in DIC due to their condensation, the intense blue-black staining expected for necrotic cells is not present. Figure 4 shows low-magnification light micrographs of cells exposed to virus at 4 (A) or 2 m.o.i. (B), or unexposed and permeabilized (C) with Triton X prior to staining with nigrosin and fixation. Only the Triton-X-treated cells show extensive staining. Even at 4 m.o.i., with extensive cell death and loss, as expected from the CPE measurement (Fig. 1), only a few of the remaining cells were stained.

Figure 5 shows that the kinetics of the formation of small nuclei (A) and CPE (B) up to 24 h postinfection had a very similar pattern. For both of these parameters the greatest change occurred after 6 h postinfection and by 12 h. A small increase in CPE (10–15%) by the MTS assay was measured prior to 8 h but was not likely to have been biologically significant (cf. standard error bars for 0 m.o.i. in Fig. 1). There was an additional increase in the number of cells showing small nuclei formation between 10 and 24 h, and a small additional decrease in cell viability measured between 12 and 24 h, but both of these changes were at a much slower rate. Interestingly these changes occur with a considerable lag, corresponding well to the 3- to 6-h lag in expression of IV proteins, but after 6 h the pathogenesis proceeds rapidly. Also, based on the 8-h time points, it appears the morphological changes slightly precede the metabolic marker. In contrast there was essentially no change for mock-infected cells. These kinetic data, as well as the titer data in Fig. 1, were generally consistent with those reported for a different strain of IV in human monocytes and a different macrophage cell line [24].

DNA fragmentation following viral exposure. The structural changes described above were indicative of cell death via an apoptotic mechanism (see Discussion). DNA fragmentation has been shown to occur in many cells undergoing apoptosis and is an important biochemical marker in most, but not all, cells [25, 26]. Figure 6 shows gels of DNA extracted from J774.1 cells mock infected (lanes 1–6) and infected at 2 m.o.i. (lanes

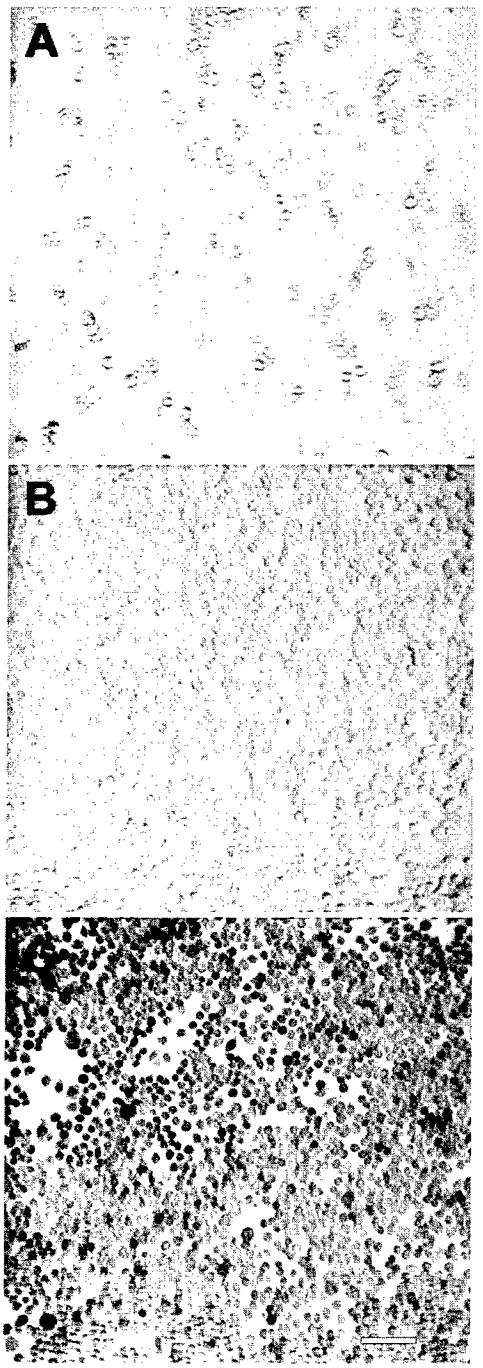

FIG. 4. Low-magnification light micrograph of nigrosin-exposed cells. Cells were infected with 4 m.o.i. (A), 2 m.o.i. (B), or mock-infected (C). At 24 h postinfection cells were exposed to nigrosin in PBS and fixed. Cells in C were permeabilized with 0.1% Triton X in PBS prior to nigrosin exposure. Low magnification allows the response to nigrosin of a large number of cells to be seen. All the permeabilized cells show typical blue-black staining, indicating plasma membrane permeability. In contrast few virus-exposed cells are positive at either m.o.i. Under these same conditions, measurements of cell survival (Fig. 1) indicated that at least 50% of the cells are dead. At 4 m.o.i. some nuclei have a darkened appearance and a loss of cells is evident. A few of these cells are positively stained, but most are condensed structures which appear slightly darker, as can be observed more clearly at higher magnification (Fig. 3). Bar, 100 μm.

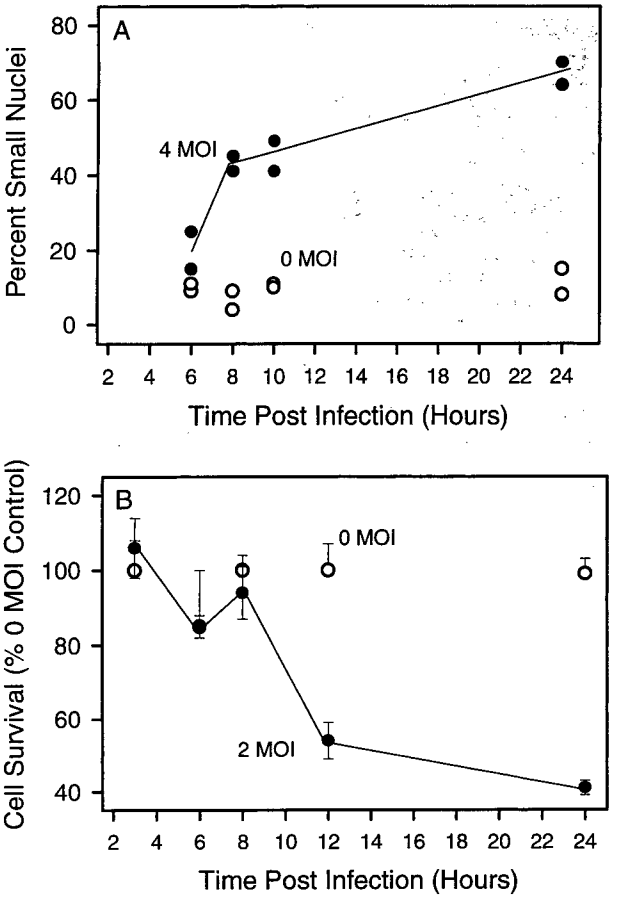

FIG. 5. Kinetics of CPE and small nuclei formation. In A cells were exposed to 4 m.o.i. in multiwell slide chambers. At 6, 8, 10, and 24 h postinfection cultures were fixed and the nuclei stained with Hoechst dye. Representative fields were examined using fluorescence video microscopy, and digital recording and a semiautomatic image processing algorithm were used to count and classify nuclei as either normal or condensed (see Methods) for exposed (closed circles) or mock-infected controls (open circles). The mean percentage of small nuclei is presented from two independent experiments. Few condensed nuclei were observed prior to 6 h postinfection but a rapid increase occurred by 8 h postinfection, which continued at a slower rate up to 24 h. No change in nuclear size was measured for mock-infected controls. In B cells were plated in 96-well plates and exposed to 0 or 2 m.o.i. and assayed for cell survival at the indicated times. Note change in abscissa from top panel. The pattern was similar to the formation of small nuclei. There was an initial lag of several hours prior to the greatest loss of cell viability between 8 and 12 h, with an additional but much smaller loss by 24 h. The decrease observed at 6 h postinfection was likely not to be biologically significant as a similar decrease was seen in the time-matched mock-infected cultures, and the cell survival value is within the variability seen for mock-infected cells (see Fig. 1). Data are means ± SEM for six cultures.

7–11) and harvested at 6–48 h. No DNA fragmentation was seen for the mock-infected cells or for the infected cells prior to 24 h. Fragmentation of the DNA was observed at 24 and 48 h, but cleavage created a broad range of sizes, not small base pair units. It is important

FIG. 6. Fragmentation of DNA. J774.1 cells were cultured in T-25 flasks and infected with 2 m.o.i. or mock-infected. At 0, 6, 8,12, 24, and 48 h postinfection medium was removed, and cells were gently washed once in PBS and treated with a cell-lysis DNA extraction buffer (see Methods). Lane 1 is 0 h mock-infected. Lanes 2–6 are mock-infected cells, and lanes 6–11 are IV-infected cells at 6, 8, 12, 24, and 48 h postinfection. Lanes 0 and 12 are molecular weight markers (λ DNA–*Bst*EII digest) of visible length between 224 and 8454. Only in the infected cells at 24 and 48 h was DNA fragmentation observed and without laddering characteristic of intranucleosomal fragmentation. Lanes a–b are DNA CEM cells exposed to anti-Fas antibody, which is known to induce apoptosis. Lanes are (a) molecular weight marker, (b) 200 ng/ml antibody, (c) 50 ng/ml antibody, and (d) untreated control. DNA laddering is seen in b and c.

to note that this DNA cleavage was not seen during the period of 6–12 h when the other markers for cell death are clearly evident.

As intranucleosomal cleavage yielding typical DNA ladders was not seen, these results were investigated further. Several alternate protocols for isolating DNA combined with different gel types and several DNA staining methods were used for analysis. These included extraction methods which removed most nonfragmented material and polyacrylamide gels stained with the very sensitive sybr green nucleic acid gel stain. All the results were similar to one another (data not shown). As a positive control the cell line CEM was exposed to an agent known to produce apoptosis, Anti-Fas antibody (Fig. 6, bottom, lanes a–d). The DNA from these cells was processed by the same methods used for the IV-exposed J774.1 cells. The CEM DNA, as expected, produced the characteristic small oligonucleotide laddering pattern generally associated with apoptosis.

In addition two different forms of *in situ* DNA nicked end labeling, e.g., "TUNEL" assays, from two differing manufacturers were used in an attempt to demonstrate intranucleosomal cleavage. In one case samples were submitted to the manufacturer for optimization of their protocol. In most case no labeling was seen at any viral titer level. In only one set of samples, 2 m.o.i. after 24 h, was any positive staining observed, but it was in less than 5% of the total cells.

Time-lapse observation of IV-induced cytopathic effect. Morphological criteria remain the most consistent markers for describing cell death processes and distinguishing between processes which are either primarily necrotic or apoptotic [27, 28]. Therefore it was important to describe morphological markers in more detail to better characterize the CPE in this experimental system. Of particular interest was whether the dramatic cytokinesis occurred (zeiosis, cell boiling), resulting in rapid cell fragmentation, which is considered an important and distinguishing characteristic of apoptotic processes [13, 14, 28]. Also, the well-defined limited time period IV induction of CPEs in the J774.1 cells combined with the availability of the imaging equipment provided an opportunity to obtain a more detailed continuous examination at the light microscopy level of virally induced cell death in a macrophage than has been previously reported to the best of our knowledge. Figure 7 shows single video frames, during the period of greatst change, for a cell that was observed continuously from 6 to 10 h postinfection at 4 m.o.i. The cell shown was taken from a larger field and is representative of changes observed for most of the other cells. An advantage of DIC optics, which uses heat-filtered white light, was that, unlike fluorescence measurements, these conditions were not damaging to the cells. Mitosis, a process sensitive to damaging conditions during microscopy, fortuitously occurred in one cell in the field (not shown) during the observation period. The displayed times are relative to the start of the recording, which was 6 h postinfection. The video frames selected are not evenly spaced so that the periods of greatest morphological change can be presented as a summary figure. The morphological changes included both changes previously described and new features not reported in earlier detailed descriptions of cell death processes, including those for virally induced CPEs [29–33].

The cells normally displayed small translational movements, accompanied by frequent retraction and extension of thin pseudopods (filopodia). The first morphological change was a flattening of the cell and loss of cytoplasmic extensions. The next change, which has not been previously described, was formation of large lucent vesicles in the cytoplasm and within the nuclear region. Many of these vesicles appeared to be apposed to both the inner and the outer surfaces of the nuclear membrane. There were very rapid changes in both the position and the size of these vesicles. In some cells this process stopped, the cells partially returned to a more rounded appearance, and cytoplasmic extensions reappeared. These cells then reflattened and repeated the lucent vesicle

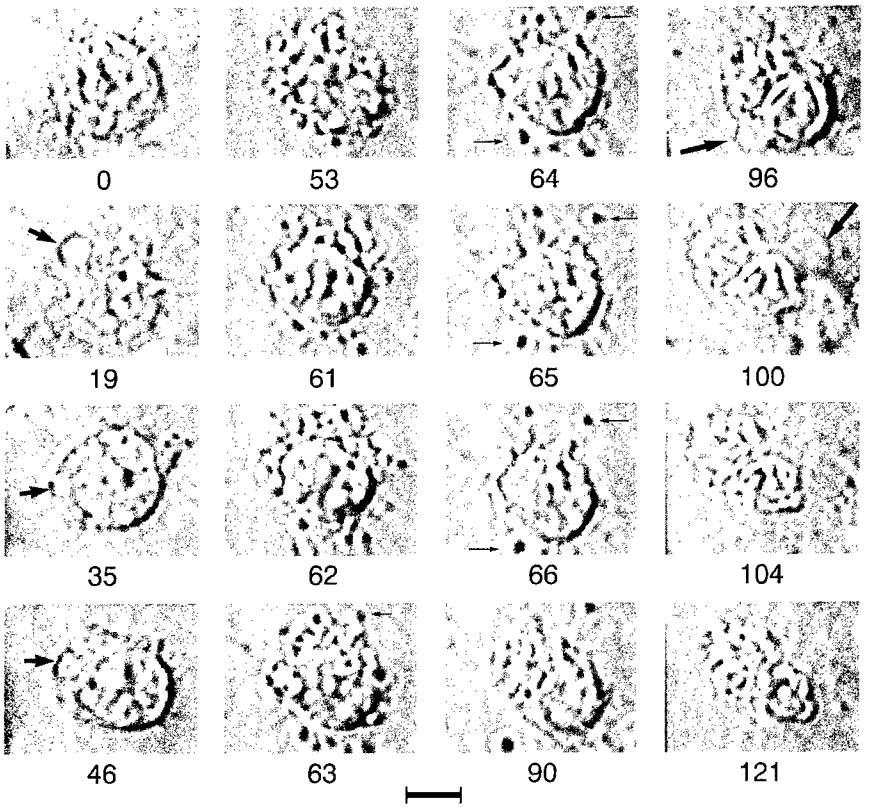

FIG. 7. DIC images from time-lapse video microscopy. J774.1 cells were exposed to 4 m.o.i. At 6 h postinfection exposed cells were mounted on the microscope in a temperature-regulated chamber at 37°C. DIC images were recorded continuously at low light levels using heat-filtered white light between 6 and 10 h postinfection. Images for a single cell, illustrating typical morphological changes, are shown. Times points shown, labeled on each panel, were selected for periods of greatest change and are relative to 6 h postinfection which is equal to record time 0. Times 0 to 35 min illustrate the initial cell flattening, loss of filopodia, and rapid formation of large lucent cytoplasmic vesicles (arrowhead). Times 61 to 66 min show the cytoplasmic boiling or zeiosis and release of small vesicles or organelles (arrows). Times 96 to 121 min show the formation and subsequent retraction of membrane blebs (arrows) and the final cytoplasmic and nuclear shrinkage, terminating in an apoptotic body. Bar, 5 μm.

formation sequence. Further observation is needed to resolve whether these are changes in the nuclear membrane, apposition of intracellular compartments, or the formation of macropinosomes [34] from the cell surface. If internal, these vesicles may be a feature of regulated J774.1 cell death. There is a single report showing electron micrographs of what may be similar lucent vesicles during cell death induction by a very different agent, cytotoxic lymphocytes [35].

In the next stage for all cells the cytoplasm took on a very granular appearance, with the formation of small phase-bright and phase-dark structures, which also displayed rapid movements. In some cells these could be seen as small vesicles that rapidly budded off from the cell surface. This rapid cytokinesis (zeiosis) was well described as a boiling appearance in previous reports (see Discussion). Upon the appearance of these small rapidly moving vesicles, the cytoplasmic region, but not the nuclear region, appeared to decrease in area. Next, as the small vesicle formation and budding decreased in frequency, the cytoplasmic area appeared to become larger in proportion while the nucleus began to decrease in size. In some cells the cytoplasmic area did not seem to expand much but became a larger portion of the cell profile due to the decrease in the nucleus. During the period that the nuclear profile continued to decrease, one or more large expansions, or blebs, of the plasma membrane generally occurred. These previously undescribed blebs were composed of very clear membrane-bound cytoplasm and appeared to contain no organelles. These plasma membrane blebs did not rupture but shrank until they either disappeared or formed a small organelle-free region to one side of the cell. A possible cause may be loss of cytoskeletal anchor elements at localized sites and/or transient loss of ion and water homeostasis. As the membrane swelling was not permanent, the cells must generally regain volume regulation and ion–water homeostasis. During this period there appeared to be additional shrinkage of both the nucleus and the cytoplasm-containing organelles.

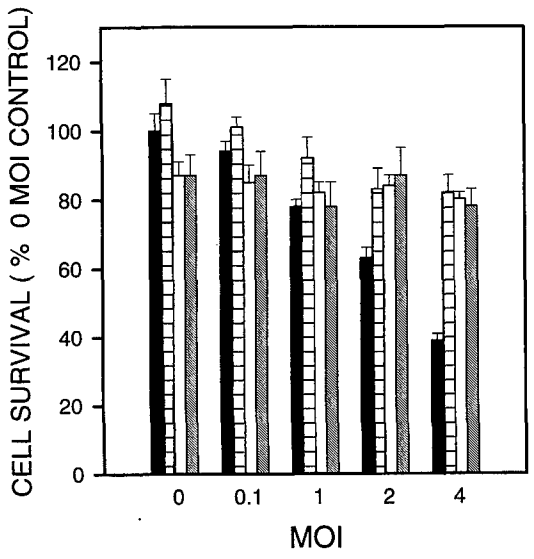

FIG. 8. Effect of amantadine on IV-induced CPE. J774.1 cells were infected with the indicated titers of virus or mock-infected. Amantadine was added to both mock-infected and infected cells as a 2-h pretreatment, during the infection, and during the 24-h postinfection culture period. Amantadine concentrations were 0 μg/ml (solid bars), 5 μg/ml (horizontally striped bars), 15 μg/ml (open), and 25 μg/ml (cross hatched). At 1, 2, and 4 m.o.i. all concentrations of amantadine reduced the CPE to control levels. Amantadine did show a small CPE at 15 and 25 μg/ml. Data are means ± SEM for six cultures from two independent experiments.

Both the membrane swelling and the cytoplasmic contraction are consistent with the possibility of a large transient calcium influx. Once the membrane bleb decreased, no further changes were evident. The final cell appearance was identical to that of the small cell remnants, apoptotic bodies, observed in the other cytopathic experiments (Fig. 3).

Effects of amantadine on CPE. The results with UV-inactivated virus suggested that the CPEs of the J774.1 cells required infection by IV, not merely surface binding. The effects of amantadine on IV have been extensively studied and the blockage for most IV strains occurs during entry via the endocytic pathway with even the earliest IV replication events being inhibited. For details and review of the molecular basis of amantadine's effects see Ref. [36]. Figure 8 shows that, as expected, 5 μg/ml blocked CPEs in the J774.1 cells. Higher concentrations did not reduce the virally induced CPEs further, but were slightly cytopathic to the controls. Amantadine added between 1 and 6 h postinfection, as expected for the X31 IV strain, did not block CPEs (data not shown).

Effect of antioxidants. Antioxidants have been shown to block apoptosis, including virus-induced CPE in a wide number of experimental systems, including influenza virus *in vivo* [37]. Among the mechanisms for ROIs activating cell death, in both viral and nonviral systems, that have been suggested are nonspecific cellular damage, cell signaling agents that activate transactivation factors [38], and most recently mitochondrial proteins that activate proteases associated with apoptosis [39]. Figure 9 shows the effect of several different types of ROI inhibitors. Only the thiol agents NAC and PDTC were effective in blocking the IV-induced CPEs, while the other antioxidants, desferoximine nesyiate, a metal chelator, trolox, a peroxidation inhibitor, and catalase, a hydrogen peroxide inhibitor, were ineffective.

DISCUSSION

These studies describe several important observations concerning IV-induced death of J774.1 macrophages. Data are presented on the virus titers needed for CPE and kinetics of this particular experimental system. The data for UV-treated virus, CPE kinetics, and amantadine all support the idea that infection and IV replication are necessary to activate CPE. CPE does not appear to be due to either cell surface-mediated signaling events or nonspecific cell membrane damage. These results confirm and extend the observation that cyclohexamide blocked IV-induced apoptosis in MDCK cells [10].

Determining the likely mechanism of virally induced

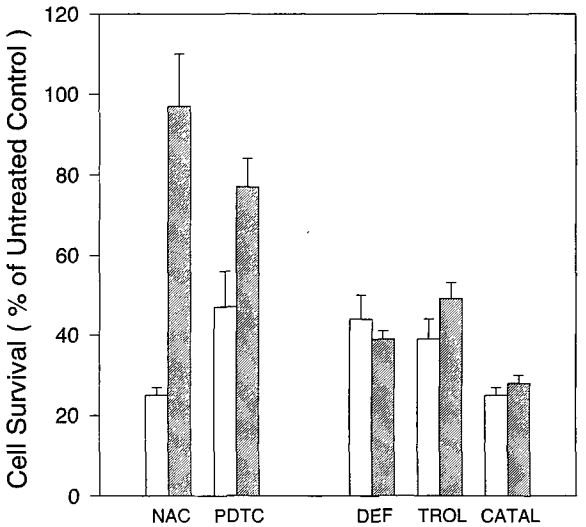

FIG. 9. Effect of antioxidants on IV-induced CPE. J774.1 cells were infected with 4 m.o.i. in the absence (white bars) or in the presence of various agents (shaded bars) and the cell survival was assayed. Inhibitors were *N*-acetylcysteine (NAC, 50 m*M*), pyrrolidine dithiocarbamate (PDTC, 100 m*M*), deferoximine nesyiate (DEF, 0.5 m*M*), trolox (TROL, 1.0 m*M*), and catalase (5000 U/ml). Only the two thiol antioxidants were effective in blocking the IV-induced CPE. Data are means ± SEM for six cultures from two independent experiments performed for each drug. Data are normalized to untreated mock-infected cultures performed as controls with each drug (values not shown).

cell death is of considerable interest for many virus–host cell interactions, with apoptosis often being favored over necrosis [40]. Morphological characteristics of the apoptotic process include nuclear, cytoplasmic, and plasma membrane shrinkage, chromatin condensation, lack of plasma membrane rupture, and cytokinesis by rapid blebbing (zeiosis). Necrotic processes differ by producing cytoplasmic swelling, cell rupture, and failure of the plasma membrane, but no change in nuclear morphology and no cytokinesis. DNA fragmentation occurs in most but not all apoptotic systems, and there are increasing reports that classic laddering is not always observed. Intranucleosomal cleavage associated with apoptosis can result in formation of small fragments, larger oligomers, or both [25, 26, 41]. Recent methodological reviews caution that morphological changes are still the best criterion for distinguishing apoptosis from necrosis [27, 28]. Despite the importance of IV pathogenesis, there are few studies relative to other viral types [40]. Two studies reported apoptosis in MDCK cells, an epithelial cell line which supports IV replication [10, 11]. In one of these reports apoptosis was also observed in RP9 cells, an avian lymphocyte line [11]. To date there has been only one brief report demonstrating that IV causes apoptosis in cells of the macrophage/monocyte lineage [12] based on morphology and DNA fragmentation. It was expected that CPE in J774.1 cells would show similar characteristics, consistent with apoptotic cell death. The morphological observations for J774.1 cells correspond well to both brief descriptions of apoptotic structural changes for IV-induced apoptosis and the more detailed descriptions from other experimental systems [13, 14, 26]. This conclusion is based on direct comparisons between images of the J774.1 cell structural changes and final cell remnant morphologies with descriptions and pictures of apoptotic processes in previous reports [29, 31–33]. Importantly the J774.1 cells underwent both nuclear and cytoplasmic shrinkage and the latter occurred by the characteristic dramatic vesicularization and budding of the cytoplasm, i.e., zeiosis or cell boiling (Fig. 7) [29, 31–33]. The nuclear changes occurred after cytokinesis. Typical necrotic markers, such as cell rupture or maintenance of intact nuclear morphology, were not observed. There was no loss of J774.1 membrane integrity (Figs. 3 and 4), which contrasted the descriptions of IV-induced CPEs in human monocytes [42]. However, the DNA cleavage pattern seen in this study was not that typically expected of apoptotic systems. The cleavage which did occur was not kinetically well coordinated with the other cytopathic changes, suggesting that it was a later secondary process. This lack of typical laddering was surprising, as bacterial toxins have been shown to induce laddering in J774.1 cells, although their appearance is not as sharply defined as those reported for lymphoid cells [43, 44]. However, several reports of apoptosis in macrophages also failed to observe typical DNA laddering [45], including J774.1 cells [46]. The reasons for differences in this or any other system, particularly relative to the clear laddering generally observed in T-cells, are still obscure [25]. Currently the only alternatives for classification of cell death are as necrotic or apoptotic. All of the observations made in this study, except for DNA fragmentation, are consistent with apoptosis and not with necrosis. Therefore it seems likely that IV induces a regulated form of cell death in the J774.1 cells as well, which is best described as an apoptotic-like process. Finally, the order of these structural changes may be important in understanding underlying biochemical events. In this system it is clear that nuclear condensation is a late and terminal event and is preceded by cytokinesis. The causal relationship between nuclear changes and the other events during CPE, such as zeiosis, bears further investigation.

The mechanism of IV-induced cell death, as for all viruses to date, is still not completely defined. Broadly possibilities include (a) nonspecific cell damage, such as changes in membrane permeability; (b) relatively nonspecific biochemical mechanisms due to a general down-regulation of host protein synthesis; (c) specific IV interference with regulators of cell death; and (d) autocrine effects of either ROI or cytokines. Each of these possibilities warrants investigation. However, if relatively nonspecific mechanisms, such as protein synthesis inhibition, dominate, it is surprising that antioxidants were effective in blocking cell death. Furthermore the result that only the thiol antioxidants were effective suggests that specific IV–cell interactions are occurring and can be manipulated. If ROIs were acting only as cell damaging agents, then the other antioxidants should have blocked the CPE. A suggestion for IV–host cell signaling pathways leading to apoptosis has been made based on transfection and expression of IV HA, leading to activation of NF-κ B [47]. It was postulated that this could be the mechanism for IV-induced apoptosis and that modulation with antioxidants which block NF-κB should be effective in blocking apoptosis. However, their results and those presented here are in contrast to results obtained with MDCK cells in which antioxidants failed to block the CPE [48]. Also further investigation of an autocrine role for cytokines is warranted. IV has been shown to elicit TNF-α, IL1-β, and IL-6 [20, 24, 49]. J774.1 cells, like other macrophage/monocyte cells, produce or respond to a variety of immunomodulators [46, 50–53], including secretion of TNF-α [54], an important immune system inducer of cell death.

In conclusion, J774.1 cells are readily maintained in culture, easily obtained in large numbers, and have many characteristics of *in vivo* macrophages, including the ability to produce various immunomodulators. Therefore, the IV–J774.1 cell system described here is likely to provide an additional valuable experimental system for studying IV–macrophage interactions including cell death and aid in our understanding of IV-induced pathogenesis.

The collegiality, help, and useful discussions of Drs. Robert Blumenthal, Anu Puri, Charles Pak, and Gary Whittaker are gratefully acknowledged. The gift of the X31 polyclonal antibody from Dr. Ari Helenius is also gratefully acknowledged. Support was through NIAID Grant AI 35892 to R.J.L.

REFERENCES

1. Abramson, J. S., and Mills, E. L. (1988) *Rev. Infect. Dis.* **10,** 326–341.
2. Murphy, B. R., and Webster, R. G. (1990) *in* Virology (Fields, B. N., and Knipe, D. M., Eds.), 2nd ed., pp. 1091–1152, Raven Press, New York.
3. White, D. O., and Fenner, F. J. (Eds.) (1994) Medical Virology, 4th ed., pp. 1–603, Academic Press, New York.
4. Sweet, C., and Smith, H. (1980) *Microbiol. Rev.* **44,** 303–330.
5. Astry, C. L., and Jakab, G. J. (1984) *J. Virol.* **50,** 287–292.
6. Laegreid, W. W., Liggitt, H. D., Silflow, R. M., Evermann, J. R., Taylor, S. M., and Leid, R. W. (1989) *J. Leukocyte Biol.* **45,** 293–300.
7. Morgensen, S. (1979) *Microbiol. Rev* **43,** 1–26.
8. Rouse, B. T., and Horohov, D. W. (1986) *Rev. Infect. Dis.* **8,** 850–873.
9. Van Campen, H., Easterday, B. C., and Hinshaw, V. S. (1989) *J. Gen. Virol.* **70,** 2887–2895.
10. Takizawa, T., Matsukawa, S., Higuchi, Y., Nakamuara, S., Nakanishi, Y., and Fukuda, R. (1993) *J. Gen. Virol.* **74,** 2347–2355.
11. Hinshaw, V. S., Olsen, C. W., Dybdahl-Sissoko, N., and Evans, D. (1994) *J. Virol.* **68,** 3667–3673.
12. Fesq, H., Bacher, M., Nain, M., and Gemsa, D. (1994) *Immunobiology* **190,** 175–182.
13. Duvall, E., and Wyllie, A. H. (1986) *Immunol. Today* **7,** 115–119.
14. Wyllie, A. H., Kerr, J. F. R., and Currie, A. R. (1980) *Int. Rev. Cytol.* **68,** 251–306.
15. Patterson, R. G., and Lamb, R. A. (1993) *in* Molecular Virology A Practical Approach (Davison, A. J., and Elliott, R. M., Eds.), 1st ed., pp. 35–72, IRL Press, New York.
16. Lowy, R. J., Sarkar, D. P., Whitnall, M. H., and Blumenthal, R. (1995) *Exp. Cell Res.* **216,** 411–421.
17. Martin, K., and Helenius, A. (1991) *Cell* **67,** 117–130.
18. Braakman, I., Hoover-Lity, H., Wagner, K. R., and Helenius, A. (1992) *J. Cell. Biol.* **114,** 401–411.
19. Katenbach, J. P., Katenbach, M. H., and Lyons, W. B. (1958) *Exp. Cell Res.* **15,** 112–117.
20. Bender, A., Amann, U., Jager, R., Nain, M., and Gemsa, D. (1993) *J. Immunol.* **151,** 5416–5424.
21. Rodgers, B., and Mims, C. A. (1981) *Infect. Immun.* **31,** 751–757.
22. Dive, C., Gregory, C. D., Phipps, D. J., Evans, D. L., Milner, A. E., and Wyllie, A. H. (1992) *Biochim. Biophys. Acta* **1133,** 275–285.
23. Belloc, F., Dumain, P., Boisseau, M. R., Jalloustre, C., Reiffers, J., Bernard, P., and Lancone, F. (1994) *Cytometry* **17,** 59–65.
24. Nain, M., Hinder, F., Gong, J.-H., Schmidt, A., Bender, A., Sprenger, H., and Gemsa, D. (1990) *J. Immunol.* **145,** 1921–1928.
25. Bortner, C. D., Oldenburg, N. B. E., and Cidlowski, J. A. (1995) *Trends Cell Biol.* **5,** 21–26.
26. Martin, S. J., Green, D. R., and Cotter, T. G. (1994) *Trends Biochem. Sci.* **19,** 26–30.
27. Eastman, A. (1995) *Methods Cell Biol.* **45,** 41–55.
28. Kerr, J. F., Golbe, G. C., Winterford, C. M., and Harmon, B. V. (1995) *Methods Cell Biol.* **46,** 1–27.
29. Hurwitz, C., and Tolmach, L. J. (1969) *Biophys. J.* **9,** 607–633.
30. Knipe, D. M. (1990) *in* Virology (Fields, B. N., and Knipe, D. M., Eds.), 2nd ed., pp. 293–314, Raven Press, New York.
31. Laster, S. M., Wood, J. G., and Gooding, L. R. (1988) *J. Immunol.* **141,** 2629–2634.
32. Mullinger, A. M., and Johnson, R. T. (1976) *J. Cell. Sci.* **22,** 242–285.
33. Sanderson, C. J. (1976) *Proc. R. Soc. London B* **192,** 241–255.
34. Alpuche-Aranda, C. M., Racoosin, E. L., Swanson, J. A., and Miller, S. I. (1994) *J. Exp. Med.* **179,** 601–608.
35. Shibata, S., Kyuwa, S., Lee, S.-K., Toyoda, Y., and Goto, N. (1994) *J. Virol.* **68,** 7540–7545.
36. Lamb, R. A., and Krug, R. M. (1996) *in* Virology (Fields, B. N., Howley, P. M., and Knipe, D. M., Eds.), 2nd ed., pp. 1353–1396, Lippincott-Raven, New York.
37. Schwarz, K. B. (1996) *Free Radical Biol. Med.* **21**(5), 641–649.
38. Lin, K.-I., Lee, S.-H., Narayanan, R., Baraban, J. M., Hardwick, J. M., and Ratan, R. R. (1995) *J. Cell. Biol.* **131,** 1149–1161.
39. Kroemer, G., Zamzami, N., and Susin, S. A. (1997) *Immunol. Today* **18,** 44–51.
40. Razvi, E. S., and Welsh, R. M. (1995) *Adv. Virus Res.* **45,** 1–60.
41. Oberhammer, F., Wilson, J. W., Dive, C., Morris, I. D., Hickman, J. A., Wakerling, A. E., Walder, P. R., and Sikorska, M. (1993) *EMBO J.* **12,** 3679–3684.
42. Pescheke, T., Bender, A., Nain, M., and Gemsa, D. (1993) *Immunobiology* **189,** 340–355.
43. Khelef, N., Zychlinsky, A., and Guiso, N. (1993) *Infect. Immun.* **61,** 4064–4071.
44. Zychlinsky, A., Prevost, M. C., and Sansonetti, P. J. (1992) *Nature* **358,** 167–169.
45. Munn, D. H., Beall, A. C., Song, D., Wrenn, R. W., and Throckmorton, D. C. (1995) *J. Exp. Med.* **181,** 127–136.
46. Fujihara, M., Ito, N., Pace, J. L., Watanabe, Y., Russell, S. W., and Suzuki, T. (1994) *J. Biol. Chem.* **269,** 12773–12778.
47. Pahl, H. L., and Baeuerle, P. A. (1995) *J. Virol.* **69,** 1480–1484.
48. Olsen, C. W., Dybdahl-Sissoko, N., and Hinshaw, V. S. (1996) *Death Differ.* **3,** 191–197.
49. Sprenger, H., Bacher, M., Rischkowsky, E., Bender, A., Nain, M., and Gemsa, G. (1994) *J. Immunol.* **152,** 280–288.
50. Chen, B. D.-M., and Lin, H.-S. (1984) *J. Immunol.* **132,** 2955–2960.
51. Miyakawa, Y., Kagaya, K., Watanabe, K., and Fukazawa, Y. (1995) *Microbiol. Immunol.* **33,** 1027–1038.
52. Salo, R. J., Bleam, D. K., Greer, V. L., and Ortega, A. P. (1985) *J. Leukocyte Biol.* **37,** 395–406.
53. Tosk, J., Lau, B. H. S., Myers, R. C., and Torrey, R. R. (1989) *J. Leukocyte Biol.* **46,** 103–108.
54. Sakurai, A., Satomi, N., and Haranaka, K. (1985) *Cancer Immunol. Immunother.* **20,** 6–10.

Received November 22, 1996
Revised version received March 5, 1997

ANNALS OF CLINICAL AND LABORATORY SCIENCE, Vol. 27, No. 3

Effects of Reactive Oxygen and Nitrogen Species Induced by Ammonium Dinitramide Decomposition in Aqueous Solutions of Deoxyribose Nucleic Acid*

LINDA STEEL-GOODWIN, Ph.D.,†
K. J. KUHLMAN, B.S.,‡
CLAY MILLER, M.S.,§
M. D. PACE, Ph.D.,‖
and A. J. CARMICHAEL, Ph.D.¶

†Tri-Service Toxicology, Armstrong Laboratory, Wright-Patterson AFB, OH 45433
and
‡Mantech Environmental, Inc., Dayton, OH 45431
and
§Walter Reed Army Toxicology Detachment, Dayton, OH 45431
and
‖Naval Research Laboratory, Washington, DC 20332
and
¶Armed Forces Radiobiology Research Institute, Bethesda, MD 20332

ABSTRACT

Ammonium dinitramide (ADN), a potential rocket fuel, decomposes in water forming NO_2. The chemistry of this ADN-released NO_2 in oxygenated biological systems is complex both in the number of potential chemical species and in the number of parallel and consecutive reactions that can theoretically occur. High-pressure liquid chromatography (HPLC) studies revealed ADN fragmented deoxyribose nucleic acid (DNA). Damage to DNA standard solutions was caused by at least two major pathways, one arising from reactions of NO_2 with oxygen and one arising from a reaction with superoxide ($O_2^{-\bullet}$). The radical species generated when ADN is incubated with standard solutions of DNA, pH 7.5, in the presence of the spin trap agent n-tert-butyl-α-nitrone (PBN) was compared with the PBN-radical adducts generated in the presence of ADN and $O_2^{-\bullet}$ or of ADN and hydrogen peroxide (H_2O_2). The ADN-induced PBN radical adducts increased linearly over the 90-minute study period. The values of peak intensity in the presence of $O_2^{-\bullet}$ and in the presence of H_2O_2, were 828% and 7.08%, respectively, of the ADN-induced

* Send reprint requests to Major Linda Steel-Goodwin, Ph.D., Air Force Office of Scientific Research, 110 Duncan Avenue, Suite B115, Bolling Air Force Base, Washington, DC 20332-8080.

0091-7370/97/0500-0000 $01.50 © Institute for Clinical Science, Inc.

radicals alone. The synergistic effect of ADN with O_2^- may provide an understanding of the sensitivity of the rat blastocyst to ADN at the preimplantation stage of development and the lack of toxicity in *in vivo* studies in tissues high in catalase.

Introduction

The general objective of this research was to study toxic free-radical mechanisms induced in biomolecules following exposure to ammonium dinitramide (ADN). Free radicals are compounds containing an unpaired electron.[1,2,3] The specific goals were twofold: first, to study the effects ADN, a nitrogen dioxide producing agent, induced in deoxyribose nucleic acid (DNA), and second, to correlate the free radicals produced with radical-radical reactions of ADN in the presence of DNA. The purpose of this correlation was to provide information on the possible pathways of ADN induced DNA injury.

Ammonium dinitramide is a constituent in rocket propellants.[4] Because the environmental effects and toxicity of this highly energetic material are being evaluated, an understanding of at least its decomposition is necessary to ensure that decomposition products cause no environmental problems. Ammonium dinitramide is an oxidizing agent and breaks down to form the free radical NO_2.[5,6] In aqueous media, ADN produces the free radical $NO^{\cdot}$ as well as NO_2 and NO_3,* both of which are known environmental pollutants that can cause acid rain. Before full-scale use, ADN's toxic effects should be known in order to assess the concentration that could affect personnel exposed intentionally, accidentally, or occupationally. As is common, assessment of human risk can be based on data from animal studies.

Rodent bioassays conducted on ADN[7] and *in vivo* rodent reproductive studies[8,9] as well as *in vitro* enzyme linked immunoassay (ELISA) studies[10,11] suggest DNA can be damaged on exposure to ADN. The present study was performed to confirm or refute this assumption.

The goals of this study were achieved with commercially available DNA, and the techniques of high-pressure liquid chromatography (HPLC) and electron paramagnetic resonance (EPR)/spin trapping. The versatile technique of HPLC that separates substances in solution, was used to determine if ADN fragments DNA.[12] A magnetic resonance technique, EPR measures the effect of a magnetic field on an unpaired electron (free radicals and transition metals). The technique measures the effect of a magnetic field on the unpaired electron.[1,2] The spinning electron acts as a small magnet. It also interacts with neighboring nuclei. When placed in an external magnetic field, information is obtained regarding the local environment surrounding the unpaired electron.

The number of EPR lines that will be obtained can be predicted from the equation: $2\ \Sigma M_I + 1$ where I is the nuclear spin. For example, nitrogen that has a nuclear spin of 1 forms three lines on the EPR spectra. The EPR is the most sensitive and direct method for studying free radicals.[1,2] Spin trapping is the reaction of a short-lived free radical with a spin trap, usually a nitrone or nitroso compound, yielding a longer-lived nitroxide spin adduct that can be measured and identified by EPR.[1,2]

Free-radical mechanisms are a natural process in biological systems. Superoxide ($O_2^{\cdot-}$) and nitric oxide ($NO^{\cdot}$) are produced beneficially as part of various biochemical pathways in many cells. In the normal functioning cell, these radicals are in harmony, and their levels are balanced by antioxidants in cells.[13] However, when this radical/antioxidant balance is altered by induction of one of these species or by the presence of other free radicals (*eg*, carbon-centered radicals) generated as metabolites of xenobiotic agents, a chain of events may occur through the propagation of free radical pathways that ultimately lead to cell transformation and/or death.[3,13]

In vivo studies show high levels of ADN can induce anemia[14] in rats, but the major target

* MD Pace, unpublished data.

for ADN toxicity effects is the rat fetus because ADN administered in drinking water has been shown to be a rat reproductive toxin.[8,9] Both HPLC and EPR/spin trapping techniques were used to elucidate whether or not free radicals play a role in damaging DNA and to suggest a mechanism to explain the ADN *in vivo* findings.[8,9,14]

Method and Materials

Reagents

The ammonium dinitramide* (ADN, $NH_4^+(NO_2)_2^-$) used in this study contained 1 to 2 percent ammonium nitrate as the hazardous ingredient. The standard DNA used in this study was either herring sperm DNA† or λ-phage DNA.‡ All other chemicals were analytical grade.

HPLC

A sample of herring sperm DNA prepared in an aqueous solution (5ng/ml in 0.1 mM ethylenediamine tetracetic acid (EDTA), 10 mM Tris pH7.5 and 120 mM NaCl) was split, and one portion was exposed to 1 mM ADN. These samples were then run qualitatively by HPLC, using an isocratic method with 100% methanol and storing all spectra from 190 to 600 nm from the diode array detector.

EPR/Spin Trapping

A sample of λ-phage DNA (5ng/ml in 0.1 mM EDTA, 10 mM Tris pH 7.5, and 120 mM NaCl) was incubated for 90 minutes with 50 mM n-tert-butyl-α-nitrone (PBN) with and without 1 mM ADN and without or in the presence of either 5 μl of saturated potassium superoxide in dimethyl sulfoxide or 5 μl of 40 percent v/v hydrogen peroxide). Samples (20-ul) were placed in capillary tubes and the EPR spectrum was measured every 3 min for 90 min with an EMS104 EPR analyzer§ having the following parameters: microwave power, 25 mW; sweep width, 100 G; modulation amplitude, 1.80 G; sweep time, 20.97 s; filter time constant, 20.48 ms; receiver gain, 30.

Calculations

The peak intensity values of ADN and DNA, of ADN, DNA, and $O_2^{-\cdot}$, or of ADN, DNA, and H_2O_2 were subtracted from the respective control data (DNA alone, DNA and $O_2^{-\cdot}$, or DNA with H_2O_2). The data was plotted with time and linear regression measured.‖

Results

In figure 1 is shown the HPLC isocratic plot. The gray-scale plot, which varies from −0.7 adsorbance units (darkest) to 6.5 absorbance units (lightest) of the raw solvent is shown in figure 1A. It is virtually identical to the plot of solvent and DNA alone (figure 1B). When DNA was exposed to ADN (figure 1C), the plot clearly shows considerable absorbance at approximately 2 minutes, the approximate time that the injection takes to travel through the system when unretained. In the actual plot at the instrument, using a different scale, this absorbance extends to 600 nm. This is a clear indication that the ADN is decomposing the DNA, probably into its nitrogen base components.

In figure 2 are shown selected spectra of n-tert-butyl-α-nitrone (PBN)-radical adducts generated when DNA was incubated over a 90-minute period in the presence of ADN. Initially the ADN-induced PBN radical was a 1:2:2:1 quartet seen at the 23-minute time point (figure 2A); then, a second radical, a triplet of triplets, was formed at the 67-minute time point (figure 2B). Both these radicals were present by the 20-minute time point when $O_2^{-\cdot}$ was also present in the reaction mixture (figure 2C).

In contrast, the initial ADN-induced PBN adduct was suppressed when hydrogen peroxide (H_2O_2) replaced $O_2^{-\cdot}$ in the reaction mix-

* SRI International, Menlo Park, CA.
† Boehringer Mannheim.
‡ Sigma/Aldrich Chemicals.
§ Bruker Instruments Inc, Billerica, MS.
‖ Sigma Suite, Jandel Corporation, San Rafael, CA.

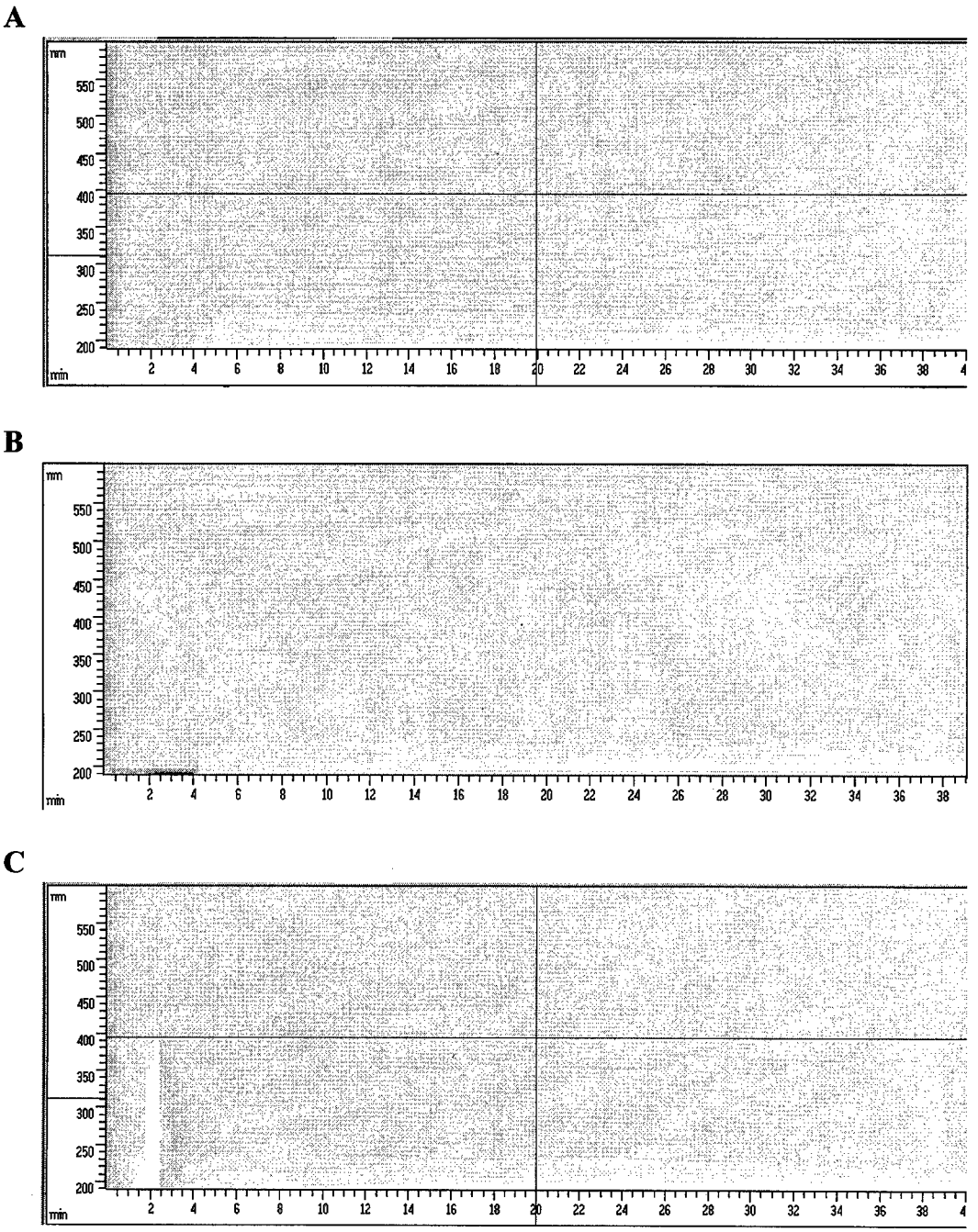

FIGURE 1. The high pressure liquid chromatography data of (A) the plot of raw solvent, (B) deoxyribonucleic acid (DNA) alone, and (C) DNA exposed to 1mM ammonium dinitramide.

ture (figure 2D). Control DNA without ADN produced no radicals (figure 2E). The hyperfine couplings (hfcs) of these radicals at each time point in figure 2 are given in table I. This table shows that the reactions continue to progress during the experiment and that as

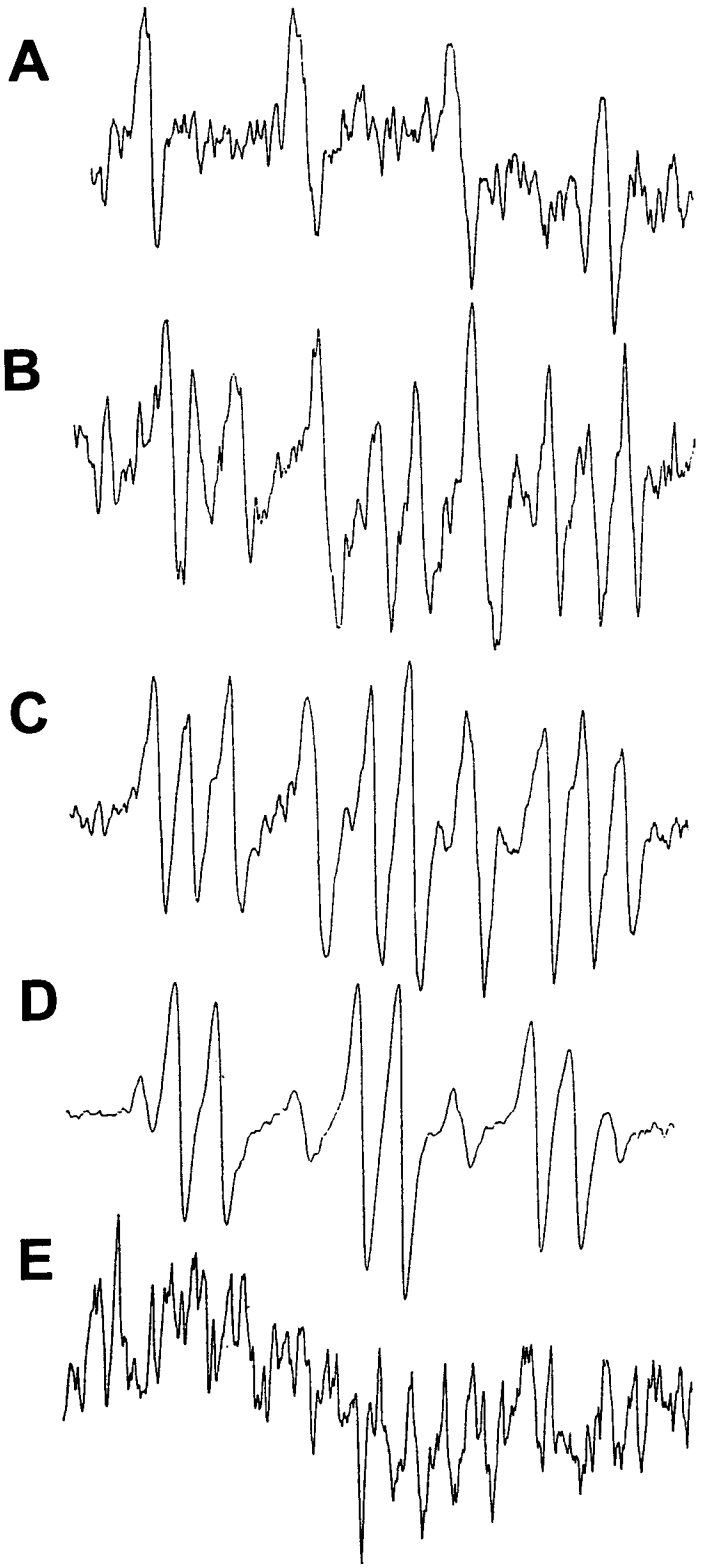

FIGURE 2. First derivative electron paramagnetic resonance spectra of 20 μl samples of deoxyribonucleic acid (DNA) treated with a variety of reactive species: (A) 1 mM of ammonium dinitramide (ADN) for 20 min; (B) 1 mM of ADN for 67 min; (C) 1 mM of ADN and 5 μl of potassium superoxide in 1 ml of total sample, (D) 1 mM of ADN and 5 μl of 40 percent hydrogen peroxide in 1 ml of total sample (E) DNA control, 1 ml of total sample.

TABLE I

Spin Adducts Hyperfine Coupling Constants

Experiment	*Radical*	a_N	$a_{H\beta}$
ADN+DNA	1:2:2:1	1.363	1.363
23 minutes			
ADN+DNA	1:2:2:1	1.367	1.367
67 minutes	2:2:2	1.594	0.386
ADN+DNA+$O_2^{-\cdot}$	1:2:2:1	1.418	1.418
20 minutes	2:2:2	1.617	0.357
ADN+DNA+H_2O_2	1:2:2:1	1.40	1.40
16 minutes	2:2:2	1.615	0.3635

ADN = ammonium dinitramide.
DNA = deoxyribose nucleic acid.
H_2O_2 = hydrogen peroxide.

one radical is formed another is suppressed, resulting in slightly different hfcs in the EPR spectra.

In figure 3, plots of the intensity of the radicals that were generated in the samples (A = ADN and DNA; B = ADN, DNA; and $O_2^{-\cdot}$, C = ADN, DNA, and H_2O_2) and were subtracted from their respective control samples: (A = DNA alone, B = DNA and $O_2^{-\cdot}$; and C = DNA and H_2O_2). The regression analysis of the data is shown in table II.

In figures 2 and 3, it is shown that the combination of ADN and $O_2^{-\cdot}$ increased the peak intensity of ADN-induced PBN radical adducts trapped, while H_2O_2 suppressed the ADN-induced PBN radical adducts trapped. The values of peak intensity at the 90-minute time point was calculated, from the data given in table II, to be 828 percent and 7.08 percent, respectively, of the ADN-induced PBN radical adducts in the presence of $O_2^{-\cdot}$ and H_2O_2, respectively.

Discussion

High pressure liquid chromatography studies showed ADN will fragment DNA (figure

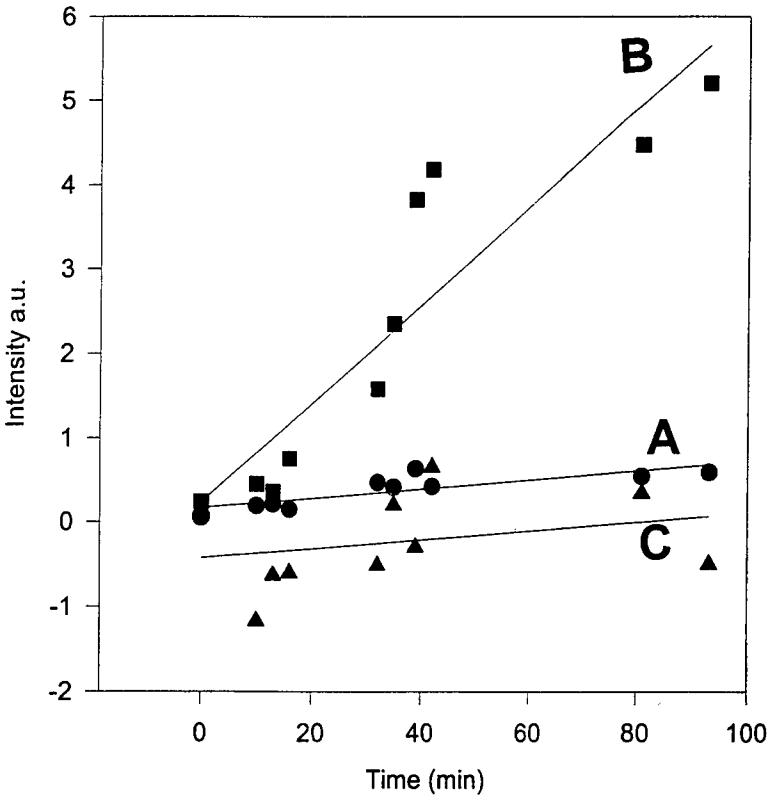

FIGURE 3. Free-radical formation of deoxyribonucleic acid (DNA) exposed at 25°C to a variety of reactive species over the reaction time of 90 mins: (A) ● 1 mM of ammonium dinitramide (ADN), (B) ■ 1 mM of ADN and 5 µl of potassium superoxide in 1 ml of total sample; (C) Δ1 mM of ADN and 5 µl of 40 percent hydrogen peroxide in 1 ml of total sample. The radical intensity is measured in arbitary units (a.u.).

TABLE II

Regression Values

Experiment	b [0]	b [1]	r^2	n
(ADN + DNA)	0.7107	$4.1306e^{-3}$	0.646	30
(DNA)	0.5061	$1.5938e^{-3}$	0.152	30
(ADN + DNA) – (DNA)	0.1683	$5.4471e^{-3}$	0.671	10
(ADN + DNA + $O_2^{-}\cdot$)	0.2977	0.0632	0.9923	30
(DNA + $O_2^{-}\cdot$)	0.4326	$8.9389e^{-4}$	0.2435	24
(ADN + DNA + $O_2^{-}\cdot$) – (DNA = $O_2^{-}\cdot$)	0.2387	0.0582	0.8381	11
(ADN + DNA + H_2O_2)	2.5804	0.1417	0.9639	28
(DNA + H_2O_2)	2.5891	0.1513	0.9923	30
(ADN + DNA + H_2O_2) – (DNA + H_2O_2)	–0.4272	$5.2674e^{-3}$	0.0827	13

ADN = ammonium dinitramide.
DNA = deoxyribose nucleic acid.
H_2O_2 = hydrogen peroxide.

1). This was anticipated because agarose gel electrophoresis studies of DNA extracted by lysis from WB344 rat liver cells exposed to ADN gave a classical DNA ladder typical of apoptotic cells.* Photomeric ELISA studies using 5-bromo-2-deoxyuridine (BrdU)[10] support the electrophoresis data and also the current HPLC results. These data together suggest ADN could cause point mutations in DNA, and this could explain the ADN genotoxicity study results.[7,11]

The formulas in figure 4 show that theoretically ADN in reactions arising from the ADN radical decomposition product nitric oxide (NO) and $O_2^{-\bullet}$ can deaminate DNA bases. Deamination of 5-BrdU by ADN is not possible as there is no site for ADN to deaminate, but ADN can deaminate cytosine to uracil, adenine to hypoxanthine, and guanine to xanthine. Deamination reactions and the DNA damage induced have been reviewed elsewhere.[15]

The theoretical series of radical-radical reactions that could occur to generate NO˙ to deaminate DNA and cause cytotoxicity are shown in figure 5. The radical reactions of ADN with DNA were investigated by EPR spin trapping using the spin trap PBN. The spectra are shown in figure 2. These spectra, despite being at different time points, have PBN-radical adducts of similar hfcs suggesting the radicals trapped by PBN are the same but are trapped at different stages of the reaction. The radical-radical interactions that could occur between DNA and ADN alone and in the presence of $O_2^{-\bullet}$ and H_2O_2 are also shown in figure 5. The scheme of equations (1 to 15) shows, by chemical reactions, why it was possible to see experimentally (figures 2 and 3) an increase in radical intensity in the presence of ($O_2^{-\bullet}$) and the suppression of radical species in the presence of H_2O_2.

The effects of ADN in the presence of H_2O_2 and saturated potassium superoxide ($O_2^{-\bullet}$) provide reducing and oxidizing environments. Both H_2O_2 and $O_2^{-\bullet}$ can both be biologically generated.[16] It is possible that these reactive oxygen and nitrogen intermediates may be induced in cells following exposure to ADN, and this could lead to oxidative stress and DNA damage. Cell death does occur on ADN exposure *in vitro*.[10,11] The EPR/spin trapping has shown ADN forms two types of radical adducts with PBN: a 1:2:2:1 quartet and a triplet of triplets (figure 2). These same radical species are seen in the presence of $O_2^{\cdot-}$ and H_2O_2. The quartet is believed to be the con-

* M. Hale, L. Steel-Goodwin, and A. J. Carmichael unpublished data.

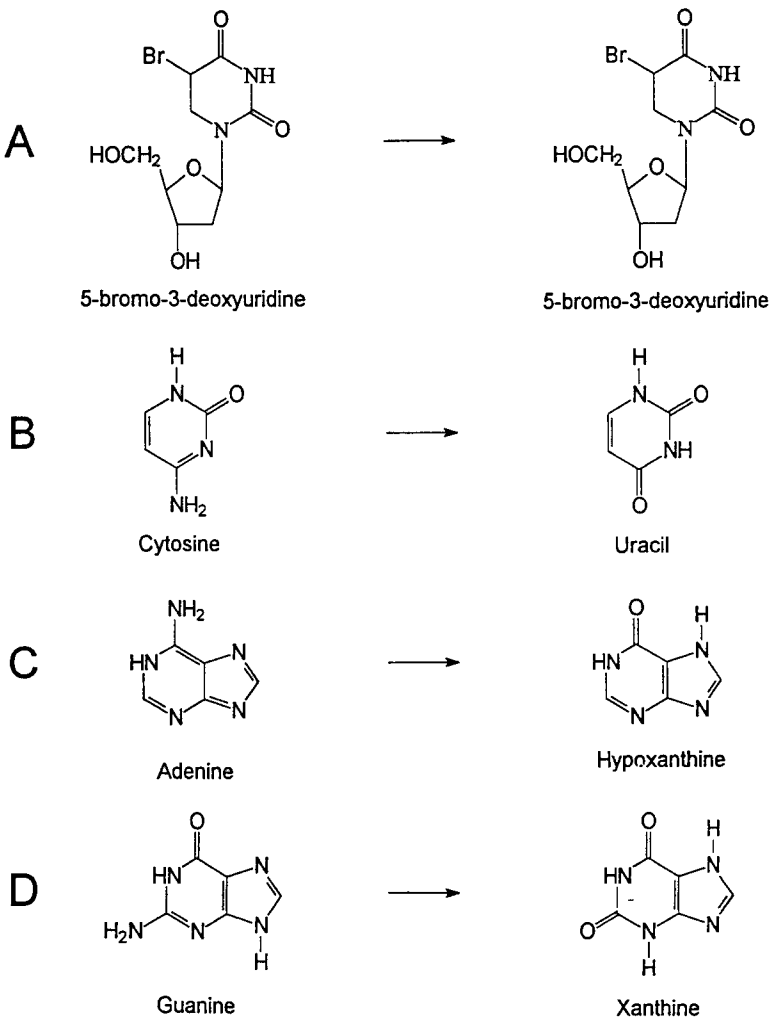

FIGURE 4. Potential products of representative nucleic acid bases following exposure to ammonium dinitramide (a) 5-bromo 3-deoxy-uridine, no change. (B) cytosine to uracil. (C) adenine to hypoxanthine. (D) guanine to xanthine.

version of PBN into the reduction product H-MNP of the nitroso spin trap 2-methyl-2-nitrosopropane (MNP). This chemical conversion of PBN was first demonstrated in studies involving phosgene gas.[17] It is possible the triplet of triplets seen in figures 2B, 2C, and 2D is a further decomposition product of H-MNP.

The generation of the two radical species shown in the spectra figure 2 indicates that ADN is highly reactive in oxygenated aqueous environments. Biological systems are composed mainly of water and, theoretically, ADN can initiate a cascade of radical events and chemical reactions that could be deleterious to cells. Cells poor in antioxidants would be especially vulnerable to ADN. Review of the *in vivo* studies where rats were administered ADN in drinking water[8,9,14] showed no pathological changes except in fetus number and red blood cell hemolysis.

Free-radical studies on reproduction are rare. Development of embryos require implantation in the maternal endometrium. It is known that $O_2^{-\bullet}$ reconfigures endometrial membrane to favor attachment of the blastocyst.[18] There is a peak in $O_2^{-\bullet}$ at the peri-implantation stage as compared with preimplantation and postimplantation phases. Because $O_2^{-\bullet}$ is so reactive, its release and concentration is controlled by antioxidants. It is possible that the addition of ADN can alter the

1.	$2NH_4^+N(NO_2)_2$	→	$2NH_3^\bullet + 4NO_2^\bullet + 2H^+ + N_2$
2.	$NH_3^\bullet + H^+$	→	NH_4^+
3.	$2H^+ + O_2^{-\bullet} + O_2^{-\bullet}$	→	$H_2O_2 + O_2$
4.	$NO + O_2$	→	$O_2NO^\bullet$
6.	$O_2NO^\bullet + NO$	→	$2NO_2$
7.	$2NO_2$	→	N_2O_4
8.	$NO + NO_2$	→	N_2O_3
9.	$N_2O_3 + H_2O$	→	$2H^+ + 2NO_2^-$
10.	$N_2O_4 + H_2O$	→	$2H^+ + NO_2^- + NO_3^-$
11.	$H_2O_2 + NO_2^- + H^+$	→	$ONOOH + H_2O$
12.	$O_2^{-\bullet} + NO^\bullet + H^+$	→	$ONOOH$
13.	$ONOOH$	→	$^\bullet OH + NO_2^\bullet$
14.	$^\bullet OH + NO_2^\bullet$	→	$NO_3^- + H^+$
15.	$H_2O_2 + O_2^{-\bullet}$	→	$O_2 + OH^- + {}^\bullet OH$

FIGURE 5. Reactions arising from decomposition of ammonium dinitramide in aqueous solutions of deoxyribonucleic acid in the presence of $O_2^{\cdot -}$ and H_2O_2.

membrane fluidity of the blastocyst so much so that the blastocyte cannot implant, and membrane leakage occurs. *In vitro* studies have shown ADN increases membrane leakage of WB344 rat liver cells and human red blood cells.[19]

In addition, release of NO· radicals due to a radical-radical cascade induced by ADN can cause increased smooth muscle motility of the uterus. Increased uterine contraction could make it difficult for the blastocyst to remain stationary on the surface of the endometrium long enough to adhere to the endometrium and develop further. Free-radical and histopathology studies are in progress to determine the role free-radical events play in ADN-induced membrane changes of preimplantation, peri-implantation and postimplantation blastocysts.

Ammonium dinitramide had no toxic effect *in vivo* in cells that contain high levels of catalase (*e.g.*, liver cells).[14] Based on the H_2O_2 results (figure 2D and figure 3), the lack of toxicity in liver *in vivo* is explained by the high levels of catalase normally present in hepatocytes. However, this does not explain the effects of ADN-induced damage to red blood cells[14] *in vivo* because erythrocytes, like liver, also have high levels of catalase. However, recent studies[20] suggest red cell damage could occur through the ability of red cells to sequester NO· in hemoglobin. The radical-radical reactions shown in figure 5 can propagate and ultimately cause red cell damage and lead to the red cell hemolysis found in rats supplied with drinking water containing high concentrations of ADN.[14]

In conclusion, this study shows that ADN will fragment DNA *in vitro* by a series of complex chemical reactions. The number of radicals spin trapped and detected by EPR in the presence of $O_2^{\cdot -}$ at the 90-minute time point

was 828 percent of that of the ADN-induced radicals alone. This synergistic effect may account for the ADN-induced alteration of embryo implantation numbers seen in rats *in vivo*.[8,9] Alternatively, the number of radicals generated in the presence of H_2O_2 was only 7.08% of that of the ADN-induced radicals at the 90-minute time point. The majority of mammalian cells are high in catalase which may naturally ameliorate the ability of ADN to cause damage and could explain the negligible toxicity when ADN was administered to rats via drinking water.[14]

Acknowledgments

The authors wish to acknowledge Dr. Linda Graeter who came to us with this challenge. It is our hope that this study will assist with interpretation of her ongoing research on reproductive effects of ammonium dinitramide.

This project was supported by the U.S. Army under work unit 7757A202, ManTech Environmental Inc., Dayton, OH, contract number F29, and by the Air Force Office of Scientific Research under work unit number A2312A202. Views presented in this paper are those of the authors; no endorsement by the U.S. Army or U.S. Air Force has been given or should be inferred.

References

1. Buettner GR. The spin trapping of superoxide and hydroxyl radicals. In: Oberley LW, editor. Superoxide Dismutase, Vol II. Boca Raton, FL: CRC Press, 1982: 64–81.
2. Rice-Evans CA, Diplock AT, Symons MCR. In: Burdon RH, van Knippenberg PH, editors. Techniques in free radical research. New York: Elsevier 1991.
3. Kehrer JP. Free radicals as mediators of tissue injury and disease. Critical Reviews in Toxicology 1993;23: 21–48.
4. Borman S. Advanced energetic materials emerge for military and space applications. Chem Eng News 1994;72:18–22.
5. Pace MD. Spin trapping of nitrogen dioxide from photolysis of sodium nitrite, ammonium nitrite, ammonium dinitramide and cyclic nitrosamines. J Phys Chem 1994;98:6251–7.
6. Steel-Goodwin L, Pace MD, Carmichael AJ. Ammonium dinitramide: An EPR/ENDOR study 1995; AL/OE-TR-1995-0160 Armstrong Laboratory Wright-Patterson Air Force Base, OH.
7. Zhu S, Korytynski E, Sharma S. Genotoxicity assays of ammonium dinitramide: I, Salmonella/Microsome Mutagenesis, II. Mouse Lymphoma Cell Mutagenesis, III. *In vivo* Mouse Bone Marrow Micronuclei Test. 1994; AL/OE-TR-1994-0148 Armstrong Laboratory Wright-Pattern Air Force Base, OH.
8. Kinead ER, Wolfe RE, Flemming CD, Leahy HF, Caldwell DJ, Miller CR, Marit GB. Reproductive toxicity screen of ammonium dinitramide administered in the drinking water of Sprague-Dawley rats. Toxicol Indust Health 1995;11:437–48.
9. Graeter LJ. Preimplantation effects of ammonium dinitramide (ADN) administered in the drinking water of Sprague-Dawley rats. The Toxicologist 1996; 30:Abstract # 626.
10. Steel-Goodwin L, Dean KW. Apoptosis in liver cells on exposure to ammonium dinitramide. Ann Clin Lab Sci 1995;25:357–8.
11. Dean KD, Channel SR. *In vitro* effects of ammonium dinitramide. The Toxicologist 1996;30:Abstract # 234.
12. Koenigsberger R. High performance liquid chromatography. In: Williams DL, Nunn RF, Marks V, editors. Scientific Fundamentals of Clinical Biochemistry. London: William Heinman Medical Books Ltd. 1978:165–85.
13. Carmichael AJ, Steel-Goodwin L, Gray B, Arroyo CM. Reactions of active oxygen and nitrogen species studied by EPR and spin trapping. Free Rad Res Comms 1993;19:S1–S16.
14. Kinkead ER, Salins SA, Wolfe RE, Marit GB. Acute and subacute toxicity evaluation of ammonium dinitramide. 1994; AL-TR-1994-0071 Wright-Patterson Air Force Base, OH.
15. Tannenbaum SR, Tamir S, de Rojas-Walker T, Wishnok JS. DNA damage and cytotoxicity caused by nitric oxide. In: Loeppky RN, Michejda CJ, editors. Nitrosamines and Related N-Nitroso Compounds Chemistry and Biochemistry. Washington DC: American Chemical Society, 1994:120–135.
16. Gutteridge JMC. Lipid peroxidation and antioxidants as biomarkers of tissue damage. Clin Chem 1995 41;12B:1819–28.
17. Arroyo CM, Feliciano F, Kolb DL, Keeler JR, Millette SR, Stotts RR. Autoionization reaction of phosgene ($OCCl_2$) studied by EPR. J Biochem Toxicol 1993;8:107–10.
18. Thomas M, Jain S, Kumar G, Laloraya P, Laloraya M. Free radical and blastocyst implantation. J Free Rad Biol Med 1994;2:A40.
19. Steel-Goodwin L, Music FC, Dean KW, Flemming CF, Pace MD, Carmichael AJ. Spin label assays using protein conjugates to measure receptor binding by electron paramagnetic resonance. J Soc Armed Forces Med Lab Sci 1996;25:33 O–9.
20. Jai L, Bonaventura C, Bonaventura J, Stamler JS. S-nitrosohemoglobin: A dynamic acity of blood involved in vascular control. Nature 1996;380:221–4.

ENDOCRINE RESEARCH, 23(4), 365-376 (1997)

ALTERED THYROID AXIS FUNCTION IN LEWIS RATS WITH GENETICALLY DEFECTIVE HYPOTHALAMIC CRH/VP NEUROSECRETORY CELLS

Mark H. Whitnall and Robert C. Smallridge
Radiation Pathophysiology and Toxicology Department, Armed Forces Radiobiology Research Institute, Bethesda, MD 20889-5603 and Division of Medicine, Walter Reed Army Institute of Research, Washington, DC 20307-5100

ABSTRACT

Lewis rats display hyporesponsive hypothalamo-pituitary-adrenocortical (HPA) axes, overproduction of cytokines, and susceptibility to inflammatory disease. The Lewis corticotropin-releasing hormone (CRH) neurosecretory system contains normal numbers of vasopressin (VP)-deficient axon varicosities, but abnormally sparse VP-containing varicosities in the external zone of the median eminence, compared to the normoresponsive Sprague Dawley (SD), Wistar and Fischer 344 strains. Since VP may act as a thyrotropin-releasing factor, we hypothesized that thyroid axis responsivity may be altered in Lewis rats. T_3, T_4 and TSH were measured by radioimmunoassay, and free T_4 by equilibrium dialysis, in adult male Lewis and SD rats. One h cold (5°C) induced significant increases in T_3, T_4 and TSH levels in Lewis rats but not in SD rats. Ninety min insulin-induced hypoglycemia (1 IU/kg, ip) induced a significant T_3 increase in Lewis rats and a significant T_4 increase in SD rats. Two h after ip LPS (0.25 or 0.75 mg/kg), T_4 levels fell significantly in Lewis rats but not in SD rats. TSH decreases were significant in Lewis rats after 0.75 mg/kg and in SD rats after 0.25 mg/kg. Baseline hormone levels were generally higher in Lewis rats; the differences were significant for T_3 and T_4 in the insulin experiments and for T_3, T_4 and free T_4 in the LPS experiments. The data suggest that reduced inhibition from the adrenocortical axis in Lewis rats leads to hyperresponsivity of the

thyroid axis to cold, and greater LPS-induced decreases in T_4 levels, probably due to an exaggerated inhibitory cytokine response.

INTRODUCTION

Lewis rats display blunted ACTH and corticosterone responses to stimuli and lower 24 h levels of glucocorticoids than other standard laboratory strains (1-7). We recently showed that the parvocellular CRH neurosecretory system in Lewis rats is defective in terms of VP content (8), in contrast to the magnocellular system, which contains abnormally high levels of VP (9). Preliminary results indicate that Lewis rats exhibit abnormally high mortality after whole body gamma irradiation (unpublished), and low thyroid hormone levels during radiation-induced sepsis, compared to SD rats (unpublished). Since VP may regulate TSH release from the anterior pituitary (10, 11), we tested the hypothesis that thyroid regulation in Lewis rats is abnormal. Cold and insulin-induced hypoglycemia were used to stimulate the thyroid axis. Bacterial lipopolysaccharide (LPS) was used as a model of sepsis to inhibit the thyroid axis. Lewis rats were compared to a standard rat strain (SD) with a normoresponsive hypothalamo-pituitary-adrenocortical (HPA) axis (1, 8).

MATERIALS AND METHODS

Male SD and Lewis rats, 250 ± 25 g in body weight, were purchased from the National Cancer Institute, kept on a 12-h light-dark schedule, and given food and water ad libitum, except for the insulin experiments, when food was withdrawn 18 h before the insulin injection. For each of the three treatments (cold, insulin and LPS), reported values are means of the pooled results from two experiments.

In the cold experiments, animals were briefly immersed in room temperature water to reduce the insulating properties of the fur, and then placed in standard plastic rat housing boxes (with no bedding) in a 5°C cold room for one h. Control animals were not immersed, and were kept in an adjacent room at room temperature (24°C) in their home boxes (with bedding).

In the insulin experiments, animals received ip injections of 1 IU/kg recombinant human insulin (Lilly) or vehicle (phosphate buffered saline, PBS). Blood was collected 90 min after the injection. Plasma glucose was measured in these experiments on a Kodak Ektachem-700 analyzer.

In the LPS experiments, animals received ip injections of 0.25 or 0.75 mg/kg E. Coli 0127:B8 LPS (DIFCO) or vehicle (PBS). Blood was collected 120 min after injection.

Trunk blood was collected and plasma prepared for radioimmunoassay of T_3, T_4, TSH and ACTH as described previously (8, 12). Free T_4 was assayed by equilibrium dialysis using kits from Nichols Institute Diagnostics, San Juan Capistrano, CA.

Significant differences are reported at p values of less than 0.05, obtained using analysis of variance and Fisher's protected least significant difference test.

RESULTS

As expected, baseline levels of ACTH were similar in Lewis and SD rats, and increases after cold exposure, insulin or LPS were significantly higher in SD rats (not shown).

The effects of cold exposure on thyroid hormone levels are shown in Table I. One h of cold exposure resulted in significant elevations of plasma total T_3 and total T_4 in Lewis rats but not in SD rats. TSH was

TABLE I

Plasma hormone levels after cold, insulin-induced hypoglycemia, and LPS in Sprague Dawley and Lewis rats

COLD TREATMENT

Group	T_3 (ng/ml)	N	T_4 (ng/ml)	N	Free T_4 (pmol/L)	N	TSH (ng/ml)	N
SD-Cont	0.673 ± .038	12	4.52 ± .17	7	30.1 ± 1.0	4	1.23 ± .20	4
SD-Cold	0.753 ± .050	20	4.83 ± .15	16	32.9 ± 4.4	7	1.19 ± .15	7
LEW-Cont	0.762 ± .035	12	4.96 ± .21	8	35.9 ± 2.4	4	0.52 ± .07†	4
LEW-Cold	0.949 ± .050*	20	5.48 ± .17*	16	44.3 ± 3.8	8	1.45 ± .15*	8

INSULIN TREATMENT

Group	T_3 (ng/ml)	N	T_4 (ng/ml)	N	Free T_4 (pmol/L)	N	TSH (ng/ml)	N
SD-Cont	0.575 ± .025	15	3.78 ± .24	15	34.0 ± 2.8	6	0.381 ± .046	14
SD-Ins	0.578 ± .021	17	4.66 ± .23*	17	32.3 ± 1.9	7	0.512 ± .034*	7
LEW-Cont	0.662 ± .029†	12	5.20 ± .16†	12	39.6 ± 3.4	6	0.389 ± .034	12
LEW-Ins	0.752 ± .033*	13	5.69 ± .18	13	40.5 ± 2.9	7	0.547 ± .053*	13

LPS TREATMENT

Dose, mg/kg	T_3 (ng/ml)	N	T_4 (ng/ml)	N	Free T_4 (pmol/L)	N	TSH (ng/ml)	N
SD-Cont	0.627 ± .015	14	5.03 ± .20	8	34.0 ± 1.7	4	0.436 ± .044	8
SD-0.25	0.508 ± .024*	17	4.63 ± .20	8	40.9 ± 2.3	4	0.297 ± .014*	8
SD-0.75	0.462 ± .022*	18	4.62 ± .20	9	nd		0.350 ± .055	9
LEW-Cont	0.762 ± .067†	8	6.20 ± .18†	8	47.0 ± 3.6†	4	0.487 ± .044	7
LEW-0.25	0.606 ± .037*	8	4.78 ± .22*	8	49.0 ± 5.1	4	0.394 ± .070	8
LEW-0.75	0.612 ± .041*	9	5.20 ± .29*	9	nd		0.309 ± .016*	9

Values: means ± SEM. * Different from control ($p < 0.05$, ANOVA). † Significant difference, SD-control vs. LEW-control. nd, not done.

also significantly elevated in Lewis but not in SD rats. Free T_4 was not significantly elevated in either strain (Table I).

In fasted animals, insulin-induced hypoglycemia was associated with significant elevations of total T_3 in Lewis rats but not in SD rats (Table I), similar to what was observed after cold exposure. However, total T_4 was significantly elevated in SD but not Lewis rats after this treatment. The treatment caused no significant changes in free T_4. TSH levels were significantly elevated in both strains. Control levels of T_3 and T_4 were significantly higher in Lewis than in SD rats.

Plasma glucose was slightly but significantly lower in Lewis rats than in SD rats in baseline conditions (100 ± 4.7 vs. 107 ± 5.8 mg/dl). The insulin-induced decrease in glucose was somewhat blunted in Lewis rats, resulting in final levels that were significantly higher than in SD rats (48.5 ± 4.2 vs. 39.8 ± 4.7 mg/dl). The percent decreases were 52% (± 10%) and 63% (± 16%) for Lewis and SD rats, respectively (standard errors of percent changes calculated by error propagation).

After LPS injections, levels of total T_4 were significantly decreased in Lewis but not SD rats (Table I). Total T_3 levels were significantly decreased in both strains. Free T_4 levels were not affected. TSH levels were significantly decreased after doses of 0.25 mg/kg in SD rats and 0.75 mg/kg in Lewis rats. Control levels of T_3, T_4 and free T_4 were significantly higher in Lewis rats than in SD rats.

DISCUSSION

Previous studies have shown that the adrenocortical axis in Lewis rats is hyporesponsive compared to SD, Fischer 344 and Wistar rats (1, 2). Although there appears to be a defect in pituitary corticotropes in Lewis rats (13), hyporesponsiveness of the axis is due at least in part to relatively low expression of CRH (2) and VP in the hypothalamic neurosecretory system that regulates the corticotropes (8). It is also possible that there is a defect in the secretory function of these neurosecretory axons in Lewis rats (14). In vitro studies demonstrated defective secretion of CRH from hypothalami of Lewis rats (6). In conscious rats, ip injection of LPS induced subnormal release of CRH and VP from parvocellular axon terminals in Lewis rats compared to SD rats, primarily due to the fact that there were significantly lower baseline levels of stored CRH and VP (8).

We were led to test the hypothesis that the thyroid axis is abnormal in Lewis rats because of evidence that VP may regulate secretion of

TSH from thyrotrope cells in the anterior lobe of the pituitary. When pituitary cells were incubated with VP in vitro, there was a significant and dose-related release of TSH, but not prolactin, growth hormone, follicle-stimulating hormone, or luteinizing hormone, suggesting that VP has thyrotropin-releasing hormone (TRH)-like activity (10). The presence of VP receptors on thyrotrope cells also supports the notion that VP regulates TSH release (11). Since Lewis rats possessed abnormally few VP-containing secretory vesicles in the neurosecretory system that regulates the anterior pituitary, we predicted thyroid axis function would be lower in this strain.

Contrary to our expectations, we found that baseline levels of thyroid hormones were generally higher in Lewis rats than in SD rats, and that changes in thyroid hormone levels after cold exposure were greater in Lewis rats. These data are reminiscent of the study of Fujimoto and Hedge (15), who found that a mutant strain of rat (Brattleboro) with a genetic deficiency of VP synthesis displayed abnormally high resting TSH levels. However, that strain is completely lacking in central VP, including the magnocellular neurosecretory system that regulates fluid homeostasis and electrolyte balance. The multiple endocrine abnormalities in that strain could affect thyroid axis function (10).

Our results suggest that baseline thyroid function in Lewis rats is enhanced due to reduced inhibition from the HPA axis. Activity levels of the thyroid and HPA axes are inversely correlated in many situations (16-25). In the study by Lumpkin et al. (10), VP injected into the third ventricle of conscious rats caused specific decreases in plasma TSH levels, leading the authors to suggest that VP may act in a negative ultrashort feedback loop. The synapses observed between parvocellular CRH and TRH neurosecretory cells could mediate mutual inhibition between the two axes (26). Inhibition of the thyroid axis by glucocorticoids has been demonstrated (16, 18, 27-31). Glucocorticoids inhibit hypothalamic TRH expression (31), and may act at other levels of the thyroid axis (32).

It has been proposed that increased activity in the thyroid axis can result in inhibition of the adrenocortical axis (24). One possible "corticotropin release-inhibiting factor" (CRIF) is preprothyrotropin-releasing hormone-(178-199) (24) (although Nicholson and Orth failed to confirm this result (33)). However, hyperthyroidism in Lewis rats probably is not a major cause of the hyporesponsivity of the HPA axis. The abnormalities in adrenocortical function in Lewis rats are more consistent and of higher magnitude than the thyroid abnormalities. Therefore, it is likely that the primary defect in Lewis rats is hypoactivity of the HPA axis leading to changes in thyroid regulation.

It is well known that cytokines inhibit the thyroid axis (34-39), partly due to suppression of TRH gene expression in the hypothalamus (39). This inhibition may account for the depression of thyroid function commonly observed in severely sick patients whose illnesses do not primarily affect the thyroid axis. The Lewis rat is characterized by exaggerated cytokine responses to stimuli, presumably due to defective inhibition of cytokine expression by the hypoactive HPA axis (7). Higher cytokine release after LPS challenge in Lewis rats would explain the greater decrease in thyroid hormone levels seen in this strain compared to SD rats.

In spite of the changes in levels of T_3, T_4 and TSH induced by the challenges, no significant changes in free T_4 levels were observed, suggesting that changes in free T_4 levels were blunted by binding proteins. The only significant difference observed between any of the groups in terms of free T_4 levels was between control groups of the two strains in the LPS experiments. This difference was consistent with our overall observation of higher resting levels of thyroid hormones in Lewis rats.

In summary, the present findings demonstrate altered thyroid responses in Lewis rats compared to SD rats. The Lewis strain may provide a model for clinical syndromes associated with decreased

inhibition of the thyroid axis by the HPA axis and increased inhibition of the thyroid axis by cytokines.

ACKNOWLEDGMENTS

We thank Drs. David R. Livengood and Robert S. Perlstein for helpful discussions, Dr. Greti Aguilera for performing the ACTH assays, Ms. Irene Gist, Mr. Edward Mougey, and Ms. Toni Cranston for performing the thyroid hormone assays, Ms. Santi Datta for performing the glucose analyses, and Mr. Brian Hively for excellent technical assistance.

Address all correspondence and requests for reprints to: Dr Mark H Whitnall, RPT, AFRRI, Bethesda, MD 20889-5603, tel (301) 295-0277, fax (301) 295-6503, email: whitnall@rockroseweb.com.

Dr. Smallridge's current address is The Mayo Clinic Jacksonville, 4500 San Pablo Rd, Jacksonville, FL 32224.

REFERENCES

1. Sternberg EM, Hill JM, Chrousos GP, Kamilaris T, Listwak SJ, Gold PW, Wilder RL. 1989 Inflammatory mediator-induced hypothalamic-pituitary-adrenal axis activation is defective in streptococcal cell wall arthritis-susceptible Lewis rats. Proc Natl Acad Sci USA 86:2374-2378.

2. Sternberg EM, Young WS, III, Bernardini R, Calogero AE, Chrousos GP, Gold PW, Wilder RL. 1989 A central nervous system defect in biosynthesis of corticotropin-releasing hormone is associated with susceptibility to streptococcal cell wall-induced arthritis in Lewis rats. Proc Natl Acad Sci USA 86:4771-4775.

3. MacPhee IA, Antoni FA, Mason DW. 1989 Spontaneous recovery of rats from experimental allergic encephalomyelitis is dependent on regulation of the immune system by endogenous adrenal corticosteroids. J Exp Med 169:431-445.

4. Griffin AC, Whitacre CC. 1991 Sex and strain differences in the circadian rhythm fluctuation of endocrine and immune function in the rat: implications for rodent models of autoimmune disease. J Neuroimmunol 35:53-64.

5. Villas PA, Dronsfield MJ, Blankenhorn EP. 1991 Experimental allergic encephalomyelitis and corticosterone. Clin Immunol Immunopathol 61:29-40.

6. Calogero AE, Sternberg EM, Bagdy G, Smith C, Bernardini R, Aksentijevich S, Wilder RL, Gold PW, Chrousos GP. 1992 Neurotransmitter-induced hypothalamo-pituitary-adrenal axis responsiveness is defective in inflammatory disease-susceptible Lewis rats: in vivo and in vitro studies suggesting globally defective hypothalamic secretion of corticotropin-releasing hormone. Neuroendocrinology 55:600-608.

7. Perretti M, Duncan GS, Flower RJ, Peers SH. 1993 Serum corticosterone, interleukin-1 and tumour necrosis factor in rat experimental endotoxaemia: comparison between Lewis and Wistar strains. Br J Pharmacol 110:868-874.

8. Whitnall MH, Anderson KA, Lane CA, Mougey EH, Neta R, Perlstein RS. 1994 Decreased vasopressin content in CRH neurosecretory system of Lewis rats. NeuroReport 5:1635-1637.

9. Patchev VK, Mastorakos G, Brady LS, Redwine J, Wilder RL, Chrousos GP. 1993 Increased arginine vasopressin secretion may participate in the enhanced susceptibility of Lewis rats to inflammatory disease. Neuroendocrinology 58:106-110.

10. Lumpkin MD, Samson WK, McCann SM. 1987 Arginine vasopressin as a thyrotropin-releasing hormone. Science (Washington, DC) 235:1070-1073.

11. Childs GV, Westlund KN, Unabia G. 1989 Characterization of anterior pituitary target cells for arginine vasopressin: including cells that store adrenocorticotropin, thyrotropin-beta, and both hormones. Endocrinology 125:554-559.

12. Bernton EW, Beach JE, Holaday JW, Smallridge RC, Fein HG. 1987 Release of multiple hormones by a direct action of interleukin-1 on pituitary cells. Science (Washington, DC) 238:519-521.

13. Bernardini R, Iurato MP, Chiarenza A, Lempereur L, Calogero AE, Sternberg EM. 1996 Adenylate-cyclase-dependent pituitary adrenocorticotropin secretion is defective in the inflammatory-disease-susceptible Lewis rat. Neuroendocrinology 63:468-474.

14. Rivest S, Rivier C. 1994 Stress and interleukin-1ß-induced activation of c-*fos*, NGFI-B and CRF gene expression in the hypothalamic PVN: comparison between Sprague-Dawley, Fisher-344 and Lewis rats. J Neuroendocrinol 6:101-117.

15. Fujimoto S, Hedge GA. 1982 Altered pituitary-thyroid function in the Brattleboro rat with diabetes insipidus. Endocrinology 110:1628-1633.

16. Nicoloff JT, Fisher D, Appleman MD. 1970 The role of glucocorticoids in the regulation of thyroid function in man. J Clin Invest 49:1922-1929.

17. Gharib H, Hodgson SF, Gastineau CF, Scholz DA, Smith LA. 1972 Reversible hypothyroidism in Addison's disease. Lancet 2:734-736.

18. Re RN, Kourides LA, Ridgeway EC, Weintraub BD, Maloof F. 1976 The effect of glucocorticoid administration on human pituitary secretion of thyrotropin and prolactin. J Clin Endocrinol Metab 43:338-346.

19. Duick DS, Wahner HW. 1979 Thyroid axis in patients with Cushing's syndrome. Arch Intern Med 139:767-772.

20. Topliss DJ, White EL, Stockigt JR. 1980 Significance of thyrotropin excess in untreated primary adrenal insufficiency. J Clin Endocrinol Metab 50:52-56.

21. Visser TJ, Lambert SWJ. 1981 Regulation of TSH secretion and thyroid function in Cushing's disease. Acta Endocrinol 96:480-483.

22. Barnett AH, Donald RA, Espiner EA. 1982 High concentrations of thyroid-stimulating hormone in untreated glucocorticoid deficiency: indication of primary hypothyroidism? Br Med J 285:172-173.

23. Gonzalez JJ, Werk EE, Jr. 1985 Abnormal thyrotropin and prolactin levels in untreated corticotropin deficiency. Arch Intern Med 145:356-357.

24. Redei E, Hilderbrand H, Aird F. 1995 Corticotropin release-inhibiting factor is preprothyrotropin-releasing hormone-(178-199). Endocrinology 136:3557-3563.

25. Cizza G, Brady LS, Pacak K, Blackman MR, Gold PW, Chrousos GP. 1995 Stress-induced inhibition of the hypothalamic-pituitary-thyroid axis is attenuated in the aged Fischer 344/N male rat. Neuroendocrinology 62:506-513.

26. Hisano S, Fukui Y, Chikamori-Aoyama M, Aizawa T, Shibasaki T. 1993 Reciprocal synaptic relations between CRF-immunoreactive and TRH-immunoreactive neurons in the paraventricular nucleus of the hypothalamus. Brain Res 620:343-346.

27. Wilber JF, Utiger RD. 1969 The effect of glucocorticoids on thyrotropin secretion. J Clin Invest 48:2096-2103.

28. Brown MR, Hedge GA. 1974 Effects of glucocorticoids on TRH and TSH secretion: dose and time considerations. Am J Physiol 227:289-294.

29. Ahlquist JAO, Franklyn JA, Ramsden DB, Sheppard MC. 1989 The influence of dexamethasone on serum thyrotrophin and thyrotrophin synthesis in the rat. Mol Cell Endocrinol 64:55-61.

30. Brabant A, Brabant G, Schuermeyer T, Ranft U, Schmidt FW, Hesch RD, Muhlen AVZ. 1989 The role of glucocorticoids in the regulation of thyrotropin. Acta Endocrinol 121:95-100.

31. Kakucska I, Qi Y, Lechan RM. 1995 Changes in adrenal status affect hypothalamic thyrotropin-releasing hormone gene expression in parallel with corticotropin-releasing hormone. Endocrinology 136:2795-2802.

32. Larsen PR, Ingbar SH. 1992 The thyroid gland. In: Wilson JD, Foster DW (eds) Williams Textbook of Endocrinology. W.B. Saunders, Philadelphia, pp. 357-487.

33. Nicholson WE, Orth DN. 1996 Preprothyrotropin-releasing hormone-(178-199) does not inhibit corticotropin release. Endocrinology 137:2171-2174.

34. Rettori V, Jurcovicova J, McCann SM. 1987 Central action of interleukin-1 in altering the release of TSH, growth hormone, and prolactin in the male rat. J Neurosci Res 18:179-183.

35. Dubois J-M, Dayer J-M, Siegrist-Kaiser CA, Burger AG. 1988 Human recombinant interleukin-1ß decreases plasma thyroid hormone and thyroid stimulating hormone levels in rats. Endocrinology 123:2175-2181.

36. Pang X-P, Hershman JM, Mirell CJ, Pekary AE. 1989 Impairment of hypothalamic-pituitary-thyroid function in rats treated with human recombinant tumor necrosis factor-α (cachectin). Endocrinology 125:76-84.

37. Van der Poll T, Romijn JA, Wiersinga WM, Sauerwein HP. 1990 Tumor necrosis factor: a putative mediator of the sick euthyroid syndrome in man. J Clin Endocrinol Metab 71:1567-1572.

38. Hermus ARMM, Sweep CGJ, van der Meer MJM, Ross HA, Smals AGH, Benrad TJ, Kloppenborg PWC. 1992 Continuous infusion of interleukin-1β induces a nonthyroidal illness syndrome in the rat. Endocrinology 131:2139-2146.

39. Kakucska I, Romero LI, Clark BD, Rondeel JMM, Qi Y, Alex S, Emerson CH, Lechan RM. 1994 Suppression of thyrotropin-releasing hormone gene expression by interleukin-1-beta in the rat: implications for nonthyroidal illness. Neuroendocrinology 59:129-137.

DISTRIBUTION LIST

DEPARTMENT OF DEFENSE

ARMED FORCES RADIOBIOLOGY RESEARCH INSTITUTE
ATTN: PUBLICATIONS BRANCH
ATTN: LIBRARY

ARMY/AIR FORCE JOINT MEDICAL LIBRARY
ATTN: DASG-AAFJML

ASSISTANT TO THE SECRETARY OF DEFENSE
ATTN: AE
ATTN: HA(IA)

DEFENSE SPECIAL WEAPONS AGENCY
ATTN: TITL
ATTN: DDIR
ATTN: RAEM
ATTN: MID

DEFENSE TECHNICAL INFORMATION CENTER
ATTN: ACQUISITION
ATTN: ADMINISTRATOR

FIELD COMMAND DEFENSE SPECIAL WEAPONS AGENCY
ATTN: DASIAC
ATTN: FCIEO

INTERSERVICE NUCLEAR WEAPONS SCHOOL
ATTN: DIRECTOR

LAWRENCE LIVERMORE NATIONAL LABORATORY
ATTN: LIBRARY

UNDER SECRETARY OF DEFENSE (ACQUISITION)
ATTN: OUSD(A)/R&E

UNIFORMED SERVICES UNIVERSITY OF THE HEALTH SCIENCES
ATTN: LIBRARY

DEPARTMENT OF THE ARMY

HARRY DIAMOND LABORATORIES
ATTN: SLCSM-SE

OFFICE OF THE SURGEON GENERAL
ATTN: MEDDH-N

U.S. ARMY AEROMEDICAL RESEARCH LABORATORY
ATTN: SCIENCE SUPPORT CENTER

U.S. ARMY CHEMICAL RESEARCH, DEVELOPMENT, & ENGINEERING CENTER
ATTN: SMCCR-RST

U.S. ARMY INSTITUTE OF SURGICAL RESEARCH
ATTN: COMMANDER

U.S. ARMY MEDICAL DEPARTMENT CENTER AND SCHOOL
ATTN: MCCS-FCM

U.S. ARMY MEDICAL RESEARCH AND MATERIEL COMMAND
ATTN: COMMANDER

U.S. ARMY MEDICAL RESEARCH INSTITUTE OF CHEMICAL DEFENSE
ATTN: MCMR-UV-R

U.S. ARMY NUCLEAR AND CHEMICAL AGENCY
ATTN: MONA-NU

U.S. ARMY RESEARCH INSTITUTE OF ENVIRONMENTAL MEDICINE
ATTN: DIRECTOR OF RESEARCH

U.S. ARMY RESEARCH LABORATORY
ATTN: DIRECTOR

WALTER REED ARMY INSTITUTE OF RESEARCH
ATTN: DIVISION OF EXPERIMENTAL THERAPEUTICS

DEPARTMENT OF THE NAVY

BUREAU OF MEDICINE & SURGERY
ATTN: CHIEF

NAVAL AEROSPACE MEDICAL RESEARCH LABORATORY
ATTN: COMMANDING OFFICER

NAVAL MEDICAL RESEARCH AND DEVELOPMENT COMMAND
ATTN: CODE 42

NAVAL MEDICAL RESEARCH INSTITUTE
ATTN: LIBRARY

NAVAL RESEARCH LABORATORY
ATTN: LIBRARY

OFFICE OF NAVAL RESEARCH
ATTN: BIOLOGICAL & BIOMEDICAL S&T

DEPARTMENT OF THE AIR FORCE

BROOKS AIR FORCE BASE
ATTN: AL/OEBZ
ATTN: OEHL/RZ
ATTN: USAFSAM/RZB

OFFICE OF AEROSPACE STUDIES
ATTN: OAS/XRS

OFFICE OF THE SURGEON GENERAL
ATTN: HQ AFMOA/SGPT
ATTN: HQ USAF/SGES

U.S. AIR FORCE ACADEMY
ATTN: HQ USAFA/DFBL

U.S. AIR FORCE OFFICE OF SCIENTIFIC RESEARCH
ATTN: DIRECTOR OF CHEMISTRY & LIFE SCIENCES

OTHER FEDERAL GOVERNMENT

ARGONNE NATIONAL LABORATORY
ATTN: ACQUISITIONS

BROOKHAVEN NATIONAL LABORATORY
ATTN: RESEARCH LIBRARY, REPORTS SECTION

CENTER FOR DEVICES AND RADIOLOGICAL HEALTH
ATTN: DIRECTOR

GOVERNMENT PRINTING OFFICE
ATTN: DEPOSITORY ADMINISTRATION BRANCH
ATTN: CONSIGNED BRANCH

LIBRARY OF CONGRESS
ATTN: UNIT X

LOS ALAMOS NATIONAL LABORATORY
ATTN: REPORT LIBRARY

NATIONAL AERONAUTICS AND SPACE ADMINISTRATION
ATTN: RADLAB

NATIONAL AERONAUTICS AND SPACE ADMINISTRATION
GODDARD SPACE FLIGHT CENTER
ATTN: LIBRARY

NATIONAL CANCER INSTITUTE
ATTN: RADIATION RESEARCH PROGRAM

NATIONAL DEFENSE UNIVERSITY
ATTN: LIBRARY TECHNICAL SERVICES

NATIONAL INSTITUTE OF STANDARDS AND TECHNOLOGY
ATTN: IONIZING RADIATION DIVISION

U.S. DEPARTMENT OF ENERGY
ATTN: LIBRARY

U.S. FOOD AND DRUG ADMINISTRATION
ATTN: WINCHESTER ENGINEERING AND ANALYTICAL CENTER

U.S. NUCLEAR REGULATORY COMMISSION
ATTN: LIBRARY

RESEARCH AND OTHER ORGANIZATIONS

AUSTRALIAN DEFENCE FORCE
ATTN: SURGEON GENERAL

AUTRE, INC.
ATTN: PRESIDENT

BRITISH LIBRARY
ATTN: ACQUISITIONS UNIT

CENTRE DE RECHERCHES DU SERVICE DE SANTE DES ARMEES
ATTN: DIRECTOR

FEDERAL ARMED FORCES DEFENSE SCIENCE AGENCY FOR NBC PROTECTION
ATTN: LIBRARY

FOA NBC DEFENCE
ATTN: LIBRARY

INHALATION TOXICOLOGY RESEARCH INSTITUTE
ATTN: LIBRARY

INSTITUTE OF NUCLEAR MEDICINE AND ALLIED SCIENCES
ATTN: DIRECTOR

INSTITUTE OF RADIOBIOLOGY, ARMED FORCES MEDICAL ACADEMY
ATTN: DIRECTOR

OAK RIDGE ASSOCIATED UNIVERSITIES
ATTN: MEDICAL LIBRARY

RESEARCH CENTER OF SPACECRAFT RADIATION SAFETY
ATTN: DIRECTOR

RUTGERS UNIVERSITY
ATTN: LIBRARY OF SCIENCE AND MEDICINE

UNIVERSITY OF CALIFORNIA
ATTN: DIRECTOR, INSTITUTE OF TOXICOLOGY & ENVIRONMENTAL HEALTH
ATTN: LIBRARY, LAWRENCE BERKELEY LABORATORY

UNIVERSITY OF CINCINNATI
ATTN: UNIVERSITY HOSPITAL, RADIOISOTOPE LABORATORY

XAVIER UNIVERSITY OF LOUISIANA
ATTN: COLLEGE OF PHARMACY

REPORT DOCUMENTATION PAGE

Form Approved
OMB No. 0704-0188

1. AGENCY USE ONLY *(Leave blank)*	2. REPORT DATE	3. REPORT TYPE AND DATES COVERED
	February 1998	Reprints

4. TITLE AND SUBTITLE

AFRRI Reports, Third - Fourth Quarters 1997

5. FUNDING NUMBERS

NWED QAXM

6. AUTHOR(S)

7. PERFORMING ORGANIZATION NAME(S) AND ADDRESS(ES)

Armed Forces Radiobiology Research Institute
8901 Wisconsin Avenue
Bethesda, MD 20889-5603

8. PERFORMING ORGANIZATION REPORT NUMBER

SR97-11 - SR97-16

9. SPONSORING/MONITORING AGENCY NAME(S) AND ADDRESS(ES)

10. SPONSORING/MONITORING AGENCY REPORT NUMBER

11. SUPPLEMENTARY NOTES

12a. DISTRIBUTION/AVAILABILITY STATEMENT

Approved for public release; distribution unlimited.

12b. DISTRIBUTION CODE

13. ABSTRACT *(Maximum 200 words)*

This volume contains AFRRI Scientific Reports SR97-11 through SR97-16 for July-December 1997.

14. SUBJECT TERMS

15. NUMBER OF PAGES

72

16. PRICE CODE

17. SECURITY CLASSIFICATION OF REPORT	18. SECURITY CLASSIFICATION OF THIS PAGE	19. SECURITY CLASSIFICATION OF ABSTRACT	20. LIMITATION OF ABSTRACT
UNCLASSIFIED	UNCLASSIFIED	UNCLASSIFIED	UL